IDENTIFICATION OF FORCE COEFFICIENTS IN A SQUEEZE FILM DAMPER WITH A MECHANICAL SEAL

A Thesis

by

ADOLFO DELGADO-MARQUEZ

Submitted to the Office of Graduate Studies of
Texas A&M University
in partial fulfillment of the requirements for the degree of

MASTER OF SCIENCE

December 2005

Major Subject: Mechanical Engineering

IDENTIFICATION OF FORCE COEFFICIENTS IN A SQUEEZE FILM DAMPER WITH A MECHANICAL SEAL

A Thesis

by

ADOLFO DELGADO-MARQUEZ

Submitted to the Office of Graduate Studies of
Texas A&M University
in partial fulfillment of the requirements for the degree of

MASTER OF SCIENCE

Approved by:

Chair of Committee,	Luis San Andrés
Committee Members,	John M. Vance
	Othon K. Rediniotis
Head of Department,	Dennis L. O'Neal

December 2005

Major Subject: Mechanical Engineering

ABSTRACT

Identification of Force Coefficients in a Squeeze Film Damper
with a Mechanical Seal. (December 2005)
Adolfo Delgado-Marquez, B.S., Universidad Simón Bolívar
Chair of Advisory Committee: Dr. Luis San Andrés

Squeeze film dampers (SFDs) with low levels of external pressurization and poor end sealing are prone to air entrapment, thus reducing the damping capability. Furthermore, existing predictive models are too restrictive. Single frequency, unidirectional load and centered circular orbit experiments were conducted on a revamped SFD test rig. The damper journal is 1" in length and 5" in diameter, with nominal clearance of 5 mils (0.127 mm). The SFD feed end is flooded with oil, while the discharge end contains a recirculation groove and four orifice discharge ports to prevent air ingestion. The discharge end is fully sealed with a wave-spring that pushes a seal ring into contact with the SFD journal. The measurements conducted without and with lubricant in the squeeze film lands, along with a frequency domain identification procedure, render the mechanical seal dry-friction force and viscous damping force coefficients as functions of frequency and motion amplitude. The end seal arrangement is quite effective in eliminating side leakage and preventing air entrainment into the film lands. Importantly enough, the dry friction force, arising from the contact forces in relative motion, increases significantly the test element equivalent viscous damping coefficients. The identified system damping coefficients are thus frequency and amplitude of motion dependent, albeit decreasing rapidly as the motion parameters increase. Identified force coefficients, damping and added mass, for the squeeze film damper alone agree very well with predictions based on the full film, short length SFD model.

DEDICATION

To my mother, father, brother and close friends.

ACKNOWLEDGEMENTS

I thank my advisor and committee chair, Dr. Luis San Andrés, for his continued support and advice over the course of this research.

Thanks to all the graduate students at the Rotordynamics Laboratory, especially: Dario Rubio, Juan Carlos Rivadeneira, Arun Suryanarayanan and Zach Zutavern. The work of Anthony Breedlove and John Neff is gratefully acknowledged. I also thank Eddie Denk and the rest of the Turbomachinery Laboratory staff for all the technical support and assistance.

Finally, I thank Dr Luis San Andrés for giving me the opportunity to join the Tribology group and pursue research at Texas A&M Turbomachinery Laboratory.

NOMENCLATURE

c	Bearing radial clearance [m]
C_C	Cross coupled damping coefficient (CCO) [N.s/m]
C_D	Direct damping coefficient [N.s/m]
$C_{rv} = C_s$	Structure residual damping coefficient [N.s/m]
C_{seal}	equivalent viscous damping for mechanical seal [N.s/m]
C_{tt}	Squeeze film damper coefficient prediction (CCO) [N.s/m]
$C_{t\alpha}$	$C_{t\alpha}=C_{rv}+C_{seal}+C_{\alpha\alpha}$, System damping coefficients [N.s/m], $\alpha=x,y$
$C_{\alpha\beta}$	Identified squeeze film damping coefficients [N.s/m], $\alpha, \beta=x,y$
D_C	Cross coupled inertia coefficient (CCO) [kg]
D_D	Direct inertia coefficient [kg]
$D_{\alpha\beta}$	Identified squeeze film added mass coefficients [kg], $\alpha, \beta=x,y$
E	Energy dissipated [J]
$F_{x,y}$	External (shaker) forces applied to bearing [N]
$\bar{F}_{x,y}$	Frequency components of external forces applied to bearing [N]
F_μ	Dry friction force from contact in mechanical seal [N]
f_n	Natural frequency [Hz]
$H_{\alpha\alpha}$	Dynamic impedance, $\alpha=x,y$
$K_{sx,,} K_{sy}$	Structural (support) stiffnesses [N/m]
L, D	Length and diameter of SFD land [m]
M	Mass of bearing housing [kg]
M_f	Estimated mass of lubricant (feed plenum & recirculation annulus) [kg]
M_T	$M+M_f+D$. Dynamic mass of lubricated test system [kg]
P_s , P_r	Inlet pressure and pressure at recirculation annulus [Pa]
Q	Volumetric flow [LPM]
T	Lubricant temperature [°C]
U_α	Experimental Uncertainty (α= measured variable)

V	Velocity vector [m/s]
x,y	Bearing dynamic motions along X,Y directions [m]
$\overline{x}, \overline{y}$	Frequency components of bearing motions [m]
$z_{(\omega)}$	Complex displacement in frequency domain [m]
ΔP	P_s-P_r, Pressure differential across SFD [Pa]
ρ, μ	Lubricant density [kg/m^3] and viscosity [Pa.s]
ω, ω_n	Excitation frequency [rad/s], natural frequency [rad/s]
ζ	$C/[2\ (K_s M)^{1/2}\ ]$. Viscous damping ratio

TABLE OF CONTENTS

Page

LIST OF TABLES

LIST OF FIGURES

Page

Page

Page

Page

Page

I INTRODUCTION

Squeeze Film Dampers (SFDs) are widely used to provide external damping in aircraft gas turbines supported on rolling element bearings, as well as in hydrocarbon compressors, for example. SFDs also aid to attenuate rotor synchronous responses at passage through critical speeds where shaft vibration amplitude due to imbalance peaks. A typical SFD consists of a stationary journal (generally the outer race of a ball bearing) and a cylindrical housing, both separated by a small gap filled with lubricant. In operation, the dynamic motion of the journal (whirling) squeezes the thin lubricant film, thus generating hydrodynamic pressures and film forces able to dissipate mechanical energy [1].

The forced performance (damping capability) of a SFD depends on its geometrical configuration as well as on the operational parameters such as flow regime, type of journal motion, lubricant viscosity, cavitation type and air entrapment among others [2]. In particular, the latter can lead to a severe reduction of the damping force coefficients [3,4]. Air entrapment occurs at sufficiently high whirl frequencies and large vibration amplitudes where air is ingested into the lubricant film, becoming entrapped, thus severely reducing the damper forced performance [5]. The severity of air ingestion and entrapment increases with frequency and journal amplitudes. This phenomenon is more pervasive in open ends SFD configurations, where at least one of the damper ends is exposed to ambient.

Presently, with increasing rotor flexibilities and shaft speeds, high performance turbomachinery undergoes high dynamic loads and large displacements. Under these conditions, air ingestion and entrapment compromise the performance of SFDs with opened end or partially sealed configurations. Sealed SFDs prove to be less prone to air ingestion/entrapment at high frequencies, thus enhancing their performance at such frequencies. Dif[l]ferent types of seals have been adopted (O-rings, end plates, etc.), yet there are many more seal and geometric configurations (i.e. oil feeding arrangement,

---

This thesis follows the style of *ASME Journal of Tribology*.

grooves) used in practice and not yet thoroughly researched. This work includes the experimental study of a particular sealed SFD configuration. The configuration comprises of a mechanical contact end seal and a recirculation annulus at one end of the test damper element.

II LITERATURE REVIEW

Squeeze Film Dampers have been a subject of study since about 45 years ago, when they were introduced as an effective mean for attenuating vibration in turbomachinery. Della Pietra and Adilleta [6,7] present a compilation of the research conducted on SFDs in the last 40 years. The authors include a complete description of SFDs, their physical characteristics, including end seal configurations, the research efforts carried out for modeling SFD forced performance, developing predictive models and validations with test data, etc.

The present review discusses previous works related to experimental parameter identification of force coefficients and those studying the influence of end seals and feeding grooves on the performance of SFDs.

San Andrés and Vance [8] present a detailed experimental work conducted on a controlled orbit SFD test rig. The test rig comprises a journal mounted on an eccentric lobe of a stiff shaft running on ball bearings with solid steel supports. Measurements of dynamic pressure distribution in the oil film are conducted for increasing frequencies. The results show large levels of dynamic pressures at the damper central groove, thus indicating the importance of groove pressures on the overall damper force performance.

Roberts *et al*. [9] present an experimental and theoretical work focused on the parameter identification of damping and inertia force coefficients from transient response data (impact tests). The theoretical analysis includes predictions based on the long and short length bearing models. A parameter identification of the decay response data yields the empirical coefficients which are compared to analytical ones. The test direct damping coefficients for a squeeze film damper with open ends show good agreement with predictions based on the short length bearing model. On the other hand, inertia and cross-coupled damping coefficients are well under predicted. Additionally, the results show that “memory effects” (frequency dependency) within the squeeze film are not significant.

Ellis *et al*. [10] present a parameter identification procedure based on the State Variable Filter (SVC) method. The method relies on the assumption that a linearized two-dimensional model is appropriate for determining the set of dynamic force coefficients in a squeeze-film bearing. The evaluation of the method comprises parameter identification from simulated data and experimental data. Simulated input data includes increasing noise levels to asses the sensitivity of the method to signal noise as it would be present in actual experimentation. Noise proves to affect the accuracy of the method, particularly in a heavily damped system. Results show that the linear model may not be appropriate for high magnitudes of static eccentricity (ratio >0.5).

Miller *et al*. [11] present the identification of rotordynamic coefficients of a squeeze film damper. The experimental procedure consists of various set of impact tests delivered with an impact gun. The tests are conducted under different temperature conditions and journal off-center positions. The parameter identification method transforms the test element time response to the frequency domain and extracts dynamic force coefficients from the bearing impedance matrix as a function of frequency. The estimated damping coefficients agree well with theoretical predictions (based on the analysis of San Andrés and Vance [8]). Furthermore, the identified coefficients do not show any significant variation with the magnitude of impacts exerted on the test element.

Levesley and Holmes [12] compare the damping capacity and general performance of various SFD configurations, including different types of end seals. Their results show that an end-sealed SFD provides more damping capacity and is less prone to the occurrence of oil vapor cavitation. The authors conclude that piston-ring end sealed SFDs have a better performance over two other end seal arrangements tested (end-chambered and end plate seals).

Arauz and San Andrés [13] present a series of experiments to determine the effects of a circumferential feeding groove on the dynamic response of a squeeze film damper. The damper is sealed by a serrated piston ring located at the discharge end of the damper. The tests comprise different damper configurations including two different groove depths and journal orbit radii. The experiments show similar magnitudes for the

dynamic pressures measured at the groove and those at the film lands for all the configuration tested. Consequently, as indicated by Vance and San Andrés [8], relatively large damping forces are generated at the groove, which contribute significantly to the damping characteristics of the SFD.

Diaz and San Andrés [3] use the instrumentation variable filter (IVF) method for parameter identification of a n-DOF mechanical linear system, and a particularized form of the method for the parameter identification of a squeeze film damper operating with a bubbly mixture (air in oil). The method, based on frequency domain analysis, proves to be a reliable tool for the identification of bearing force coefficients. The predictions of the system dynamic flexibilities fairly agree with the experimental results within the frequency range from 10 Hz to 50 Hz (system natural frequency of 30 Hz), and for various test conditions including different air entrapment volume percentages in the lubricant mixture. The conclusions confirm that the amount of damping provided by the test SFD is greatly affected by the amount of air ingestion.

De Santiago and San Andrés [14] identify the damping coefficients of a sealed ends, integral SFD from rotor imbalance response tests and impact tests. Both ends of the SFD are sealed by end plates of known clearance. Model predictions of the damping coefficients are in good agreement with the identified coefficients. The experiments results show that the amplitudes of rotor synchronous response at the first and second critical speeds are proportional to the imbalance displacement, thus evidencing the linearity of the SFD elements. Furthermore, the identified damping coefficients of the integral sealed damper are twice as large as values obtained in [1] for the same damper with no end seals.

Diaz and San Andrés [15] present two methods for identification of damping coefficients in a squeeze film damper. The first method consists on a least-square curve fitting of the damping forces in the time domain, and the second one is based on approximating the rotor orbit using its synchronous components (Filtered Orbit Method). The frequency domain method proves to be more adequate and simpler than the time domain method. The results from the experiments show that the identified damping

coefficients are insensitive to whirl frequency and nearly independent of the imbalance magnitude.

San Andrés and De Santiago [16] present experiments to obtain the dynamic parameters of an open-end SFD, and comparisons to predictions based on the full-film, short length bearing theory. The publication addresses the effects of fluid inertia as well as the effects of air entrapment on the dynamic response of the SFD. The authors show an interesting approach to predict the performance of the SFD operating with severe air entrapment. The air entrapment is accounted for as a reduction of the effective length of the damper rather than a reduction in the effective viscosity of the air in oil film mixture (as presented in previous analytical efforts). The effective length of the SFD is frequency and amplitude dependant, as the amount of air entrapped is a function of these two variables. In the experiments presented, the damper effective length ranged from 82% to 78% of the actual damper length. The identified damping force coefficients agree well with predictions, except for the identified inertia coefficients that are approximately twice as large as those obtained from conventional model predictions.

Kim and Lee [17] present an analytical and experimental study of a sealed squeeze film damper with a central feeding groove. A dynamic pressure field analysis allows identifying the SFD dynamic force coefficients. The analysis includes the effect of the groove and end seal over the dynamic coefficients of the SFD. The model relies on the short length bearing model (centered condition). Two types of seals are modeled, a single-stage and two-stage liquid seals. Experiments are conducted on a test rig that incorporates two magnetic bearings and the SFD at one end. The magnetic bearings excite the system with single frequency loads. The first frequency components of the force and displacements are extracted in the time domain to reduce spectral leakage. Damping and inertia coefficients are identified for different seal clearances and compared to analytical results. The results show that the model accounting for the two-stage seal presents good agreement with the inertia coefficients but underestimates the damping coefficients.

This review shows that SFDs have been extensively tested and analyzed. However, there are many more practical configurations and variations to be conceived or/and tested. In particular, the adequate location of grooves, feed and discharge recirculation annuli, and the type of end sealing are some of the geometric features that have not being fully exploited. Furthermore, none of the papers reviewed presents good agreement between the experimental and analytical results for both, damping and added mass coefficient simultaneously. Thus, more analytical and experimental works are needed to fully understand and maximize the performance of SFDs.

This experimental work stands to evaluate the performance of an end sealed SFD configuration that has not been tested before. The SFD design features an end mechanical seal that allows regulating the oil flow through the squeeze film. The damper can operate as an open end, partially sealed or fully sealed end configuration. This SFD design is currently being used in industry, yet no experimental work has been conducted to test the effectiveness or advantages of this SFD design over other dampers.

Figure 1 depicts the actual sealed end configuration use in industry. This damper combines a discharge recirculation annulus and adjustable flow (upon assembly) mechanical seal at one end. This arrangement is intended to reduce the occurrence of air entrapment and to allow the SFD to operate as an open end, partially sealed or fully seal configuration. A test damper that replicates this end seal SFD was designed and adapted to an existing test rig. A description of the test rig and damper follows.

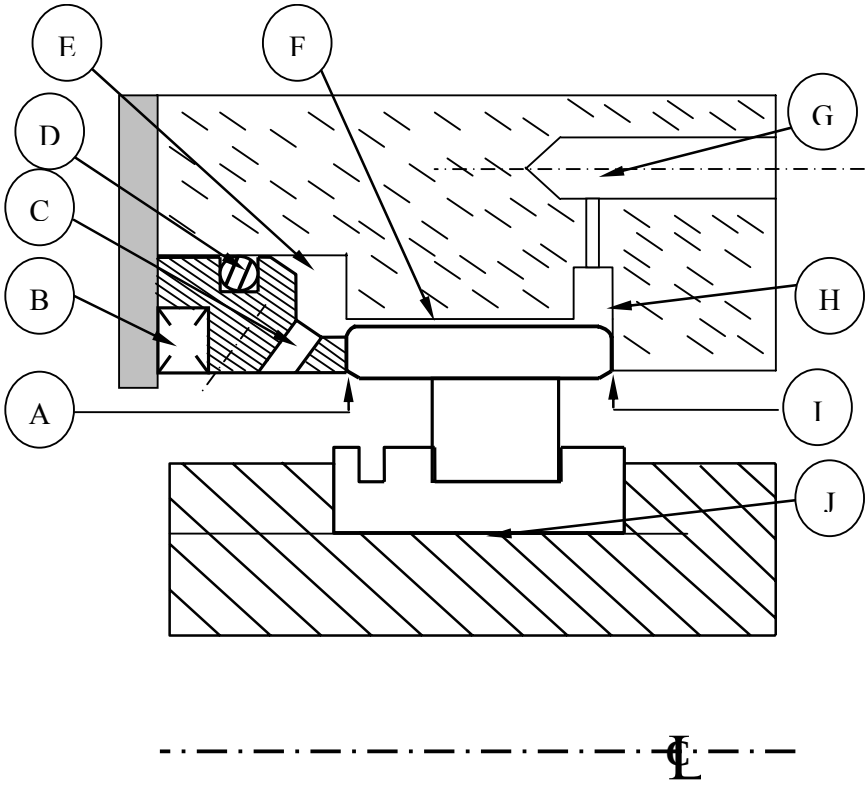

A: Bearing Outer ring and O-ring carrier contact interface	F: SFD land
B: Wave Spring	G: Oil inlet
C: Oil discharge orifice	H: Recirculation annulus (supply side)
D: O-ring	I: Outer ring and bearing support contact interface
E: Recirculation annulus (discharge side)	J: Bearing bore (or inner ring)

Figure 1 Schematic view of an industrial end sealed SFD. (Courtesy of Honeywell®)

III TEST RIG DESCRIPTION

The test rig comprises of the same structure reported in a previous TRC research project [18]. Figure 2 shows a schematic view of the test rig structure. A vertical rigid shaft mounted on three precision ball bearings (natural frequency 400 Hz [16]), holds a steel journal of 5" (127 mm) diameter and 3" (76.2 mm) long. The bearing assembly consists of an acrylic bearing sandwiched by two steel plates, attached by two vertical steel plates. These plates also serve as an interface to apply external forces onto the bearing assembly. The top plate includes a connection for lubricant supply through a flexible hose, a static pressure gauge displaying the feed pressure into the bearing and four eddy current sensors facing the shaft. The composite bearing housing hangs from a top structure with four steel rods giving a structural stiffness to the test bearing section.

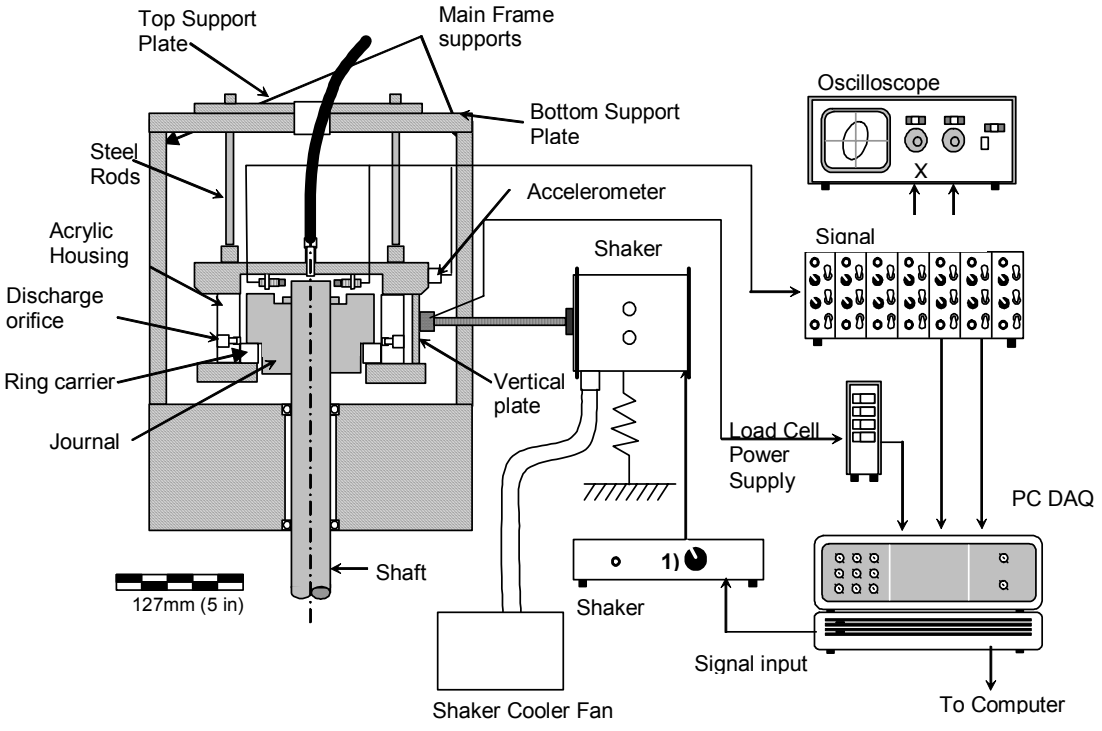

Figure 2 Test rig for dynamic force measurements and flow visualization in a sealed end SFD.

A mechanism comprising two sliding flat plates (top and bottom support plates) on the top structure allows centering and off-centering positioning of the bearing with respect to the shaft [18].

Figure 3 shows the sensor disposition and reference coordinate system on the SFD housing. Two electromagnetic shakers (max. 100 lbf or 448 N), suspended from separate steel frames, stand to provide excitation forces onto the test device. Slender steel stingers connect the shaker to the bearing housing (*x* and *y* directions). Piezoelectric load cells are fastened to the side plates and the one of the stingers end. The top disk allocates two accelerometers *(x,y)*, right above the side plates.

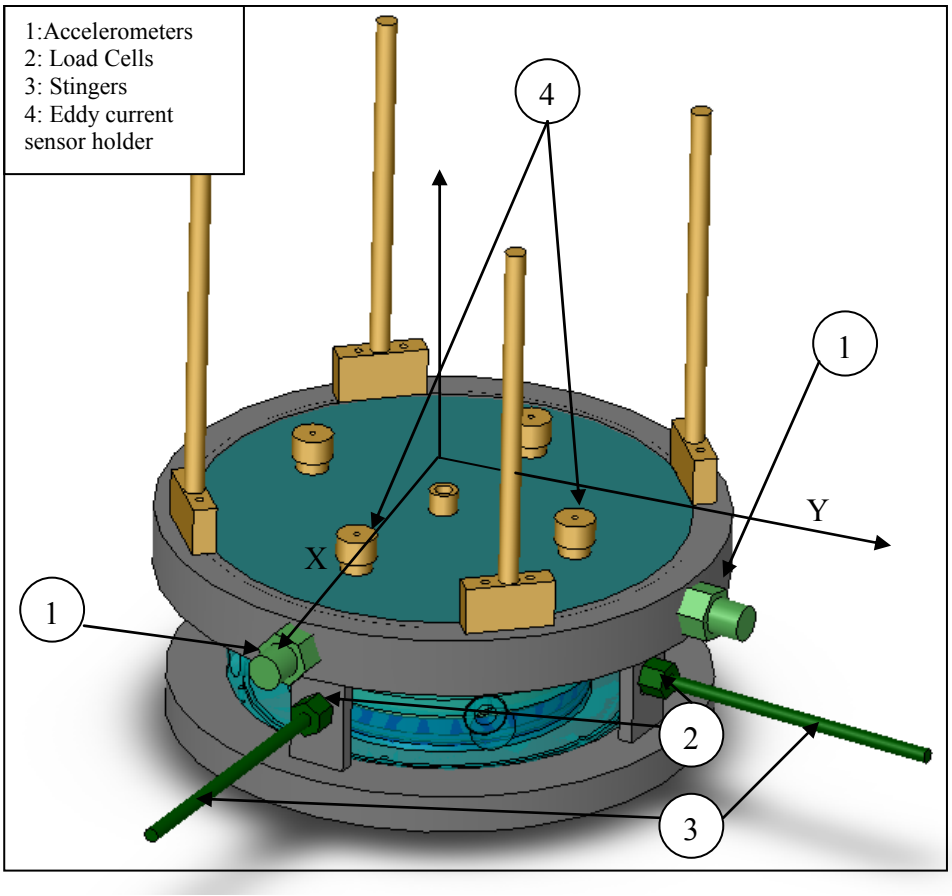

Figure 3 SFD housing reference coordinate system and location of sensors.

The bearing housing design integrates a SFD land and an annulus that accommodates a metallic ring (ring holder). This metallic ring along with the journal bottom surface provides a metal-metal mechanical seal. A wave spring, pushing the ring holder against the journal, applies a contact force between the matting surfaces. Furthermore, different sets of shims make it possible to adjust the contact force between the surfaces. Figure 4 and Figure 5 depict a cross section and a cut view of the end sealed SFD design along with its components, respectively.

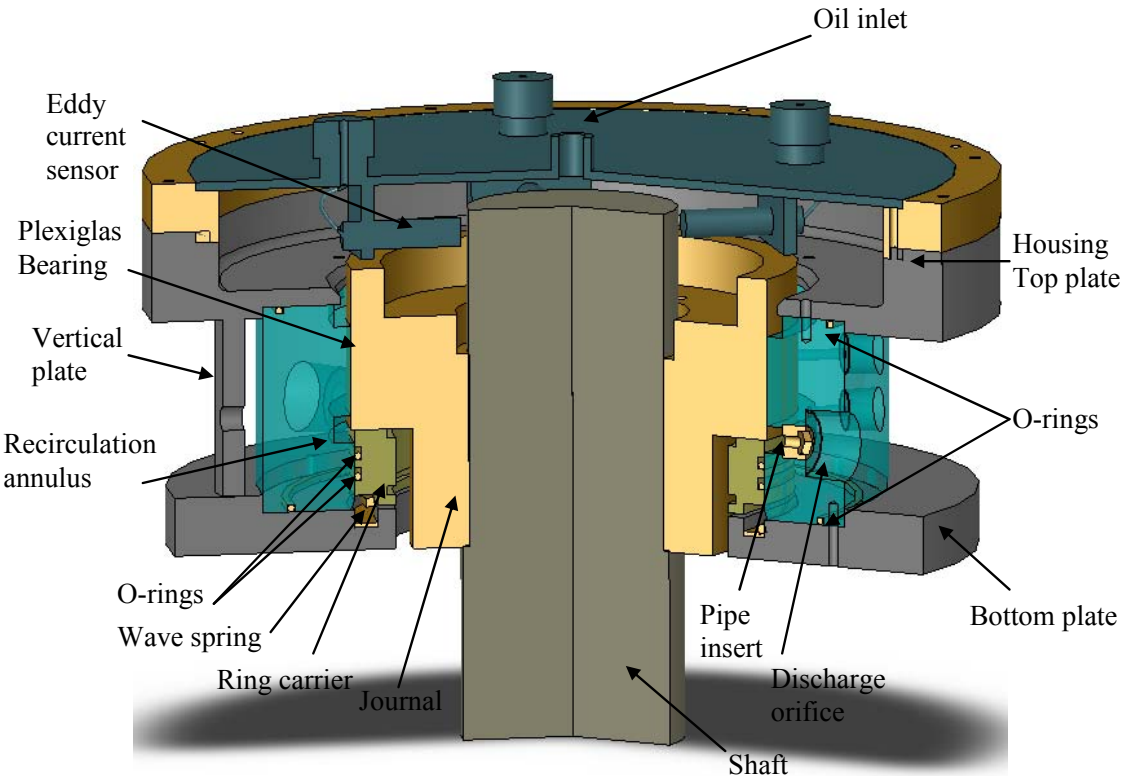

Figure 4 Sealed-end SFD assembly cross section view.

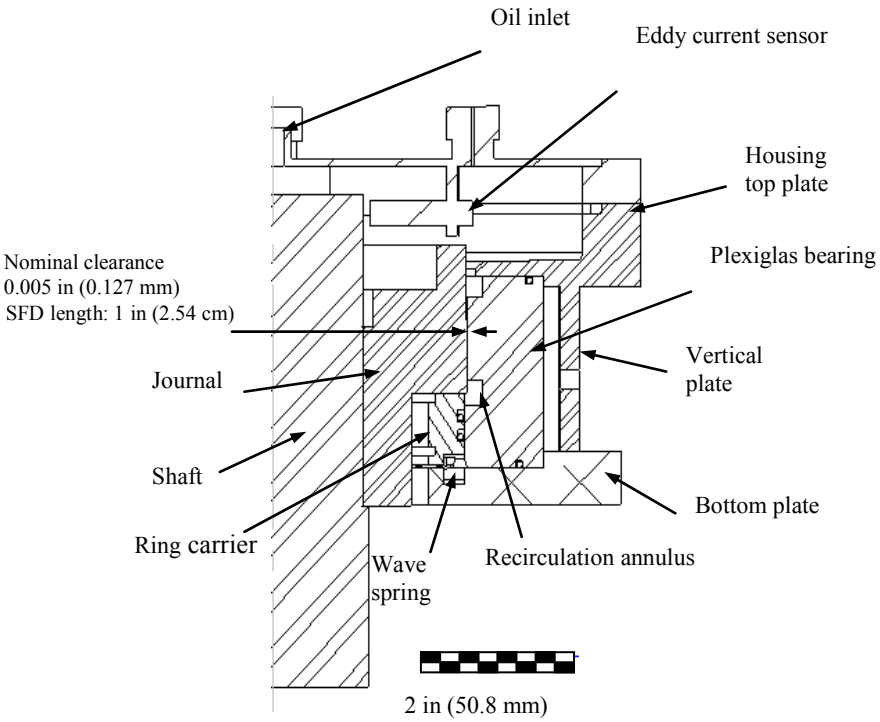

Figure 5 Cut view of sealed-end SFD assembly.

III.1 Data acquisition and post-processing

A DAQ board serves as interface to connect the instrumentation, including pressure sensors, accelerometers, load cells and proximity probes to a PC. The data is recorded using a modified version of an existing Labview® virtual instrument (VI) initially designed by Diaz [19]. The modified version includes the following features to the LabView DAQ VI

- Control magnitude and frequency of 2 shakers (real time- no need to stop operation)
- Control oil pump frequency controller through and digital output (using a relay box).
- Control system to automatically adjust shaker input level to match a given load or displacement magnitude (selected by operator).
- Automated operation for multi-frequency tests.

A Mathcad® worksheet processes the recorded time traces (displacements, acceleration, forces), transforms the data into the frequency domain, and performs the spectral analysis to identify the test SFD force coefficients.

III.2 Lubrication system

Figure 6 depicts the lubrication system of the test rig, presently including two flowmeters and pipe lines for the four outlets of the new SFD configuration (end sealed). The flowmeters, located at the SFD inlet and outlet lubrication lines, allow estimation of leakage flow through the SFD end seal.

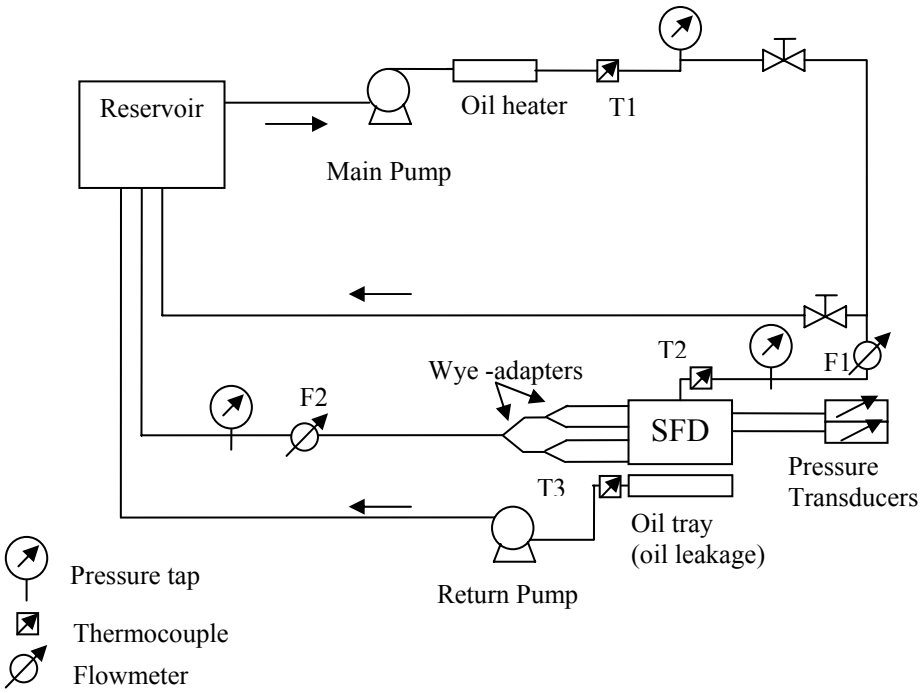

Figure 6 Schematic view of lubricant system.

The piping for connecting the SFD multiple oil outlets is symmetric in order to equalize the friction losses for each of the four outlets. This implies same longitude hoses and symmetric wye adapters.

The lubricant used is an ISO VG 2 with a density (ρ) of 736 kg/m^3 and its absolute viscosity is related to temperature, T (°C) by

$$\mu_{oil}(T) = 2.8e^{-0.01665(T-23.6)} \text{ cPoise} \quad (1)$$

obtained from viscosity measurements using a rheological viscometer [18].

IV IDENTIFICATION OF STRUCTURAL PARAMETERS (DRY SYSTEM)

IV.1 Static tests

The SFD assembly was separated into its components: Plexiglas bearing, top and bottom plates, and top lid. Each component is weighted using a calibrated scale (±0.01 lb). The weight of the rods and blocks (connecting the rods to the SFD assembly) is measured using a smaller scale (±0.001 lb). Table 1 shows the weight of each of the mentioned components and the estimated effective mass. Notice that for a steel rod, its effective mass is approximately 1/4 of its total mass, since each rod is fixed as a cantilever beam.

Table 1 Measured weight and estimated effective mass of the SFD assembly and connecting rods.

	Weight [lb]
SFD Assembly [±0.01] *	14.13 (6.4 kg)
Lid and hose connector**	6.60(3 kg)
Rods [±0.001]	1.3 (0.59 kg)
Blocks[±0.001]	0.25 (0.11 kg)
Total effective mass	21.3 (9.7 kg) (±1%)

*: including hose connectors, ring carrier and sensors.
**: including pressure sensor.

Static load tests using a force gauge (±0.5 lb) and two eddy current sensors[2] (*X2,Y2*) yield two stiffness parameters (K_{sx}, K_{sy}). These tests were conducted without the journal in position (i.e. no rubbing interface). Figure 7 shows the bearing deflections in the *X* and *Y* directions due to a force exerted in the same direction. Each data point represents an average of a set of two static load tests. The results follow a linear tendency along the entire range of loads exerted on the SFD assembly (-89 N to 89 N). Thus, a constant stiffness coefficient in each direction (*X* and *Y*) is appropriate to characterize the rigidity of the four rods arrangement.

[2] Appendix A details calibration of eddy current sensors.

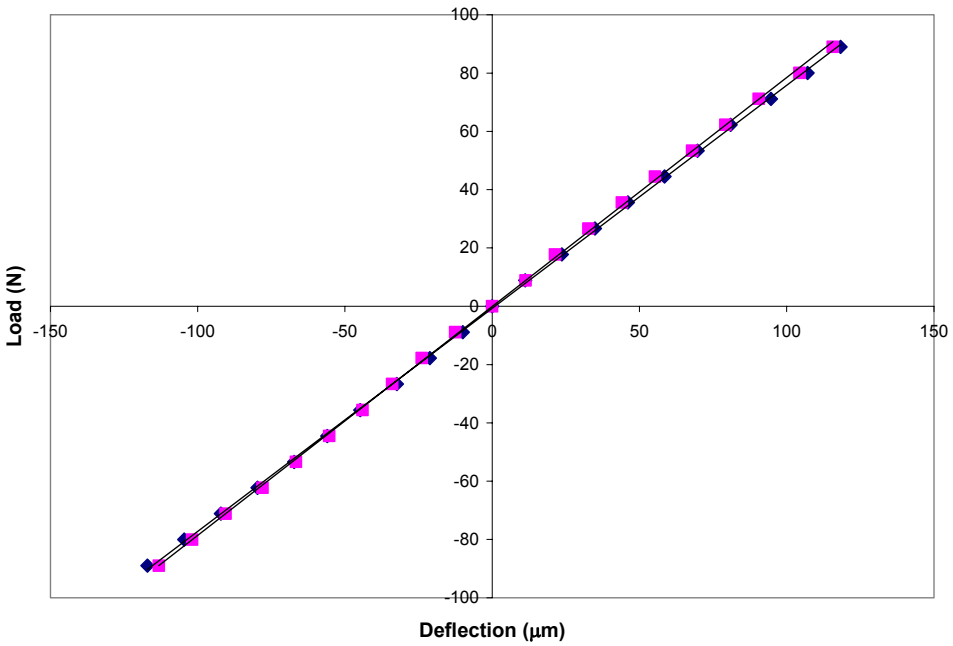

Figure 7 Bearing deflection vs. applied load in the *X,Y* direction due to a force applied in the respective (same) direction. (U_F: 0.5 lb)

Table 2 presents the structure stiffnesses in the *X* and *Y* directions. The values are very close to each other (~4% different), confirming the isotropy of the elastic support system.

Table 2 Structural stiffness coefficients of bearing support from static tests

	K_{sx}[lb/in]	K_{sy}[lb/in]
Value	4370 (765 x10^3 N/m)	4490 (786 x10^3 N/m)
Uncertainty	175 [~4%]	180 [~4%]
Range[lb]	-20 to 20	-20 to 20
f_n* [Hz]	45±1	45±1

*: obtained using the stiffnesses and mass measured from static tests

IV.2 Impact tests

A sets of impact tests performed along the *X* and *Y* directions of the SFD assembly stand to identify the structural parameters of the SFD assembly. Figure 8 depicts the time trace of a typical impact and displacement registered in the *Y* and *X* directions, respectively.

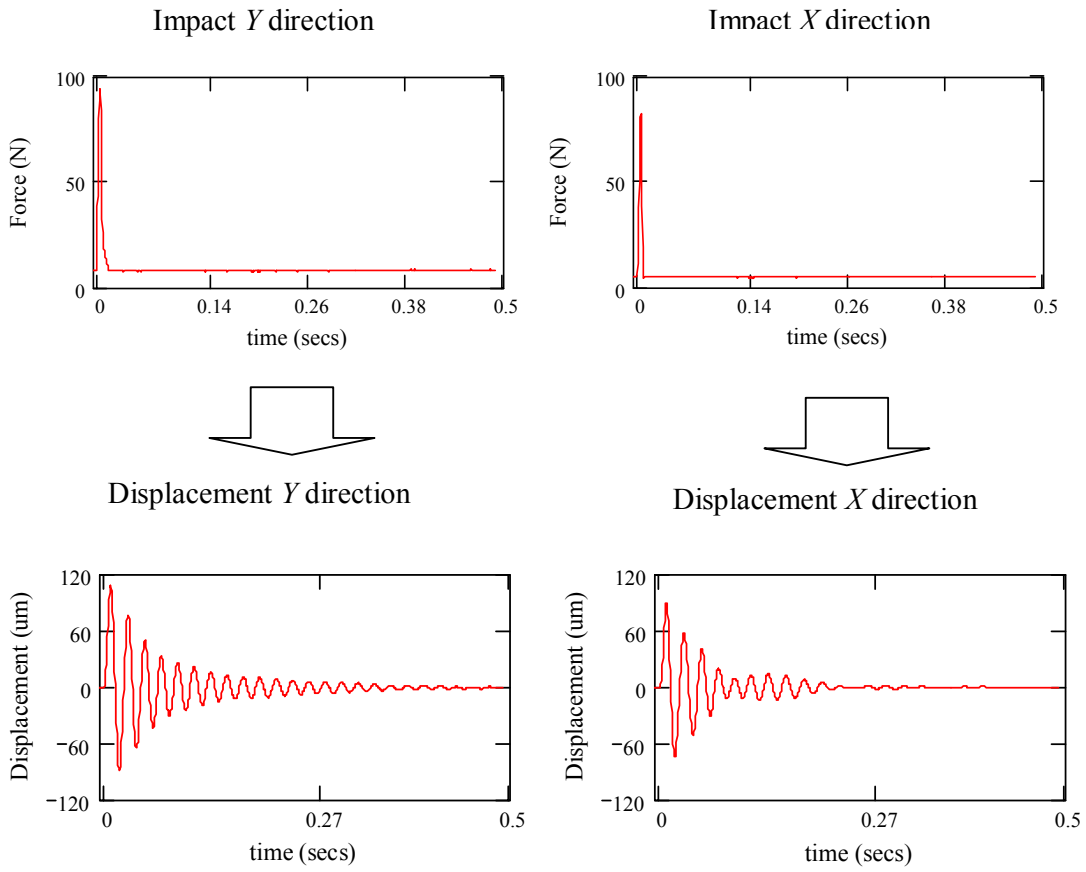

Figure 8 Impact and displacement time traces in the *Y* and *X* directions. (impact load tests)

Figure 9 and Figure 10 show the system transfer functions in the *X* and *Y* directions, respectively obtained from each impact test. Table 3 presents the identified parameter derived from the impact tests exerted on the bearing assembly. Appendix B presents the uncertainty analysis of the identified coefficients. In Figure 9 the two resonant peaks correspond to the natural frequency of the main frame (shown in Figure 1) (~47 Hz) and the SFD assembly (~49 Hz).

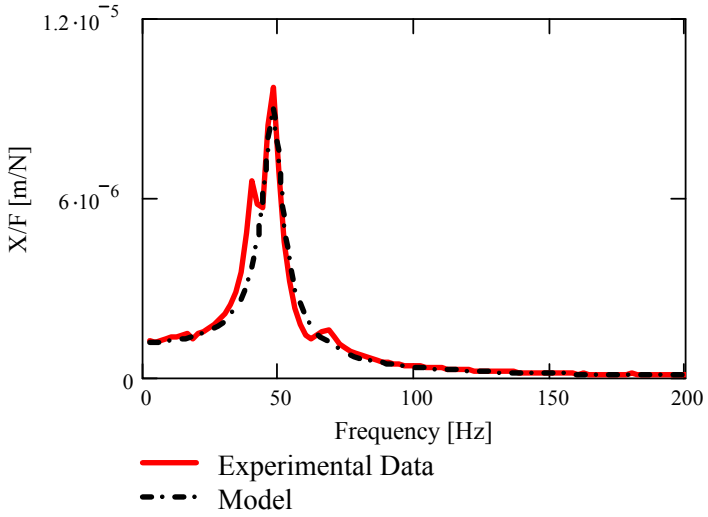

Figure 9 Impact tests transfer function and analytical fit for motions along *X* direction. (Dry system, end seal not in place)

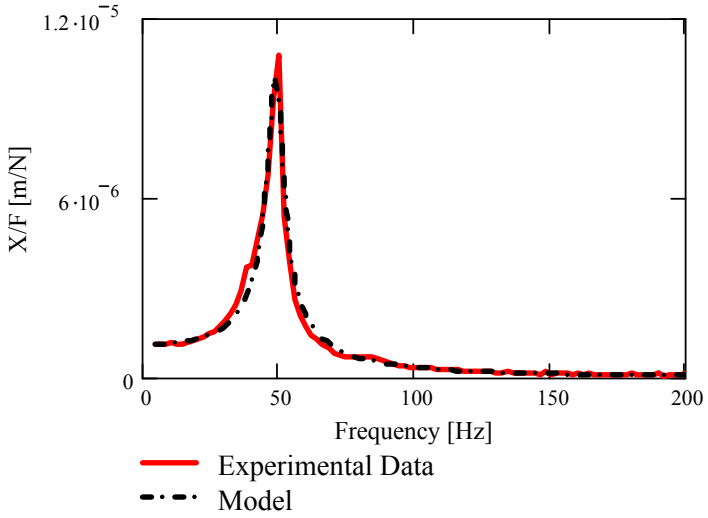

Figure 10 Impact tests transfer function and analytical fit for motions along *Y* direction. (Dry system, end seal not in place)

Table 3 Identified parameters from impact tests exerted on SFD test section (no lubricant)

	Parameters	*X*	*Y*
SI	Stiffness, K_s [kN/m]	800 (±40)	923 (±46)
	Mass, M [kg]	8.8 (±0.5)	9.7 (±0.5)
	Damping, C_s [N.s/m]	367	315
US	Stiffness, K_s [lb/in]	4570 (±230)	5270 (±265)
	Mass, M [lb]	19.5 (±1)	21.5 (±1.1)
	Damping, C_s [lb.s/in]	2.1	1.8
	Damping ratio, ζ	0.069	0.052
	Natural Frequency f_n[Hz]	47 ±1	49 ±1
	R^2 (goodness of fit)	0.96	0.98

The mass estimated from the static tests (measured weight and static stiffness) is in agreement (within uncertainty) with the values obtained from impact tests in the *X* direction (~1%) and *Y* direction (~0.5%). The stiffness estimated from impact tests are similar (within ~4%) to the one obtained from static test in the *X* direction, whereas in the *Y* direction both approaches (impact load and static load tests) render different magnitudes (~15%). This discrepancy is attributed to the alignment of the impact hammer respect to the test device. The test rig has limited accessibility in the *Y* direction for correct positioning the impact hammer.

In the following, the stiffness of the test system is taken from the static load tests (uncertainty band 4%), i.e. K_{sx} = 788 kN/m, and K_{sy} =823 kN/m.

IV.3 Periodic input load tests

This section focuses on the identification of the damping characteristics of the dry system (no lubricant) with the mechanical seal in place. The aim is to asses the effect of the mechanical seal on the system damping (i.e. dry friction). Four set of single frequency excitation tests serve to characterize the damping characteristics of the system. The tests include two load magnitudes (40-39 N and 35-33 N) from 20 Hz up to 200 Hz. The excitation loads exerted along both directions have the same magnitude and are 90^0

out of phase (i.e. circular load orbit). The results in Figures 10-17 correspond to the last set of tests. Appendix C shows system responses and excitation orbits for selected frequencies.

Figures 11 through 13 show the waterfalls of the load, displacements and acceleration magnitudes in along the X and Y directions, respectively. Figure 11 evidences fluctuations of the load magnitude at high frequencies (from 150 Hz to 200 Hz). These fluctuations are introduced by the FFT operator (frequency resolution) and do not reflect the actual load magnitude shown in Figure 14. Figure 13 shows super synchronous components in the acceleration mainly for load excitations with frequency close to 50 Hz. Odd super synchronous frequencies evidence dry friction interaction.

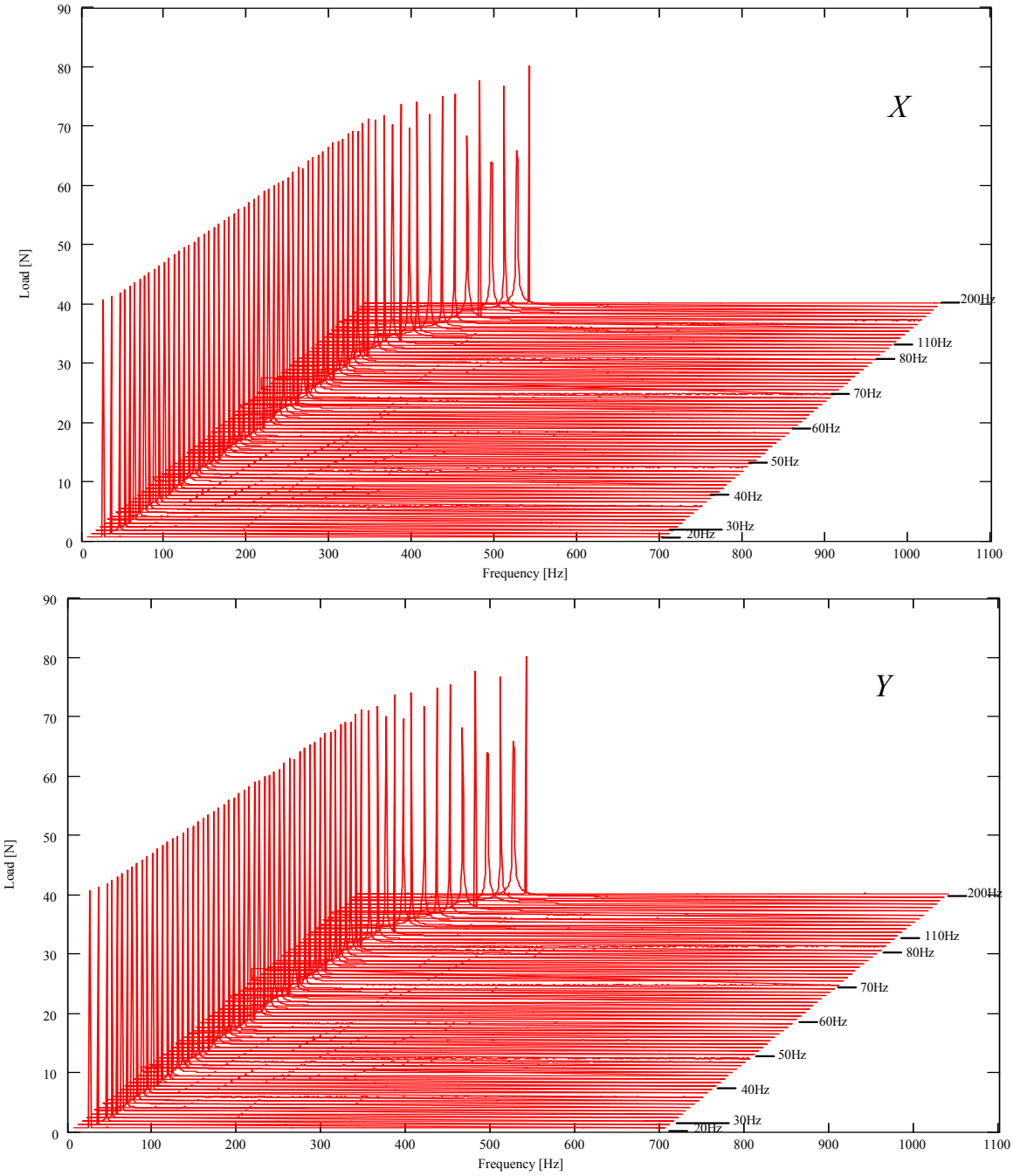

Figure 11 Waterfalls of excitation load in the *X* and *Y* directions. (Dry SFD. end seal in place. L: 40 N)

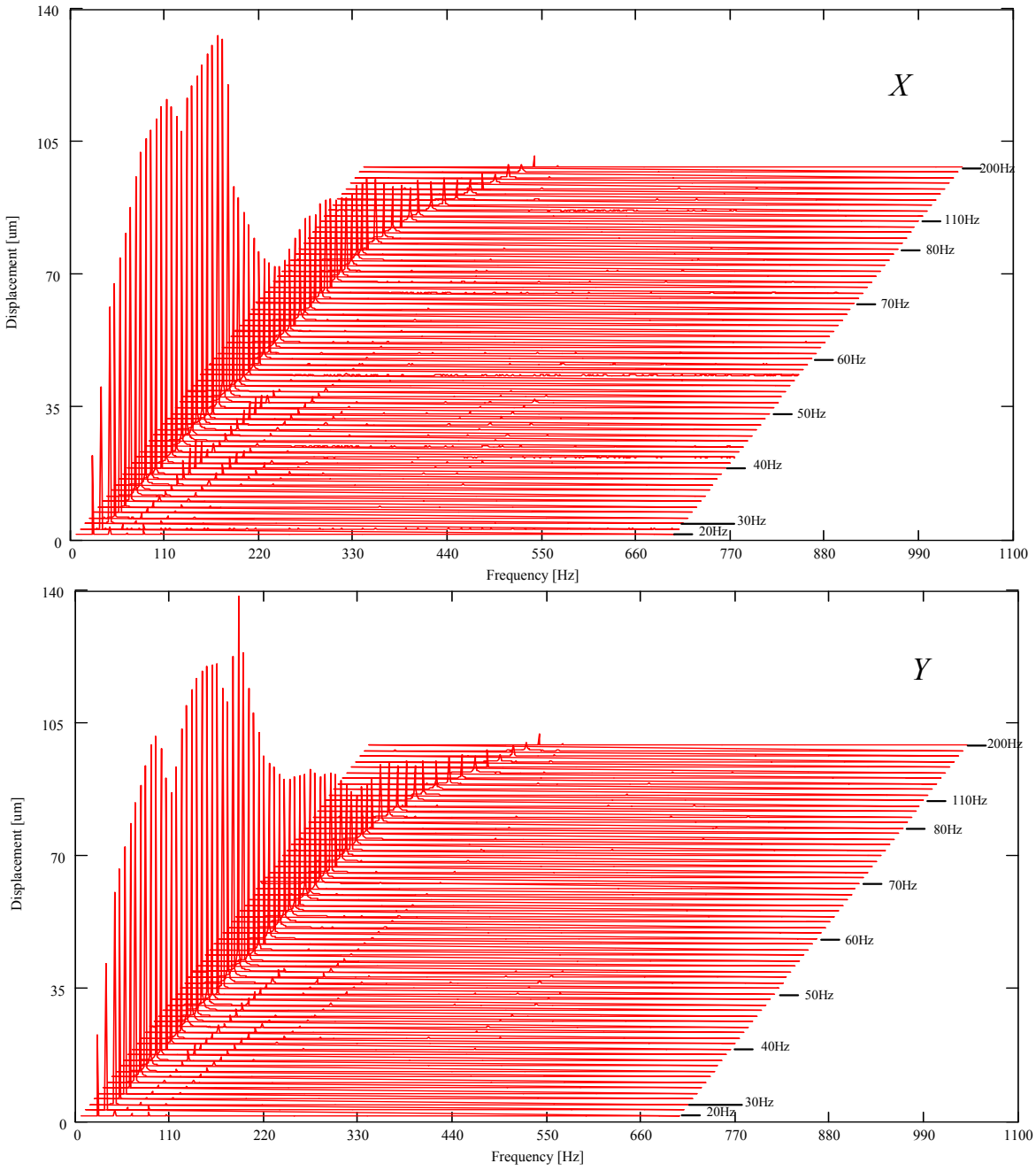

Figure 12 Waterfalls of displacement response in the *X* and *Y* directions. (Dry SFD. end seal in place. L: 40 N)

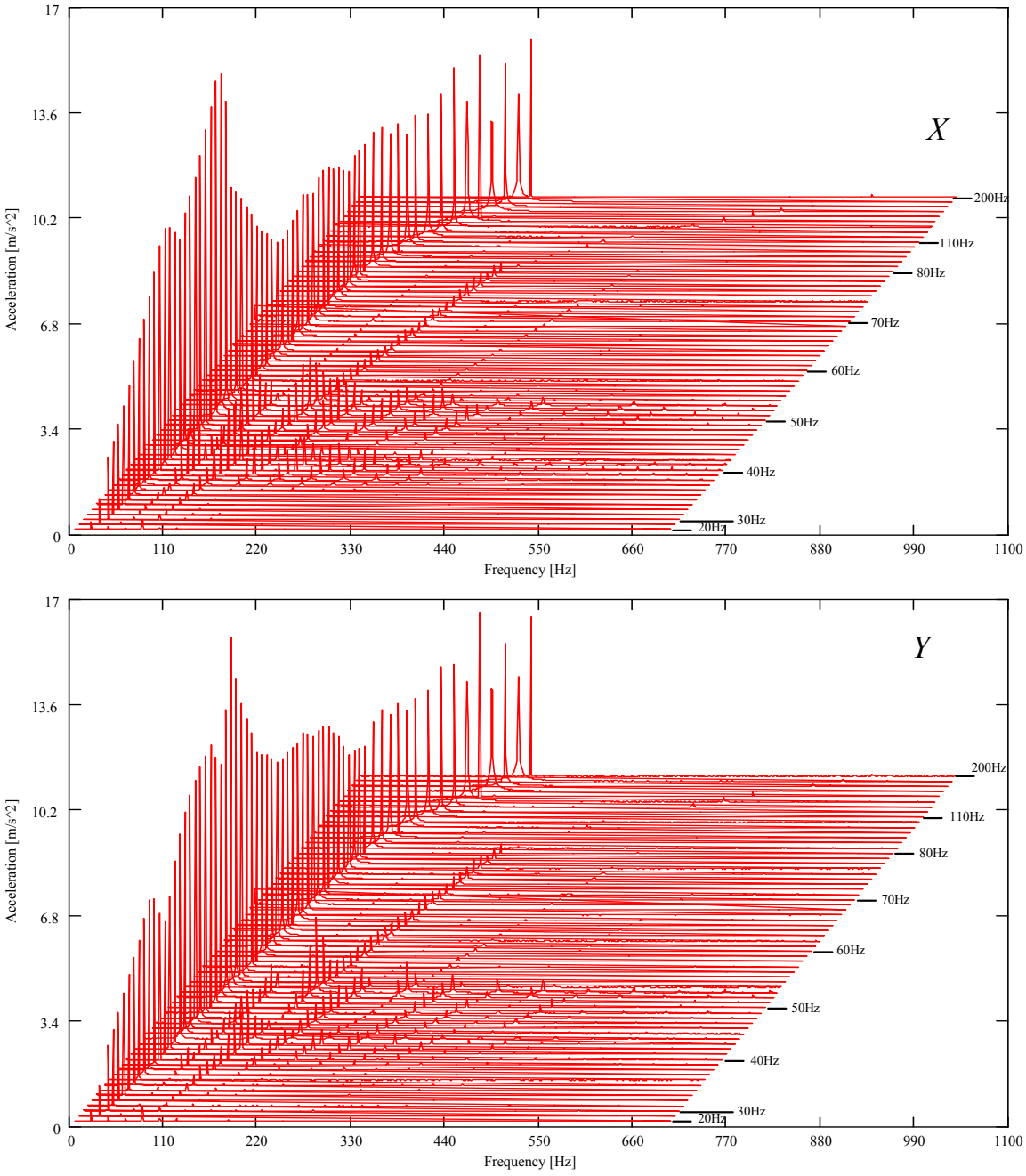

Figure 13 Waterfalls of acceleration response in the *X* and *Y* directions. (Dry SFD. end seal in place. L: 40 N)

Figure 14 depicts the amplitude of the dynamic excitation load in the *X* direction (similar in *Y*). Figure 15 and Figure 16 show the resulting synchronous displacements

along the *X* and *Y* directions, respectively. There are two peaks in response (natural frequencies), one at ~39 Hz and other ~50 Hz. The first natural frequency is associated to the motion of the main frame (see Figure 1), and the second natural frequency is associated to the motion of the steel rods supporting the SFD assembly. The effect of dry friction interaction between the mating surfaces of the mechanical seal is evident in the system response. There are a number of excitation frequencies in the *X* and *Y* directions where the system response suddenly drops, which represent transitions between slipping and sticking regimes of motion.

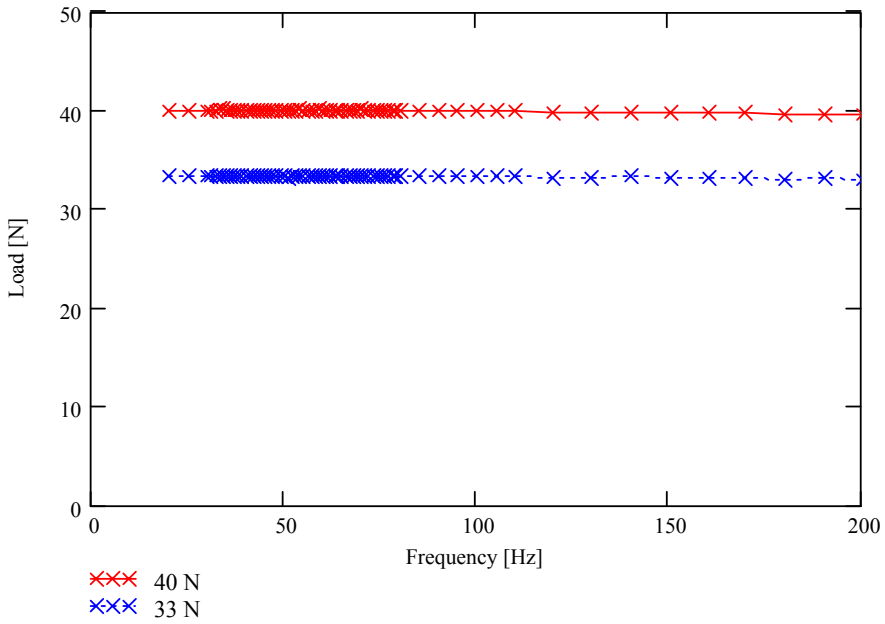

Figure 14 Amplitude of applied dynamic load, *X* direction. (Dry SFD, end seal in place)

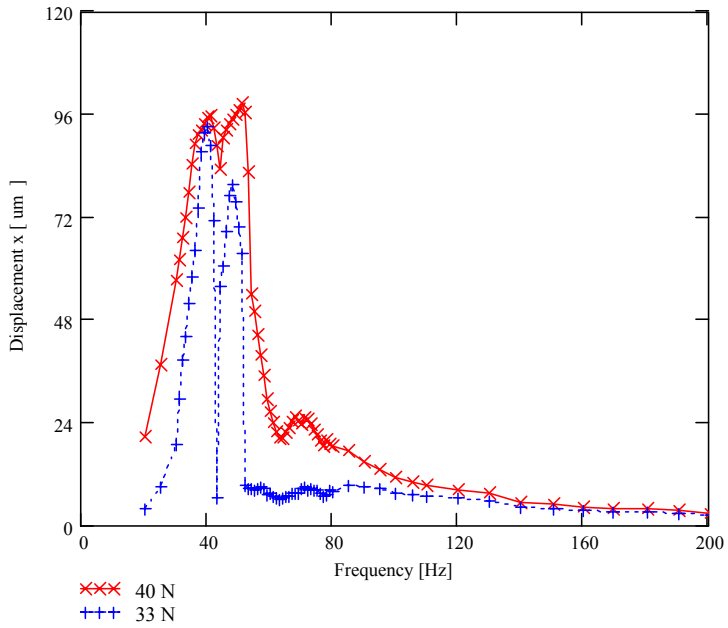

Figure 15 Synchronous frequency component of displacement response (X direction) due to a constant magnitude circular orbit excitation (40 N and 33 N). (Dry SFD, end seal in place)

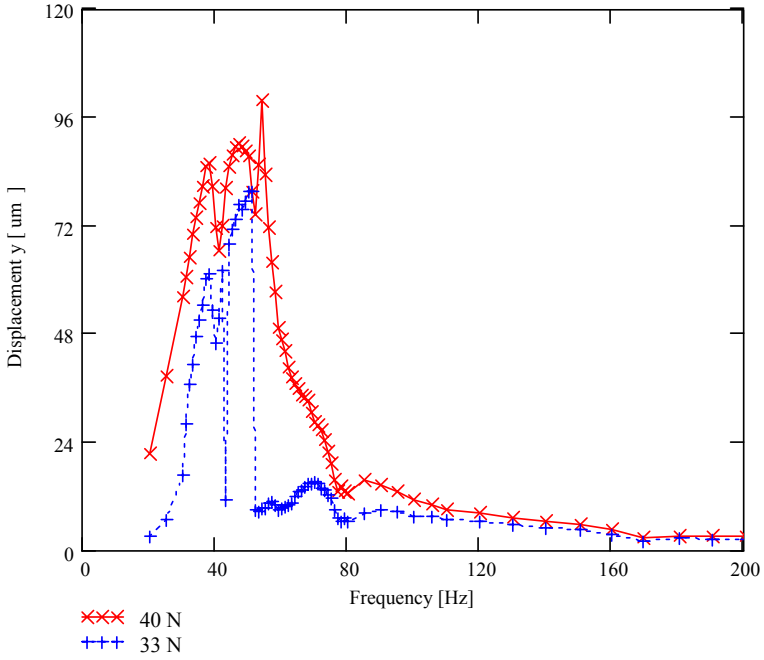

Figure 16 Synchronous frequency component of displacement response (*Y* direction)due to a constant magnitude circular orbit excitation (40 N and 33 N). (Dry SFD, end seal in place)

IV.4 Identification of dry friction force in contacting seal ring

The test system equivalent damping coefficient with the mechanical seal in place (dry system) is obtained by equating the work exerted by the external force to the energy dissipated by the system. The work exerted by the input external force is [20]

$$Work = \pi\left[\left|F_x\right|\left|X\right|\sin(\phi_1)+\left|F_y\right|\left|Y\right|\sin(\phi_2)\right] \tag{2}$$

where (F_x,F_y) and (X,Y) are the force and response vectors; ϕ_1 and ϕ_2 are the phase lag of the response relative to the force along the X and Y directions, respectively. The energy dissipated by dry friction is [20]

$$E_{dry} = F_\mu \int_{t_1}^{t_1+T} |V|\, dt \tag{3}$$

where V is the velocity vector (V_x,V_y) constructed from the displacement Fourier coefficients (no velocity data is directly available). On the other hand, some energy is also dissipated by (residual) viscous effects

$$E_{rv} = C_{rv}\int_{t_1}^{t_1+T}\left(V_x^{\,2}+V_y^{\,2}\right)dt \tag{4}$$

where $C_{rv} = C_s$ is a residual viscous damping coefficient from the support structure. The overall damping parameters are obtained assuming a combination of dry friction damping (arising from the end mechanical seal) and a residual viscous damping from other sources (i.e. steel rods, traces of oil entrapped in between ring carrier and Plexiglas bearing[3]). The identification relies on equating $E_{dry} + E_{rv}=Work$.

Table 4 shows the average of the identified friction force and equivalent viscous damping coefficient obtained from each test. The dry friction force (F_μ) and the residual viscous coefficients are obtained by finding the values that best fit the work executed by the external force (i.e. best correlation-r^2). The combination of the energy dissipated by

[3] The O-rings have to be lubricated upon assembly, which leaves oil traces in between the ring carrier and the Plexiglas bearing.

each the dry friction and the residual viscous damping account for the total energy dissipated by the system.

The friction force relates to the magnitude of the contact force at the mechanical seal interface. Thus, the friction force can be modified by either changing the compression of the wave spring that pushes the two seal surfaces together or by replacing the spring. The current contact force (i.e. normal force) at the seal interface is estimated at 70 N (± 10 N), and represents the minimum force required to create a proper mechanical sealing of the SFD section. The magnitude of the residual viscous damping coefficient (C_{rv}= 370 Ns/m) is similar (within ~10 %) to the one obtained from impact tests on the dry system without the seal in place (Table 3); thus representing the damping introduced by the support rods.

Table 4 Identified (averaged) dry friction force and equivalent viscous coefficients from single frequency excitation tests (20-200 Hz)

Test	Load(N)	Friction Force F_μ (N)	Residual Damping C_{rv}(N.s/m)	r^2
1	40	26	370	0.99
	35			0.99
2	40			0.98
	35			0.99
3	41			0.98
	35			0.99
4	40			0.98
	33			0.99

Figures 17 and 18 show the work exerted by the input force and the estimated energy dissipated by the combined (dry + viscous) damping model for each test. Figure 17 shows that the analytical model represents well the energy dissipated, even though the system shows stick-slip at certain frequencies.

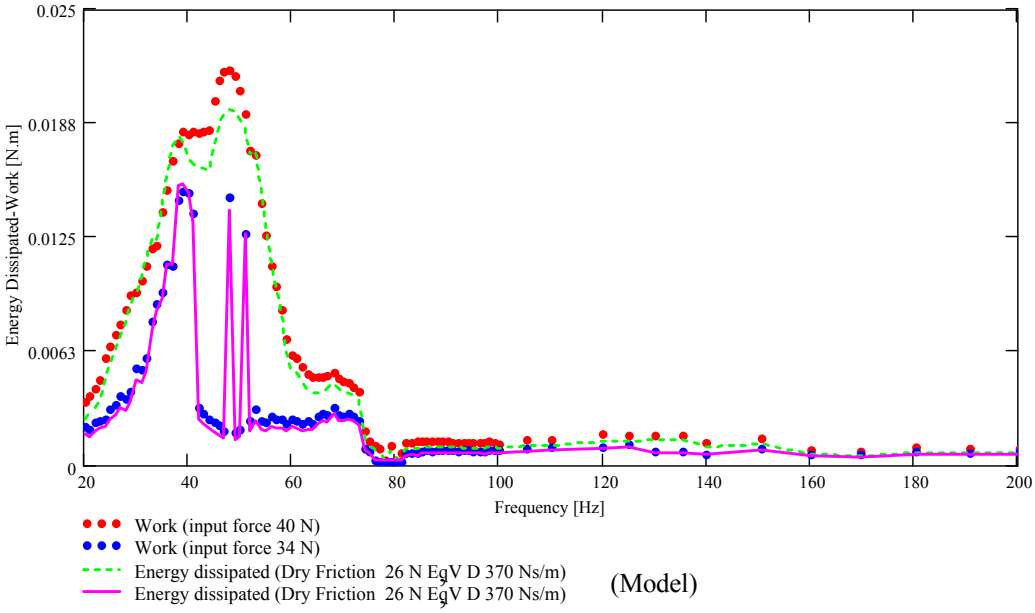

Figure 17 Work exerted by input force (= dissipated energy) estimated from combined damping model (Test 1). (Dry SFD, end seal in place)

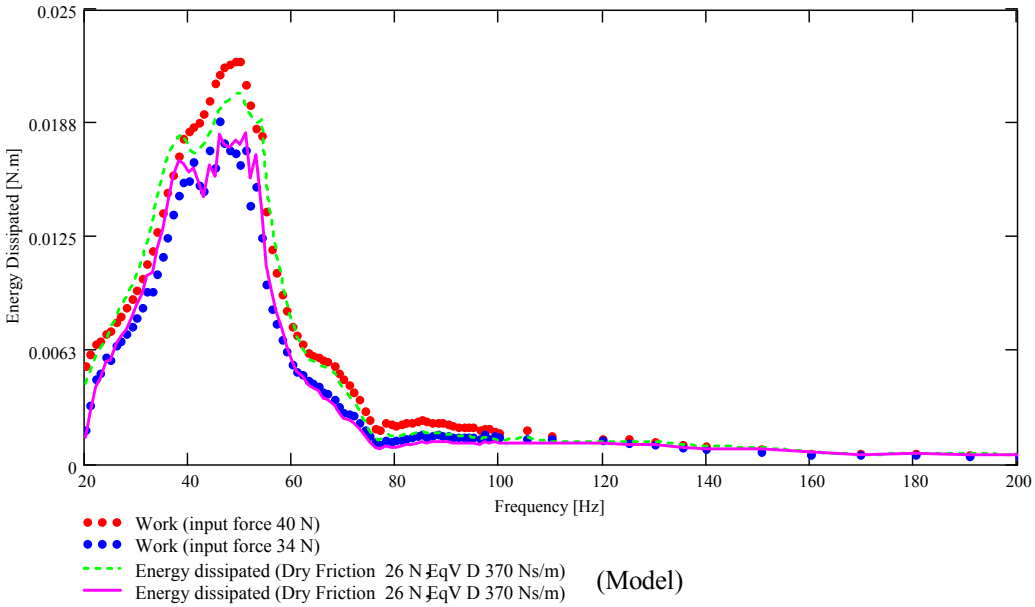

Figure 18 Work exerted by input force (= dissipated energy) estimated from combined damping model (Test 2). (Dry SFD, end seal in place)

Figure 19 presents the imaginary component of system transfer function (*F/X*) versus the excitation frequency, including the identified residual contribution ($C_{rv}\omega$, C_{rv}= 370 N.s/m). The Im(*F/X*) relates to the action of the dissipative forces on the system. For a purely viscous damping system, Im(*F/X*) = $C \times \omega$, a straight line with the damping coefficient (*C*) as its slope. In the figures *Im(F/X)* includes the effect of both dry friction and residual viscous damping. Notice that the viscous damping contribution, C_{rv}= 370 N.s/m, is rather small compared to the total damping of the dry system. This indicates that the damping arising from the seal dry friction interaction (F_{μ}= 26 N) accounts for most of the system energy dissipation.

Figure 20 shows the ratio Im(*F/X*)/ω. This magnitude represents the equivalent viscous damping coefficient for the dry system. Again, the residual damping coefficient (constant with frequency) represents a minute fraction of the overall system damping. Note that the damping arising from dry friction at the contact surface is lowest at frequencies from 40 to 50 Hz, which are precisely those at which the system peaked in motion; i.e. natural frequencies.

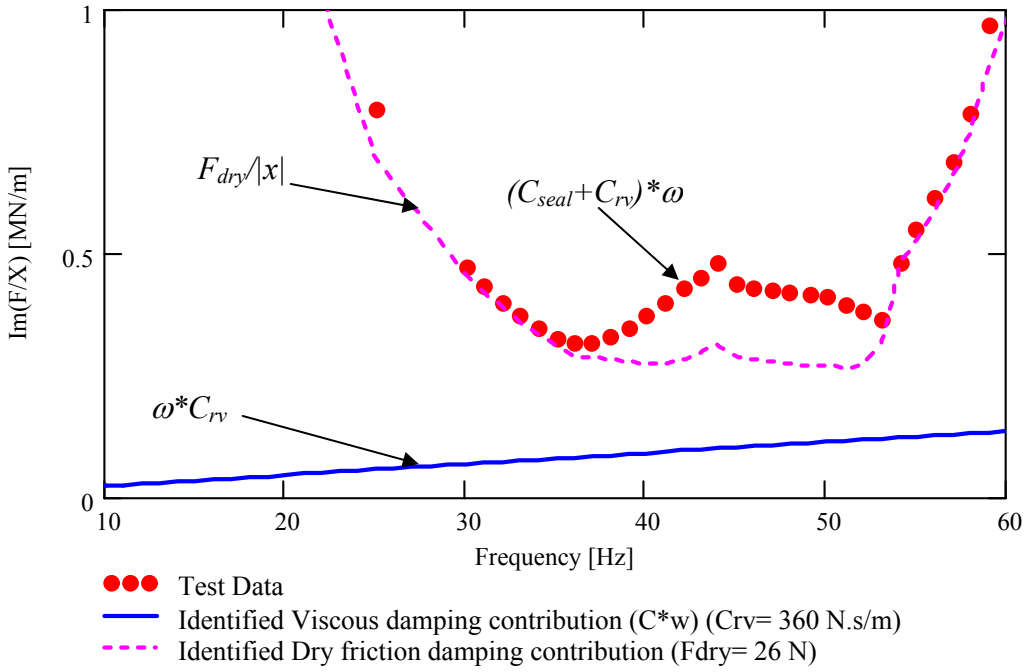

Figure 19 Imaginary component of transfer function, Im (*X/F*), vs excitation frequency. (Test 1- Dry SFD, end seal in place)

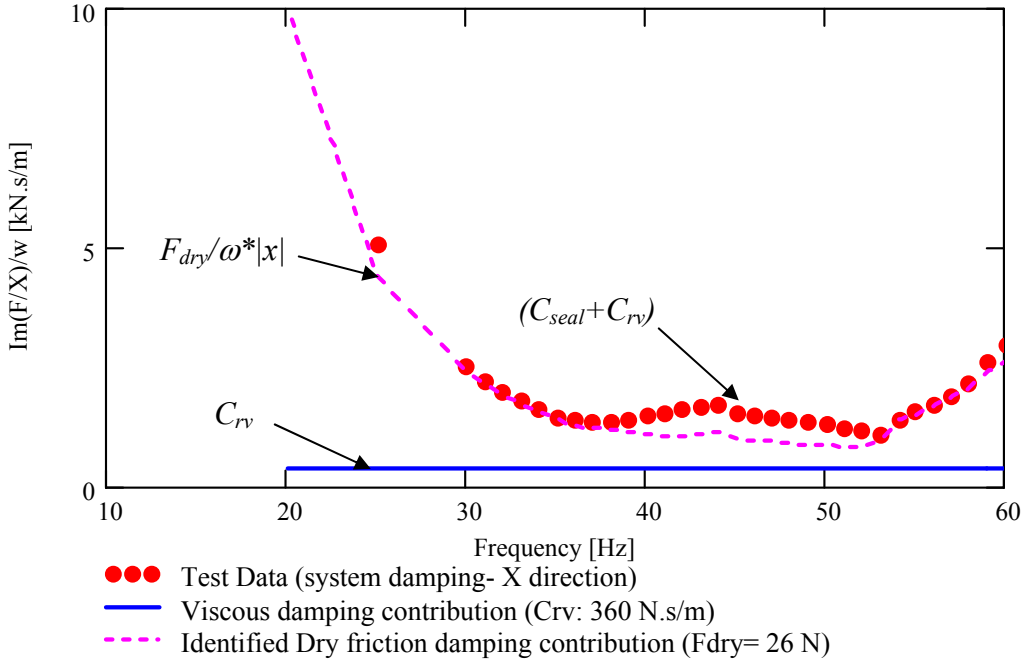

Figure 20 Equivalent viscous damping (dry friction + residual) vs excitation frequency. (Test1- Dry SFD, end seal in place)

V MEASUREMENTS OF FLOW RATE IN LUBRICATED SFD

After identifying the Coulomb friction parameter of the "dry" system, lubricant ISO VG 2 is pumped trough the SFD to asses the leakage performance of the end seal. The performance of the seal is determined by verifying that the mechanical seal assembly contact force effectively prevents leakage, and thus the recirculation annulus is completely filled with oil at all times. During the flow measurement tests the seal effectively prevented oil leakage, thus indicating that the contact force at the seal interface is sufficiently large to fully seal the damper.

Figure 21 depicts the combined results of flow versus pressure drop from three different set of tests, including five increasing oil inlet temperatures (21-43 ^{o}C). The pressure drop (differential) results from subtracting the pressure measured at the recirculation annulus from the pressure measured at the inlet of the damper. The measurements show that, as the oil temperature increases the flow increases relative to the pressure differential across the damper.

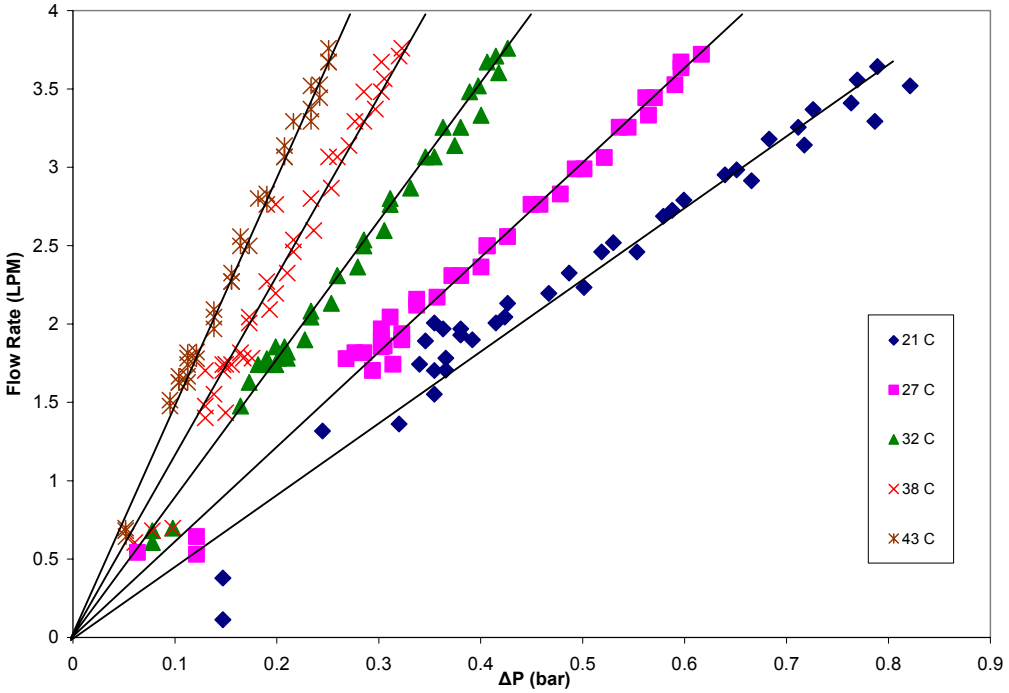

Figure 21 Lubricant Flow trough SFD vs. pressure differential for increasing oil temperatures

Figure 22 presents the pressure differential across the SFD versus the supply pressure. The pressure differential is clearly a linear function of the inlet pressure, and depends on the diameter of hole of the flow restrictors located at the discharge port in the recirculation annulus. Furthermore, the pressure at the recirculation annulus is close to ambient pressure (max P_r~ 1.12 bar). The through flow restriction consists of four pipe inserts, each with a 2.8 mm (0.11in) diameter through hole, that restrict the outlet flow at the recirculation annulus. Figure 23 depicts the location of one of the flow restrictors.

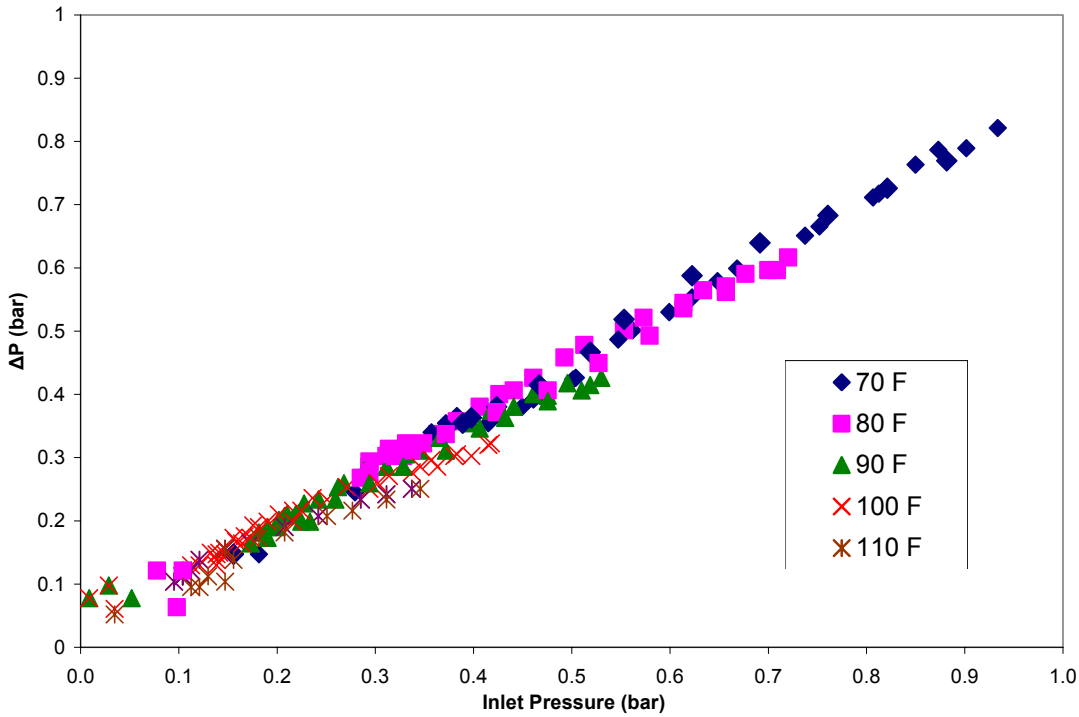

Figure 22 Pressure differential across the SFD versus inlet (supply) pressure for different temperatures (70 F-110 F)

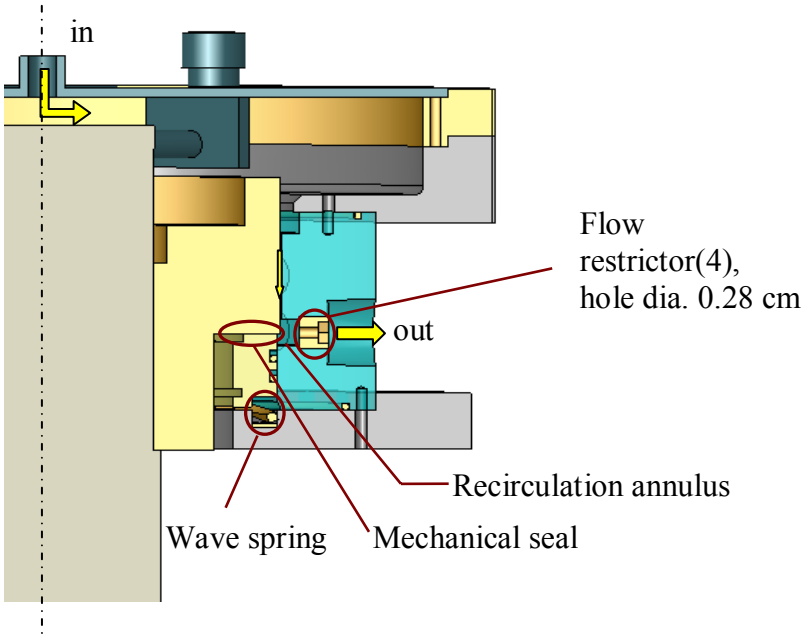

Figure 23 Cut view of SFD depicting flow restrictor.

Figure 24 shows the radial clearances measured after each test with lubricant temperatures at 21 ^{o}C, 27 ^{o}C and 32 ^{o}C. The clearance grows significantly with increasing oil temperatures. Figure 25 depicts a representation of the growth of the SFD bearing due to the raise in temperature, as obtained from a simple finite element model using COSMOS®. The radial growth is associated to an axial growth of the SFD land and a radial growth of the steel ring inside the SFD bearing that pushes the Plexiglas bearing.

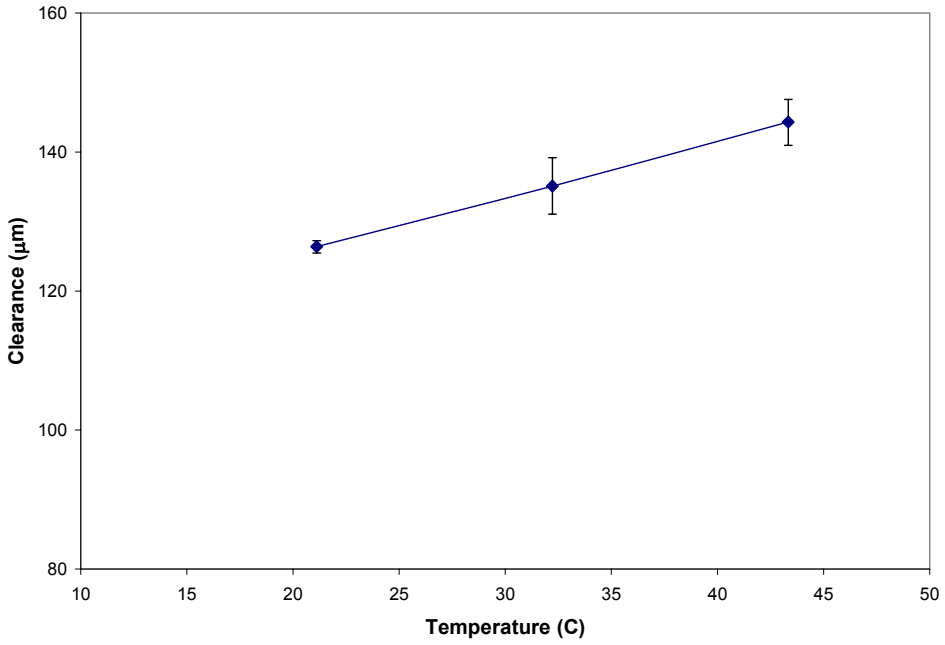

Figure 24 Measured radial clearance vs. lubricant temperature. (Nominal value *c*: 127 μm)

The analytical expression of the flow through the damper (centered journal) is [21]

$$Q = \frac{\pi D c^3}{12\mu(T)} \frac{\Delta P}{L} \tag{5}$$

where (c, D, L) are the damper radial clearance, diameter and length, respectively; ΔP is the pressure drop across the film land; and μ is the lubricant viscosity, a function of the mean film temperature (T).

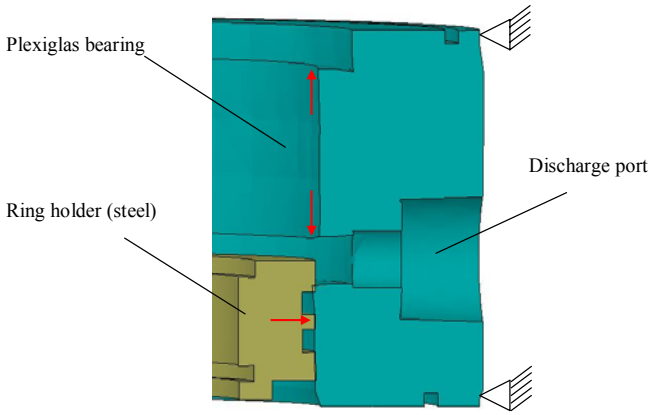

Figure 25 Representation of SFD deformation due to thermal stresses

A flow ratio is obtained by dividing the recorded flow rates by the analytical expression of flow through the damper (Eq (5)). Figure 26 shows the flow ratio as a function of the pressure differential ratio. The results are consistent, lying within a 16% band around the unit value for pressure drop ratio ($\Delta P/P_{max}$) greater than 0.4. However, the difference of the results from a unit value indicates the need for accurate values of viscosity from Eq.(1), and the clearance growth obtained experimentally. For lower pressure differentials the flow is too small for the instruments (i.e. flowmeters) to make an accurate measurement. However, since the flow is linear with pressure differential, the flow at pressure differentials less than 0.4 can be estimated by extrapolating the flow for greater pressure differentials.

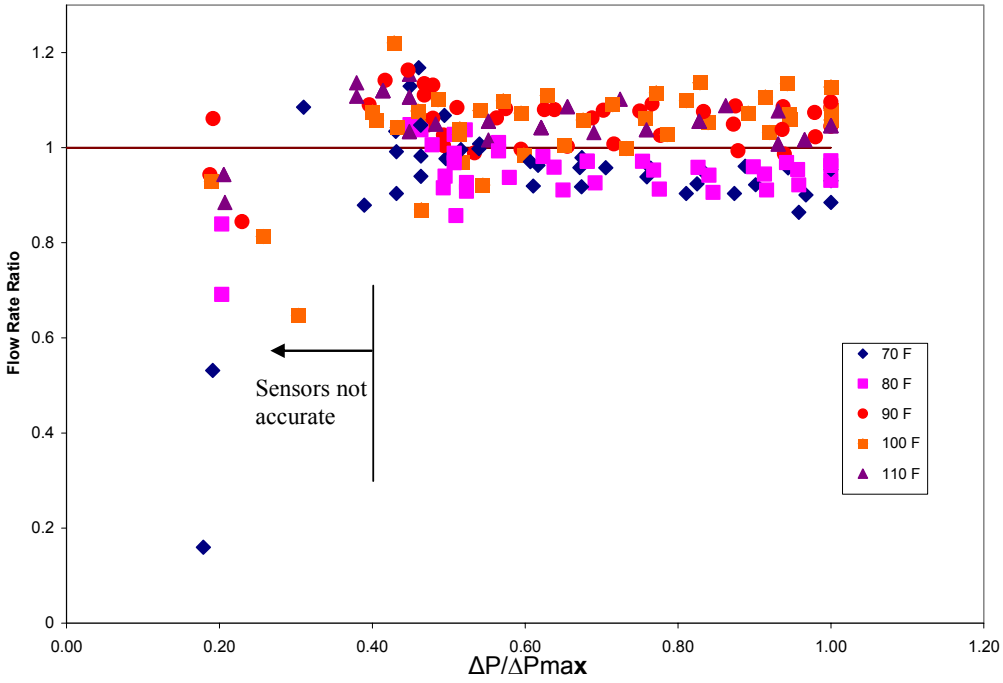

Figure 26 Ratio of test flow rate to predicted flow rate vs. pressure differential ratio

VI IDENTIFICATION OF DAMPING COEFFICIENTS FOR LUBRICATED SFD FROM SINGLE FREQUENCY FORCE EXCITATION RESPONSES

VI.1 Unidirectional tests

VI.1.1 Experimental procedure

The first experiments consist of unidirectional periodic excitation load tests, from 20 Hz to 60 Hz, along two orthogonal directions (i.e. *X* and *Y*). The tests include five increasing motion amplitudes (13 μm to 39 μm) at each excitation frequency. The bearing is initially centered within its journal. The SFD radial clearance is 127 μm ± 6 μm at the test temperature (23 ^{0}C). The DAQ system automatically adjusts the excitation load amplitude at each frequency to maintain the preset bearing displacements throughout the test frequency range. Maintaining a constant displacement or load magnitude provides a favorable scenario for the identification of systems that include dry friction [22]. Table 5 shows the test conditions and Appendix D includes recorded displacements at selected frequencies from 20 Hz to 60 Hz.

Table 5 Test conditions for dynamic load tests. Lubricated SFD

Inlet Pressure (P_s)	15.5 kPa (2.25 psi)
Outlet Pressure (P_r)	5.7 kPa (0.75 psi)
Frequency Range	20-60 Hz (5 Hz step)
Lubricant temperature (T)	23-25 ^{0}C (73-77 ^{0}F)
Viscosity (μ)	3.17 cP
Clearance (c)	127 μm (5 mils)
Displacement amplitude (radial)	13-38 μm (0.5-0.15 mils)

Figures 27 and 28 display waterfalls of load, displacement and acceleration for 13 μm and 39 μm dynamic displacements, respectively. Appendix D presents the displacement orbits for selected frequencies (20 Hz-60 Hz). The accelerations show a 3X super-synchronous component that evidences the presence of dry friction. The displacements also show a 3X component though very small when compared to the

synchronous component (>1%), a clear indication that the system operates in a macro-slip regime of motion.

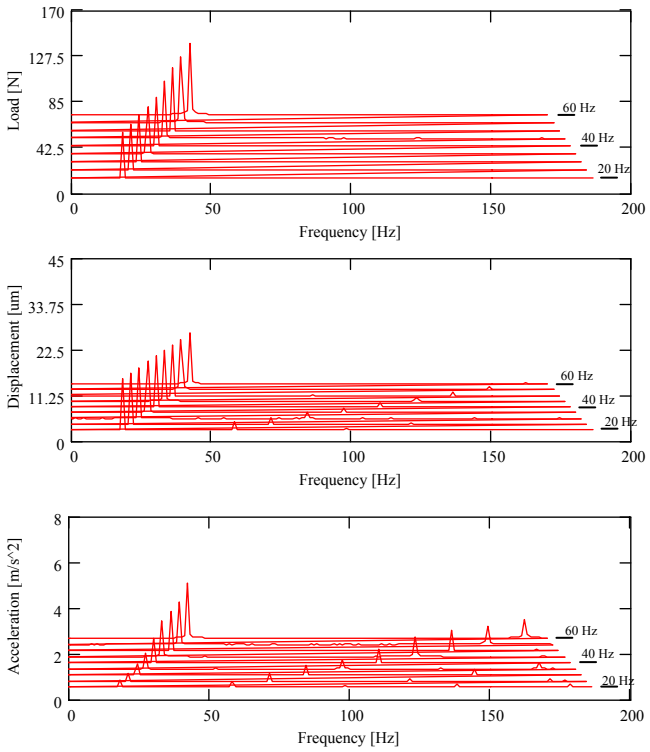

Figure 27 Waterfalls of *X*-excitation load, displacement and acceleration response from unidirectional dynamic tests (Displacement amplitude along *X* : 13 μm, lubricated SFD)

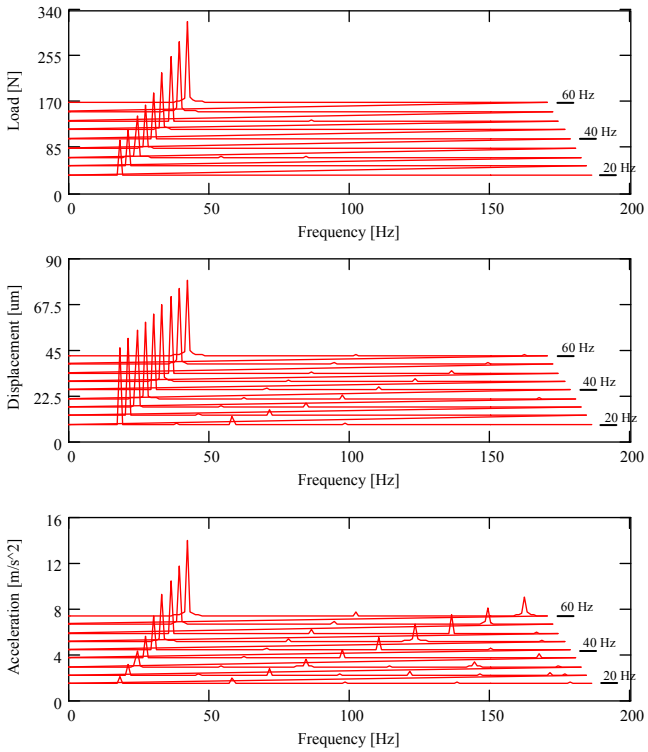

Figure 28 Waterfalls of *X*-excitation load, displacement and acceleration response from unidirectional dynamic tests (Displacement amplitude along *X* : 39 μm, lubricated SFD)

Figure 29 depicts the amplitudes of the applied dynamic load versus frequency. The load increases steadily with frequency to maintain constant preset displacements. The results demonstrate the system is overdamped, as the transfer function (*X/F*) does not show any resonance peak. Figure 30 shows the amplitudes of motion versus frequency for the five preset (constant) levels.

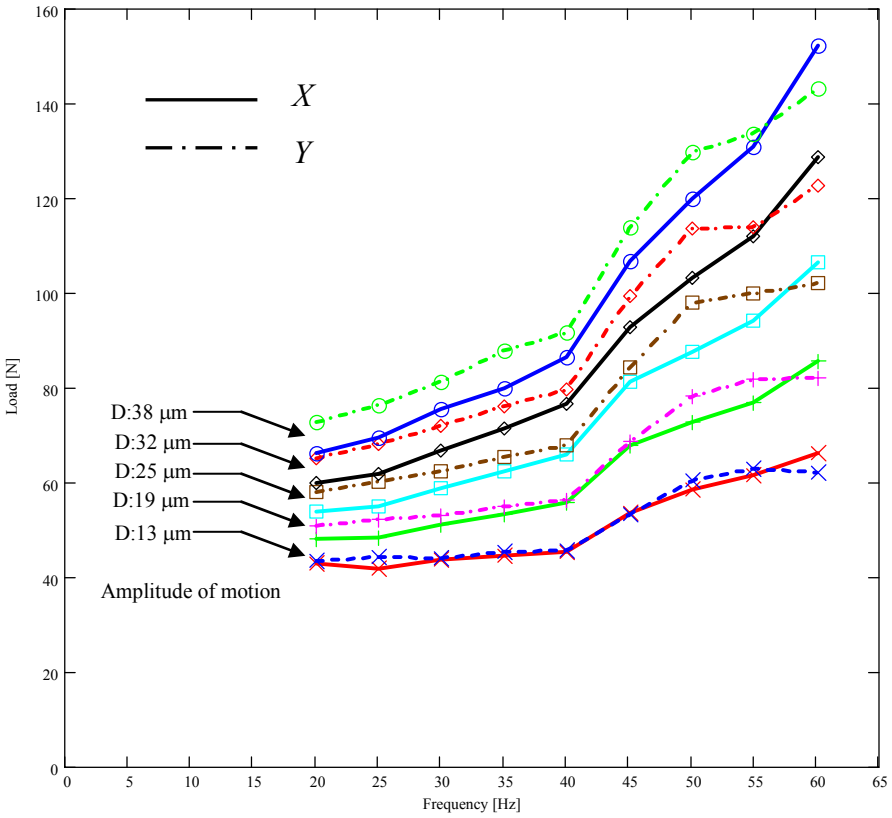

Figure 29 Amplitude of external dynamic Load vs excitation frequency (5 tests- *X* and *Y* directions, lubricated SFD)

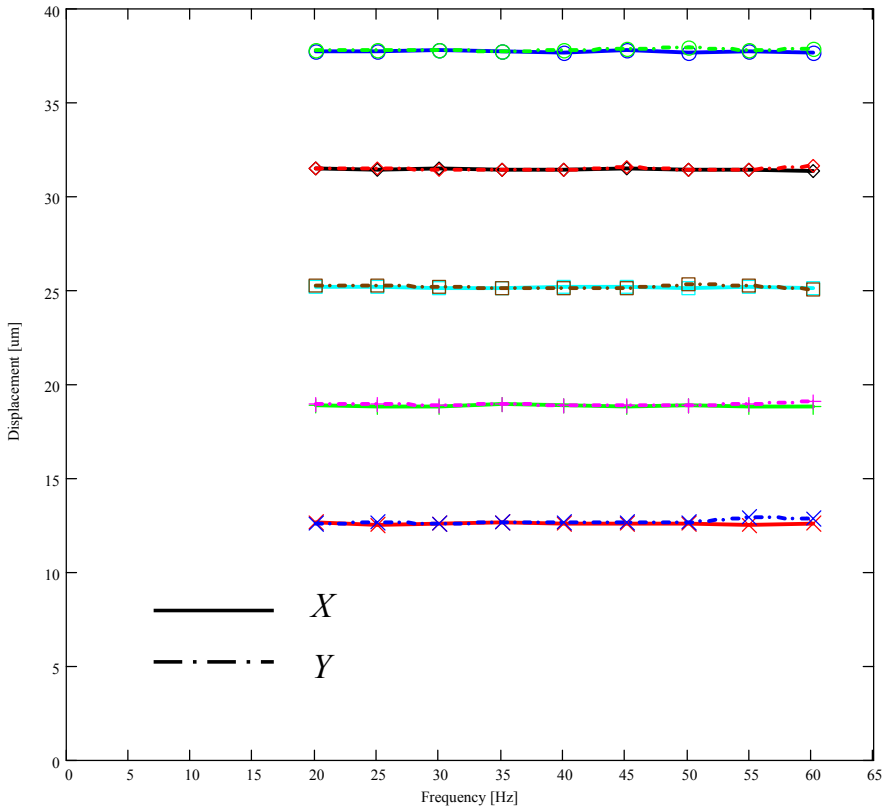

Figure 30 Fundamental amplitude of bearing motion vs excitation frequency. Periodic unidirectional load (5 tests- *X* and *Y* directions, lubricated SFD)

VI.1.2 Parameter identification method

The estimation of system parameters from unidirectional load excitations follows a simple procedure in the frequency domain. The equations of motion for the test bearing section are[4]

$$\begin{bmatrix} M+M_f & 0 \\ 0 & M+M_f \end{bmatrix} \begin{Bmatrix} \ddot{x} \\ \ddot{y} \end{Bmatrix} + \begin{bmatrix} K_{sx} & 0 \\ 0 & K_{sy} \end{bmatrix} \begin{Bmatrix} x \\ y \end{Bmatrix} = \begin{Bmatrix} F_x \\ F_y \end{Bmatrix} - \begin{Bmatrix} F_x \\ F_y \end{Bmatrix}_{seal} - \begin{Bmatrix} F_x \\ F_y \end{Bmatrix}_{SFD} \tag{6}$$

[4] In Eq.(6), M= 9.7 kg, K_{sx}=788 kN/m, K_{sy} = 823 kN/m as given in Tables 1-3.

M_f (0.62 ± 0.01 kg) represents the estimated mass of fluid enclosed in the plenum above the fluid film land section and in the recirculation annulus. This mass is estimated by forced displacing the lubricant inside the test section and weighing it.

The SFD reaction forces follow the linearized description:

$$\begin{Bmatrix} F_x \\ F_y \end{Bmatrix}_{SFD} = \begin{bmatrix} C_{xx} & C_{xy} \\ C_{yx} & C_{yy} \end{bmatrix} \begin{Bmatrix} \dot{x} \\ \dot{y} \end{Bmatrix} + \begin{bmatrix} D_{xx} & D_{xy} \\ D_{yx} & D_{yy} \end{bmatrix} \begin{Bmatrix} \ddot{x} \\ \ddot{y} \end{Bmatrix} \tag{7}$$

where $\{C_{\alpha\beta}\}_{\alpha\beta=x,y}$, $\{D_{\alpha\beta}\}_{\alpha\beta=x,y}$ are the damping and inertia force coefficients, respectively.

Recall that a squeeze film damper does <u>not</u> generate stiffness coefficients. Furthermore, as observed in preliminary testing, the cross-coupled damping and mass terms are negligible since the end seal effectively prevents air-entrapment into the damper at the test frequencies. Thus, the *X* and *Y* motions are uncoupled. For prediction purposes, the 2π-film (uncavitated) SFD model should be appropriate. The analysis also includes the residual viscous damping coefficient, C_{rv} ~ 370 N s/m (2.11 lbf s/in).

The dry friction force from contact at the mechanical seal equals

$$F_z = F_\mu sign(\dot{z}) = C_{seal_z}\dot{z}, \quad z = x, y \tag{8}$$

where *z* is a generic displacement along the *x* or *y* directions; and [20]

$$C_{seal_z} = \frac{4F_\mu}{\pi\omega|z|} \tag{9}$$

is the equivalent viscous coefficient for the mechanical seal.

In the frequency domain the system response is

$$\left[C_{tz} + \frac{i}{\omega}\left(\omega^2 M_{tz} - K_{sz}\right) \right] \dot{z}_{(\omega)} = F_{(\omega)} \tag{10}$$

where

$$M_{tz} = M_{zz} + M_f + D_{zz}, \text{ and } C_{tz} = C_{zz} + C_{seal_z} + C_{rv}, \quad z = x, y \tag{11}$$

and $z_{(\omega)}, F_{(\omega)}$ are the discrete Fourier Transform (DFT) of the time varying displacements and forces, respectively. In particular, a periodic forcing function can be represented as

$$F_z(t) = F_{zc}\cos(\omega t) + F_{zs}\sin(\omega t) = \left(F_{zc} - i\,F_{zs}\right)e^{i\omega t} = \bar{F}_z\, e^{i\omega t} \tag{12}$$

Subsequently, the displacement, velocity and acceleration are also periodic with identical frequency (ω), and expressed as

$$z_{(\omega)} = (z_c - i\,z_s)\,e^{i\omega t} = \mathbf{Z}\,e^{i\omega t};\ \dot{z} = i\omega\mathbf{Z}\,e^{i\omega t};\ \ddot{z} = -\omega^2\mathbf{Z}\,e^{i\omega t} \tag{13}$$

The system damping and mass parameters can be readily identified from Equation (10) as

$$C_{tz} = \mathrm{Re}\left(\frac{F_z}{\dot{z}}\right),\quad \left(K_{sz} - \omega^2 M_{Tz}\right) = -\omega\,\mathrm{Im}\left(\frac{F_z}{\dot{z}}\right),\ z=x,y \tag{14}$$

VI.1.3 Test results: dynamic force coefficients for lubricated system

This section presents the SFD added mass and damping force coefficients identified from the unidirectional periodic load tests with lubricant flowing through the damper. The squeeze film added inertia coefficients (D_{xx}, D_{yy}) are extracted from the dynamic stiffness for the largest amplitude of motion tested (38 μm), provided that the mass of the housing (M) and the mass of the fluid enclosed in the damper (M_f) are available.

Table 6 presents the estimated total mass coefficient and the resulting SFD inertia coefficient, and a prediction of the added inertia coefficient for an uncavitated squeeze film. The model predictive formula is

$$D_{xx} = D_{yy} = \frac{1}{2}\frac{\rho\pi R(2L)^3}{10c} \tag{15}$$

which delivers a more realistic value than that found in the archival literature [2]. The derivation of this formula is given by San Andrés [23].

Table 6 Inertia coefficient identified from unidirectional single frequency load tests (amplitude of motion: 38 μm, frequency range 20-60 Hz)

Parameter	*xx*	*yy*
Stiffness coefficient, (K_s)[kN/m]	788	823
Total Mass, (M_t) [kg]	19.7	18.4
Fluid Mass, (M_f) [kg]	0.62	
Housing Mass, (M) [kg]	9.7	
Added mass coefficient, (D) [kg]	**9.4**	**8.1**
R^2	0.98	0.96
Predicted added mass (D) [kg]	**8.2**	

Table 6 shows that the predicted added mass coefficient (8.2 kg) correlates well with the experimental values. Figure 31 shows the test derived dynamic stiffness for the 38 μm motion amplitude test, including the analytical model using the stiffness determined from static load and impact load tests and the total mass given in Table 4. The reported mass coefficient is determined using the largest amplitude of motion (38 μm). Appendix E reports the SFD added mass coefficients identified for other test amplitudes of motion.

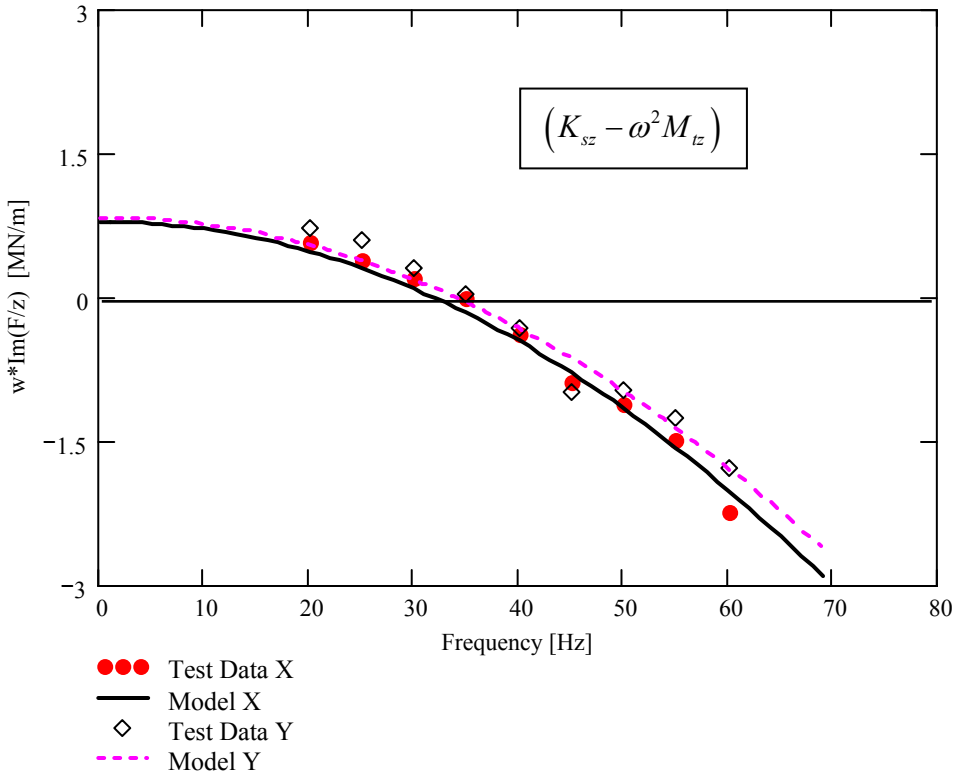

Figure 31 Dynamic stiffnesses from unidirectional load (single frequency) excitation tests and analytical model (*D*: 39 μm, K_{sx}= 788 kN/m, K_{sy}= 823 kN/m, M_{txx}= 19.7, M_{tyy}= 18.4, lubricated SFD)

Figures 32 through 35 depict the test system and SFD (alone) damping coefficients identified at each excitation frequency. The total system damping combines the damping from the mechanical seal (Coulomb-type damping), the viscous squeeze film, and the residual structure viscous damping. The test results show that the system is highly over damped.

The "viscous" damping arising from dry friction is inversely proportional to the amplitude of motion and excitation frequency, i.e. $C_{seal} \sim F_{\mu}/(\omega|z|)$. Therefore, "dry friction" damping is dominant at low frequencies and small amplitude of motions. On the other hand, the squeeze film damping coefficient is expected to be independent of excitation frequency, albeit a function of the amplitude of dynamic displacement.

Figures 32 and 33 depict the total identified viscous damping coefficients (C_{tx}, C_{ty}) for the largest and smallest amplitudes (13 μm and 38 μm) of motion versus excitation frequency, respectively. For both dynamic displacements, the system damping coefficients decrease with frequency, but for the 13 μm displacement amplitude the damping is considerably higher at low frequencies; thus confirming the significant contribution of the mechanical seal dry friction to the overall viscous damping.

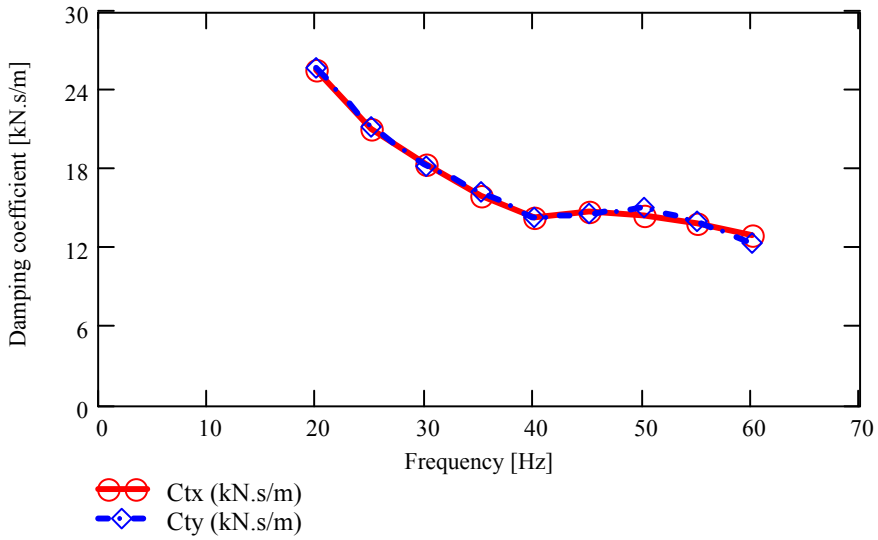

Figure 32 Identified system damping coefficients (C_{tx}, C_{ty}) versus excitation frequency. Unidirectional load tests (Displacement amplitudes along *X* and *Y* : 13 μm, lubricated SFD)

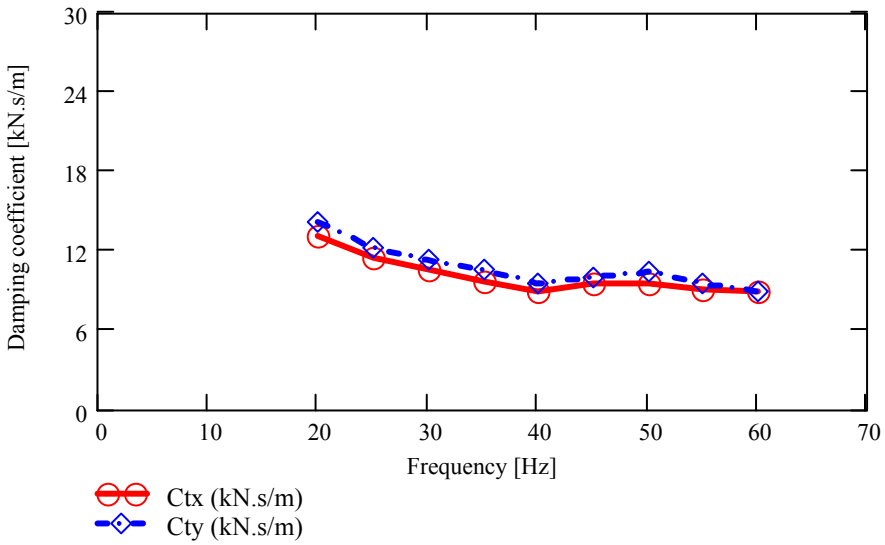

Figure 33 Identified system damping coefficients (C_{tx}, C_{ty}) versus excitation frequency. Unidirectional load tests. (Displacement amplitudes along *X* and *Y*: 38 μm, lubricated SFD)

Subtracting the "dry friction" damping (C_{seal}) and residual damping (C_{rv}) from the system damping coefficients, yields the viscous damping coefficient for the squeeze film alone, i.e. $C_{xx}=C_{tx}-C_{seal}-C_{rv}$. Figures 34 and 35 depict the squeeze film damping coefficients (C_{xx}, C_{yy}) extracted from the 13 μm and 38 μm dynamic displacement tests, respectively. The film damping coefficients ($C_{xx,}$ C_{yy}) are nearly constant and similar for both displacement amplitudes. Appendix F presents the identified viscous coefficients for all the frequencies and amplitudes of motion tested.

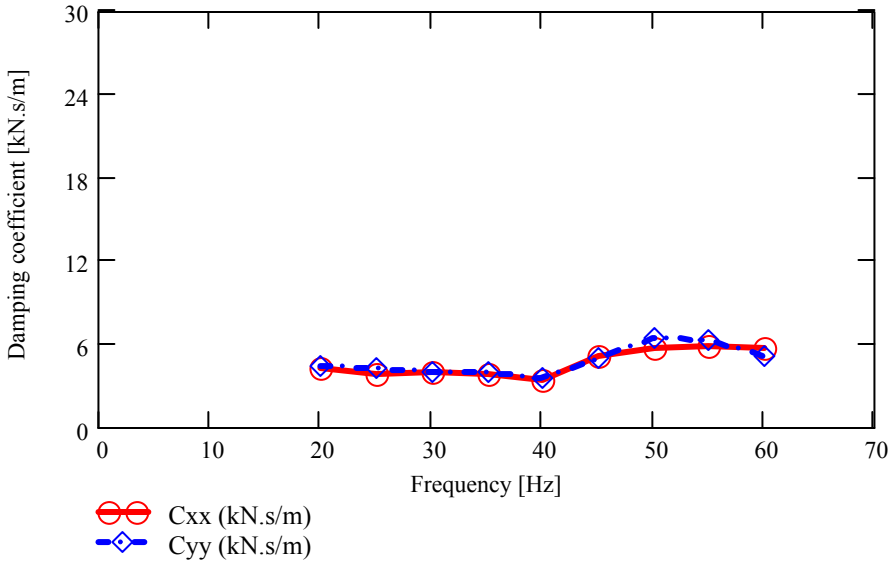

Figure 34 SFD damping coefficients (C_{xx}, C_{yy}) versus excitation frequency. Unidirectional load tests. (Displacement amplitudes along *X* and *Y*: 13 μm, lubricated SFD)

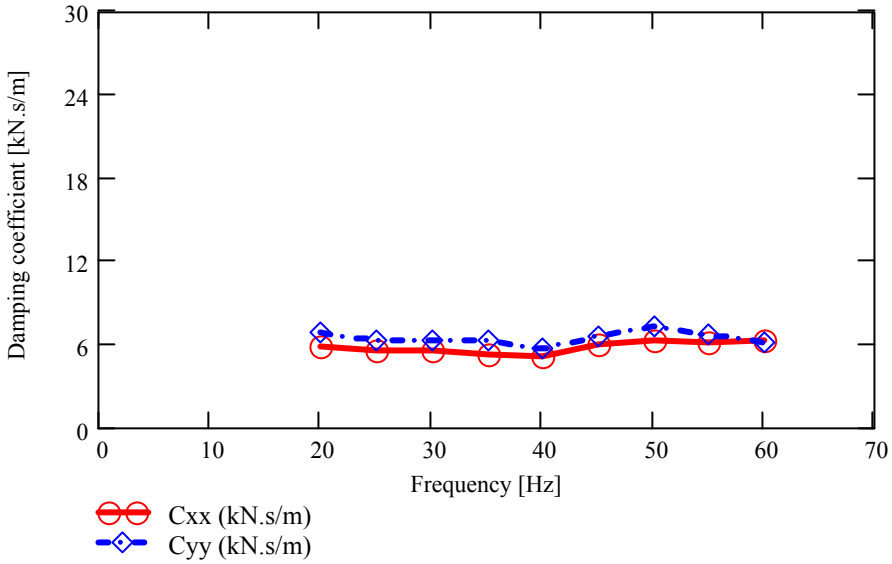

Figure 35 SFD damping coefficients (C_{xx}, C_{yy}) versus excitation frequency. Unidirectional load tests. (Displacement amplitudes along *X* and *Y*: 38 μm, lubricated SFD)

Figure 36 depicts the system total damping coefficients (C_{tx}, C_{ty}) versus displacement amplitude for excitations at 20 Hz and 60 Hz. (C_{tx}, C_{ty}) magnitudes are largest for the smallest amplitudes of dynamic motion, in particular at the lowest test frequency, thus

evidencing the effect of dry friction interaction upon the dissipation features of the system.

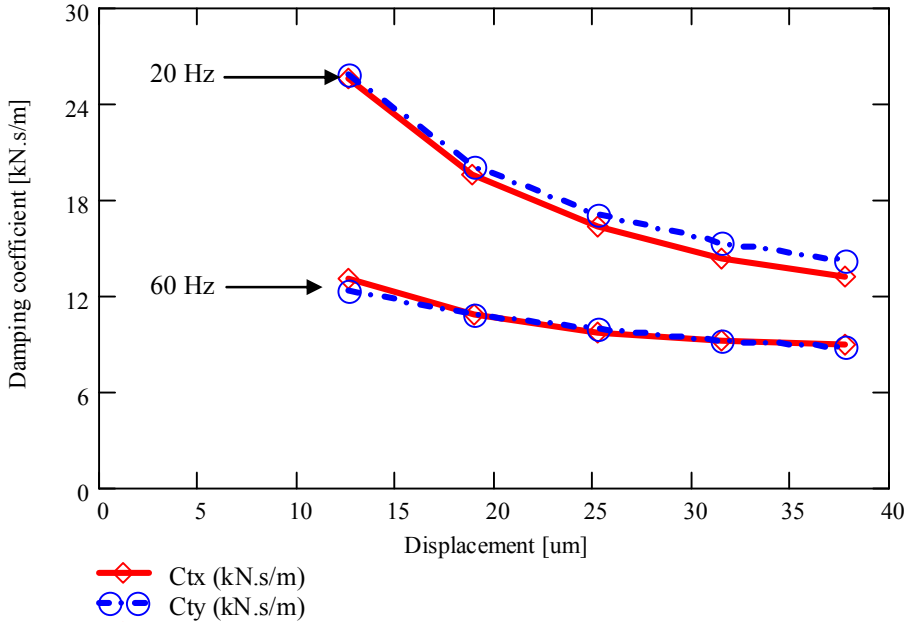

Figure 36 Identified system damping coefficients (C_{tx}, C_{ty}) versus displacement amplitude. Unidirectional load tests. (Excitation Frequency: 20 Hz and 60 Hz, lubricated SFD)

Figures 37 and 38 depict the squeeze film damping coefficients (C_{xx}, C_{yy}) and model predictions versus displacement amplitude for the lowest and highest excitation frequencies, 20 Hz and 60 Hz, respectively. The short length, open ends bearing formula for damping coefficient is [2]

$$C_{rr} = \mu D \left(\frac{L}{c}\right)^3 \frac{\pi\left(1+2\varepsilon^2\right)}{2\left(1-\varepsilon^2\right)^2} \tag{16}$$

This formula considers a full film and is derived from small amplitude unidirectional motions about a static journal eccentricity ratio ($\varepsilon = e/c$). The test derived squeeze film damping coefficients (C_{xx}, C_{yy}) increase slightly with the amplitude of motion, though less pronouncedly than the model predictions. The test results at 60 Hz evidence invariant damping coefficients. For both frequencies, the simple model predictions are

in good agreement with the identified coefficients. The average value of viscous damping is 6,000 Ns/m (34. 3 lbf.s/in).

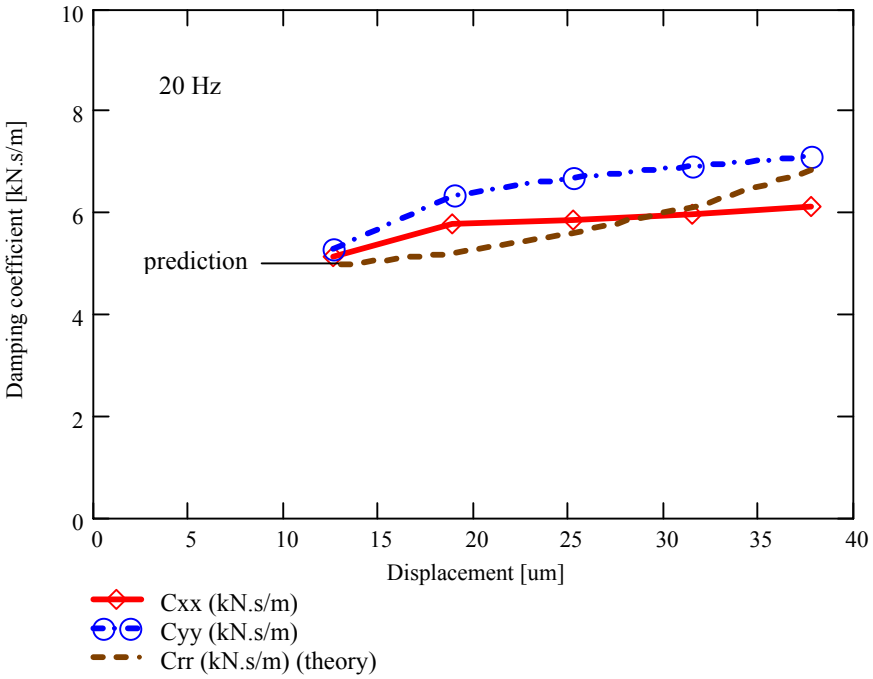

Figure 37 Squeeze film damping coefficients (C_{xx}, C_{yy}) versus displacement amplitude. Unidirectional load tests. (Excitation Frequency: 20 Hz, lubricated SFD)

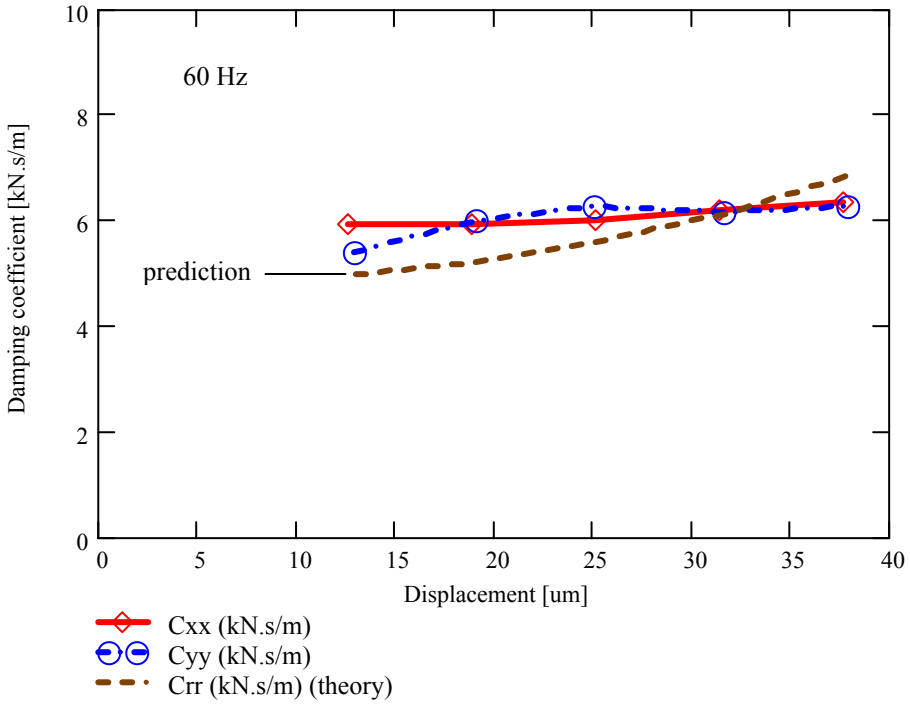

Figure 38 Squeeze film damping coefficients (C_{xx}, C_{yy}) versus displacement amplitude. Unidirectional load tests. (Excitation Frequency: 60 Hz, lubricated SFD)

VI.2 Circular orbit tests

The second set of experiments consists of single frequency dynamic loads exciting centered circular orbits (CCO) from 20 Hz to 60 Hz. The tests include four increasing motion amplitudes (12 μm to 50 μm) at each excitation frequency. Table 7 presents the test conditions. A series of adjustments between the linear motion and circular tests lead to a new estimation of the dry friction force calculated in the section IV. The calculation is detailed in Appendix G. The resulting friction force is 30 N instead of 26 N.

Table 7 Test conditions for Dynamic load Tests (CCO). Lubricated SFD

Inlet Pressure (P_s)	15.5 kPa (2.25 psi)
Outlet Pressure (P_r)	5.7 kPa (0.75 psi)
Frequency Range	20-60 Hz (10 Hz step)
Lubricant temperature (T)	23-25 ^{0}C (73-77 ^{0}F)
Viscosity (μ)	3.17 cP
Clearance (c)	127 μm (5 mils)
Displacement amplitude (radial)	12-50 μm (0.5-2 mils)

Following the procedure from unidirectional tests, the applied dynamic load is set to maintain constant amplitude circular orbits throughout the test frequency range for each amplitude level (12 μm, 25 μm to, 38 μm, 50 μm). Figures 39 and 40 show the forces and displacement orbits (Y vs. X) at 20 Hz for the four displacement amplitude tested, respectively. Appendix H includes displacements and excitation force orbits at other selected frequencies from 20 Hz to 60 Hz.

Figures 41 and 42 show the amplitudes of the dynamic load and the ensuing orbit radius versus frequency. The dynamic load increases steadily with frequency in order to maintain the design (preset) constant orbit amplitude.

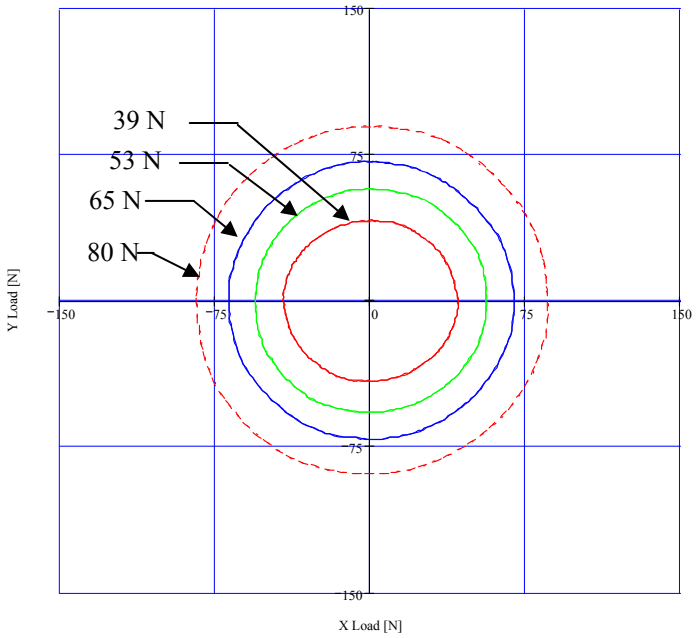

Figure 39 Dynamic excitation load orbits for four amplitude levels. (20 Hz, lubricated SFD)

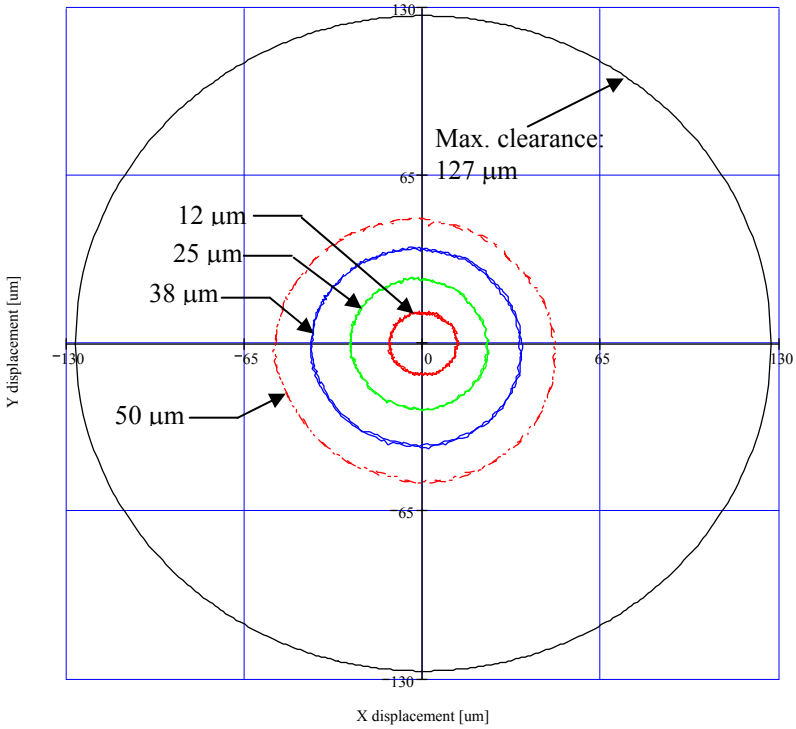

Figure 40 Displacement orbits for four amplitude levels and maximum clearance orbit. (20 Hz, lubricated SFD, CCO)

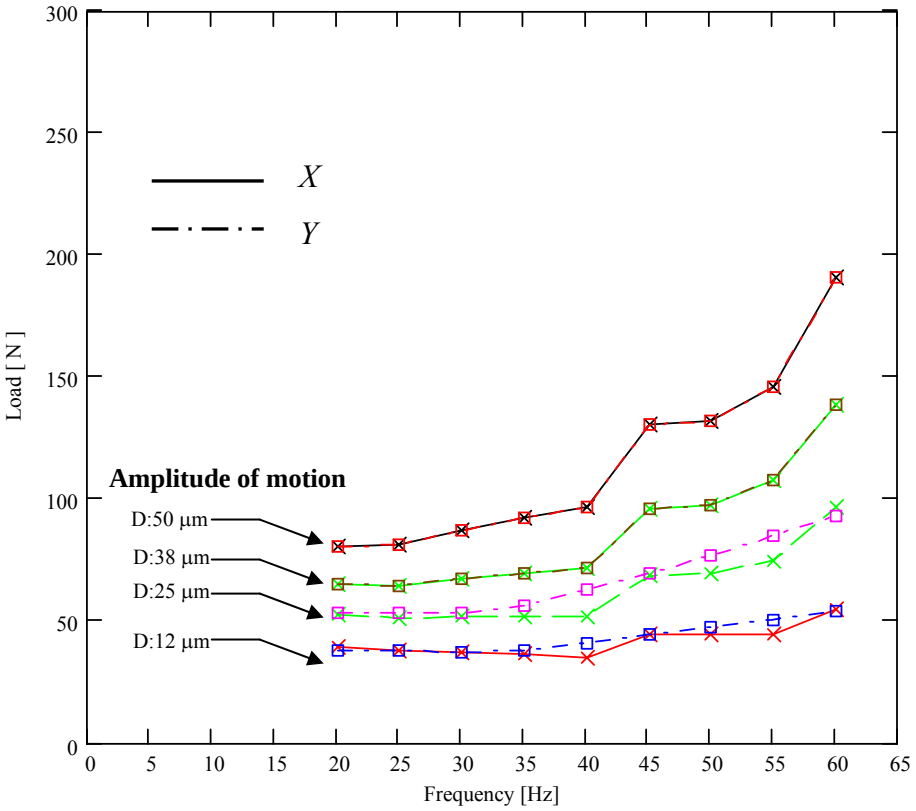

Figure 41 Amplitude of external dynamic Load vs excitation frequency (4 tests- CCO, lubricated SFD)

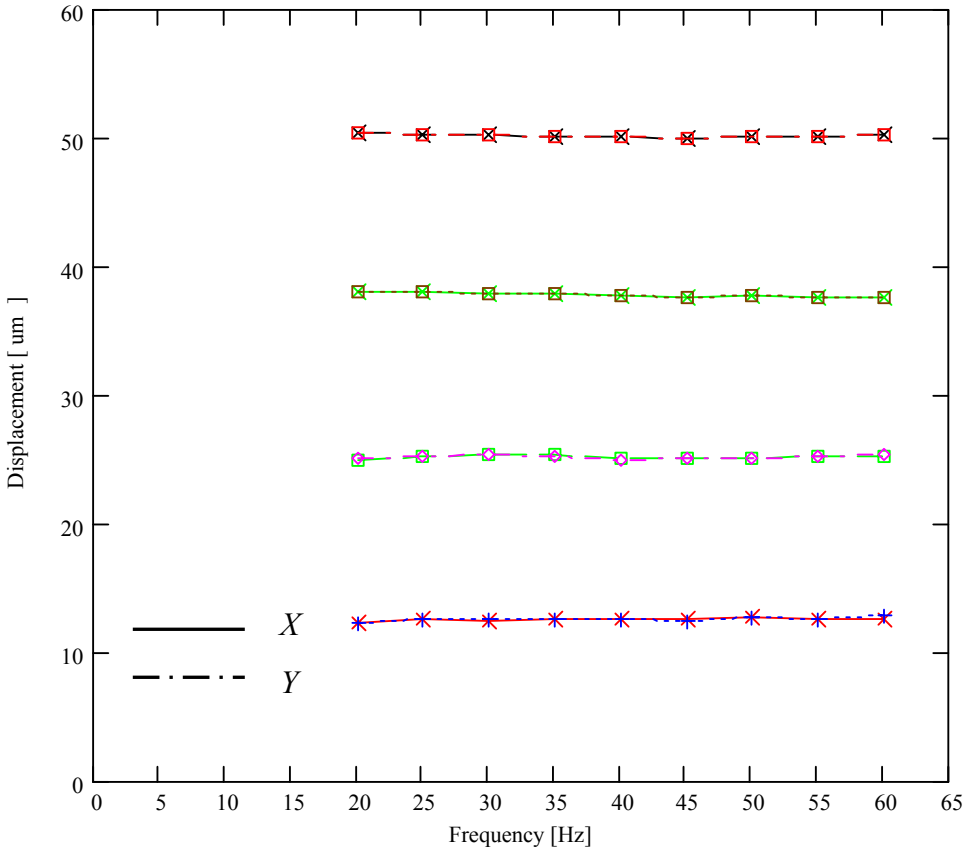

Figure 42 Fundamental amplitude (radius) of bearing circular motion vs excitation frequency. (4 tests- CCO, lubricated SFD)

VI.2.1 Parameter identification method

This section describes the identification method employed to estimate the SFD parameters from centered circular orbit tests. As presented in section VI.1.2, the equations of motion for the test bearing section are[5]

$$\begin{bmatrix} M+M_f & 0 \\ 0 & M+M_f \end{bmatrix} \begin{Bmatrix} \ddot{x} \\ \ddot{y} \end{Bmatrix} + \begin{bmatrix} K_{sx} & 0 \\ 0 & K_{sy} \end{bmatrix} \begin{Bmatrix} x \\ y \end{Bmatrix} = \begin{Bmatrix} F_x \\ F_y \end{Bmatrix} - \begin{Bmatrix} F_x \\ F_y \end{Bmatrix}_{seal} - \begin{Bmatrix} F_x \\ F_y \end{Bmatrix}_{SFD} \tag{17}$$

[5] In Eq. (17), M= 9.7 kg, K_{sx}=788 kN/m, K_{sy} = 823 kN/m as given in Tables 1-3.

where M_f (0.62 ± 0.01 kg) represents the estimated mass of fluid enclosed in the plenum above the fluid film land section and in the recirculation annulus.

The SFD reaction forces follow the linearized description:

$$\begin{Bmatrix} F_x \\ F_y \end{Bmatrix}_{SFD} = \begin{bmatrix} C_{xx} & C_{xy} \\ C_{yx} & C_{yy} \end{bmatrix} \begin{Bmatrix} \dot{x} \\ \dot{y} \end{Bmatrix} + \begin{bmatrix} D_{xx} & D_{xy} \\ D_{yx} & D_{yy} \end{bmatrix} \begin{Bmatrix} \ddot{x} \\ \ddot{y} \end{Bmatrix} \tag{18}$$

where $\{C_{\alpha\beta}\}_{\alpha\beta=x,y}$, $\{D_{\alpha\beta}\}_{\alpha\beta=x,y}$ are the damping and inertia force coefficients, respectively. The seal force is expressed as

$$\begin{Bmatrix} F_x \\ F_y \end{Bmatrix}_{seal} = \begin{bmatrix} F_\mu & 0 \\ 0 & F_\mu \end{bmatrix} \begin{Bmatrix} \dot{x} \\ \dot{y} \end{Bmatrix} \frac{1}{\sqrt{\dot{x}^2 + \dot{y}^2}} = C_{seal} \begin{Bmatrix} \dot{x} \\ \dot{y} \end{Bmatrix} \tag{19}$$

where C_{seal} is an equivalent viscous parameter that follows from equating the energy dissipated by viscous and dry friction forces.

$$C_{seal} \int V^2 dt = F_\mu \int V sign(V) dt \tag{20}$$

In the frequency domain the system can be represented as

$$\left[-\omega^2 \boldsymbol{M} + i\omega \boldsymbol{C} + \boldsymbol{K} \right] Z_{(\omega)} = \underline{H}_{(\omega)} Z_{(\omega)} = F_{(\omega)} \tag{21}$$

where

$$\boldsymbol{M} = \begin{bmatrix} M + M_f + D_{xx} & D_{xy} \\ D_{yx} & M + M_f + D_{yy} \end{bmatrix}, \boldsymbol{K} = \begin{bmatrix} K_{s_x} & 0 \\ 0 & K_{s_y} \end{bmatrix}, \boldsymbol{C} = \begin{bmatrix} C_{xx} + C_{seal} & C_{xy} \\ C_{yx} & C_{yy} + C_{seal} \end{bmatrix} \tag{22}$$

and $Z_{(\omega)}, F_{(\omega)}$ are the discrete Fourier Transform (DFT) of time varying displacements and forces, respectively. In particular, a periodic forcing function can be represented as

$$\begin{aligned} F_x(t) &= F_{xc}\cos(\omega t) + F_{xs}\sin(\omega t) = \left(F_{xc} - i F_{xs} \right) e^{i\omega t} = \overline{F}_x e^{i\omega t} \\ F_y(t) &= F_{yc}\cos(\omega t) + F_{ys}\sin(\omega t) = \left(F_{yc} - i F_{ys} \right) e^{i\omega t} = \overline{F}_y e^{i\omega t} \end{aligned} \tag{23}$$

Subsequently, the bearing displacement and accelerations are also periodic with identical frequency (ω), and are expressed as

$$Z_{(\omega)} = \begin{Bmatrix} x \\ y \end{Bmatrix} = \begin{Bmatrix} x_c - i\,x_s \\ y_c - i\,y_s \end{Bmatrix} e^{i\omega t} = \begin{Bmatrix} \bar{x} \\ \bar{y} \end{Bmatrix} e^{i\omega t}\ ;\ \begin{Bmatrix} \ddot{x} \\ \ddot{y} \end{Bmatrix} = \begin{Bmatrix} \bar{a}_x \\ \bar{a}_y \end{Bmatrix} e^{i\omega t} \tag{24}$$

In Eq.(21) the impedance matrix ($\underline{\underline{H}}_{(\omega)}$) includes four coefficients, which are complex algebraic functions of the excitation frequency (ω). Rearranging Eq. (21) yields

$$H_{xx}\left(\frac{x}{F_x}\right) + H_{xy}\left(\frac{y}{F_x}\right) = H_{yy}\left(\frac{y}{F_y}\right) + H_{yx}\left(\frac{x}{F_y}\right) = 1 \tag{25}$$

where (x/F_x)and (y/F_y) are the direct transfer functions, and (y/F_x) and (x/F_y) are the cross transfer functions of the test system. For circular centered orbits with no evidence of cavitation or air entrapment, the system (structurally isotropic) is expected to yield similar transfer functions. Indeed, the experimental results (see Appendix I) show that the direct transfer functions are similar in magnitude and phase, and the cross transfer functions are similar in magnitude with inverted phase. Thus, from experimental verification

$$H_d = H_{xx} = H_{yy}, \quad H_c = H_{xy} = -H_{yy} \tag{26}$$

then the system impedances become

$$H_d = \frac{2}{\frac{x}{F_x} + \frac{y}{F_y}}, \quad H_c = \frac{1 - H_d \frac{x}{F_x}}{\frac{y}{F_y}} \tag{27}$$

Appendix G shows that the cross impedance (H_c) is negligible when compared to the direct impedance (H_d). Thus cross coupled coefficients, as expected, are negligible.

The fluid inertia coefficients (D_D=$D_{xx,}$ D_{yy}) are identified from the dynamic stiffness obtained from the real component of the direct impedance,

$$\left(K_s - \left(M + D_D\right)\omega^2\right) = \mathrm{Re}\left(H_D\right) \tag{28}$$

The damping coefficient is identified from the imaginary components of the direct impedance as

$$C_D = \frac{\mathrm{Im}\left(H_D\right)}{\omega} = C_{xx} = C_{yy}$$

where

$$C_D = C_{SFD} + C_{seal} + C_{rv} \tag{29}$$

is the combined system total direct damping, comprising the effects of the squeeze film, dry friction and residual viscous damping.

The squeeze film damper coefficient also follows from equating the energy dissipated by the system damping coefficient (C_D) and the combination of viscous damping and dry friction damping,

$$C_D \int V^2 dt = W_v + W_{dry} + W_{rv} \tag{30}$$

where

$$W_{dry} = F_\mu \int |V| dt\,, \quad W_v = C_{SFD} \int V^2 dt\,, \quad W_{rv} = C_{rv} \int V^2 dt \tag{31}$$

VI.2.2 Test results: Dynamic force coefficients for lubricated system

This section presents the SFD added mass and damping force coefficients identified from the circular centered orbit tests with lubricant flowing through the damper. The added inertia term (D_D) is extracted from the dynamic stiffness for the largest amplitude of motion tested (50 μm), provided that the mass of the housing (M) and the mass of the fluid enclosed in the damper (M_f) are available.

The short length, open ends bearing formula for viscous damping coefficient is [2]

$$C_{tt} = \frac{\mu \pi D}{2\left(1-\left(\frac{e}{c}\right)^2\right)^{\frac{3}{2}}}\left(\frac{L}{c}\right)^3 \tag{32}$$

This formula considers a full film and is derived for circular center orbit (CCO) motion, with *e* as the circular orbit radius [2].

Table 8 presents the identified inertia coefficient from the circular orbit tests, and the structural parameters previously identified. The predicted inertia coefficient agrees well with the identified inertia coefficient (~ 9 %). Furthermore, the identified inertia coefficient is considerably larger (~20 %) than that identified from unidirectional tests. This discrepancy is attributed to the effects of the oil entrapped in the recirculation annulus. For these tests, the predicted added mass term is obtained using formulae described in an internal communication document [18], and which includes the effects of the recirculation annulus. This development will be released in the near future.

Table 8 Inertia coefficient identified from unidirectional periodic load tests (amplitude of motion: 38 μm, Frequency range 20-60 Hz)

Parameter	
Stiffness coefficient, (K_s)[kN/m]	805
Total Mass, (M_t) [kg]	21.04
Fluid Mass, (M_f) [kg]	0.62
Housing Mass, (M) [kg]	9.7
Added mass coefficient, (D) [kg]	10.7
R^2	0.98
Predicted added mass (D) [kg]	**11.7**

Figure 43 depicts the system dynamic stiffness and the curve fit the rendered the inertia coefficient. The stiffness (K_s) represents an average of the stiffness identified from structural tests.

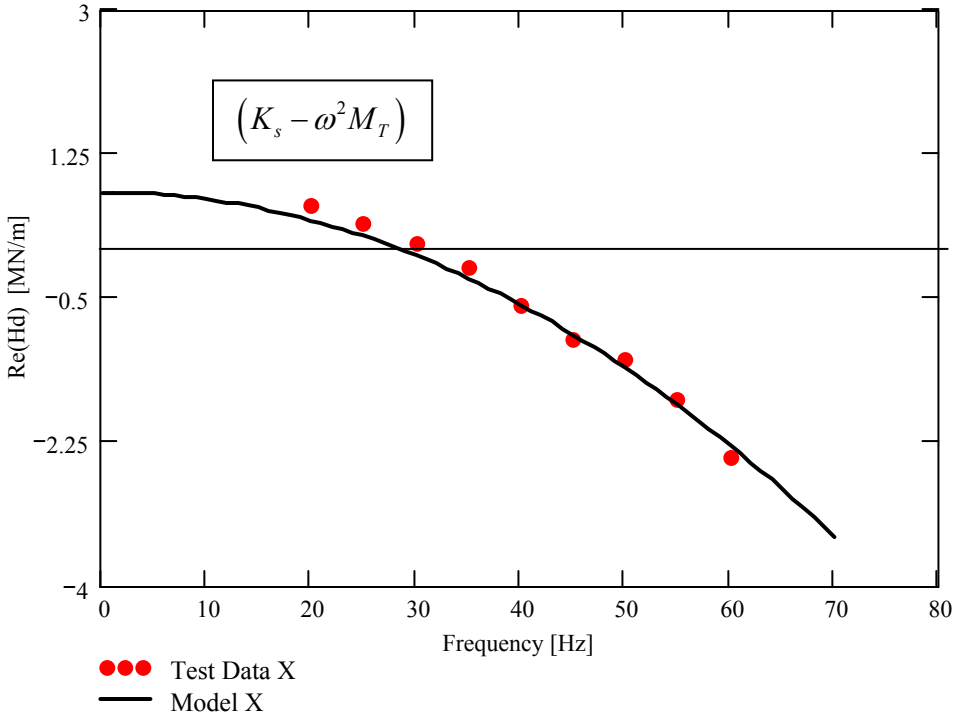

Figure 43 Dynamic stiffnesses from periodic unidirectional excitation tests and analytical model (*D*: 50 μm, K_s= 805 kN/m, M_t= 21 kg. CCO, lubricated SFD)

Figure 44 depicts the damping coefficient identified for the four orbit amplitudes tested (12 μm, 25 μm, 38 μm, 50 μm). The damping coefficients, which include the viscous and dry friction contribution, present a similar trend to those obtained form the unidirectional load tests. The damping coefficient decays steadily with frequency. Furthermore, for the smallest amplitude tests (12 μm) the coefficient is significantly larger than those identified for larger amplitudes. This evidences the large influence of dry friction arising from the mechanical seal. Importantly enough, the dependency of the damping coefficient upon the amplitude of motion is less predominant as the amplitude of motion increases. This is particularly common for systems with dry friction, which generally present threshold amplitudes that determine the different regimes of motion (i.e. slip, macro-slip)

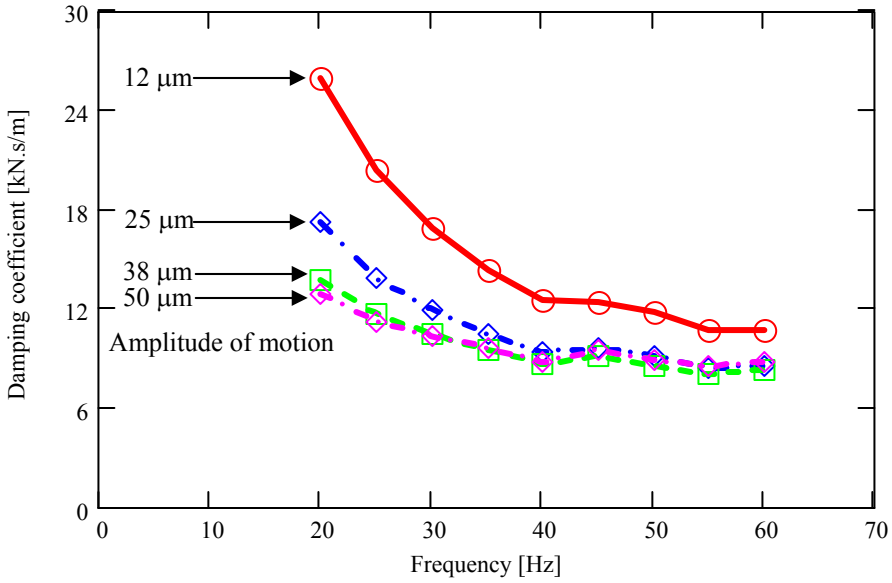

Figure 44 Identified system direct damping coefficient (C_D) versus excitation frequency for increasing orbit radii. (Circular Centered Orbit, lubricated SFD)

Figure 45 presents the squeeze film coefficients (C_{SFD}) extracted from the system total damping coefficient (C_D). The SFD coefficient represents the squeeze film viscous damping contribution to the system overall damping. Unlike the total direct damping coefficient, the squeeze film damping coefficient shows a weak dependency on frequency, which further confirms the significant contribution of the dry friction interaction to the system overall damping coefficient. The damping coefficients decreases near 40 Hz, which coincides with the natural frequency of the test rig main frame. Thus, the change of the damper coefficient between 40 Hz and 50 Hz may be associated to a change (increase) of the normal force at the seal interface due to a larger absolute motion of the main frame.

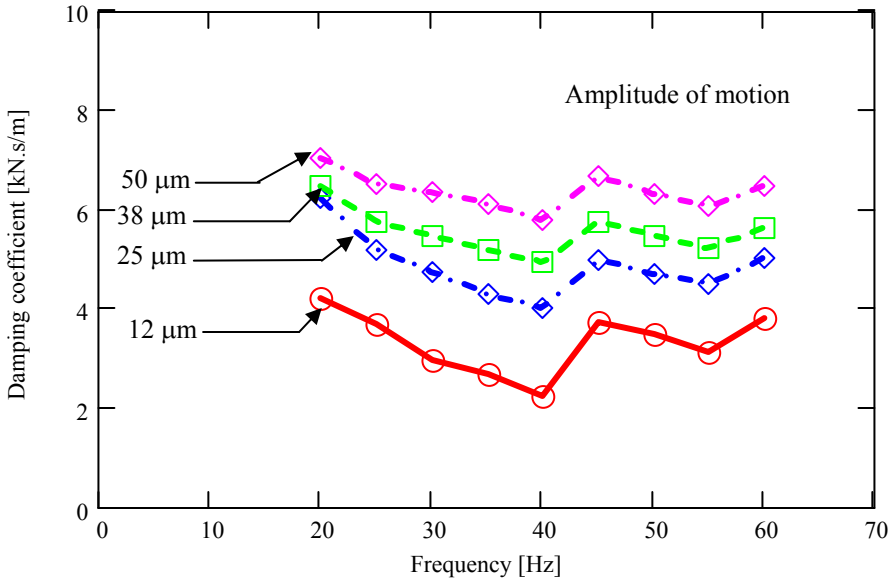

Figure 45 SFD damping coefficients (C_{SFD}) versus excitation frequency for increasing orbit radii. (Circular Centered Orbit, lubricated SFD)

Figure 46 depicts the system damping coefficient (C_D) as a function of the amplitude of motion. The dependency of the coefficient upon the displacement amplitude is more pronounced at low frequencies. Furthermore, the damping coefficient for the smaller test amplitudes (12 µm) is larger than the damping recorded at any other amplitude level for all the frequencies tested. Once more, these trends are consistent with the effect of dry friction in the system.

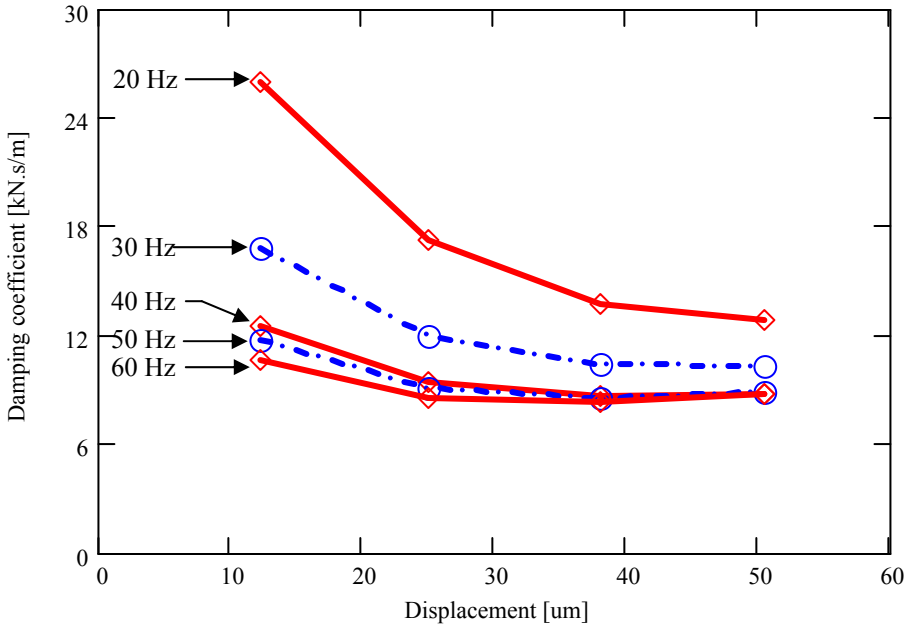

Figure 46 Identified system damping coefficients (C_D) versus orbit radius for increasing frequencies. (Excitation frequency: 20 Hz, 30 Hz, 40 Hz, 50 Hz and 60 Hz. Circular Centered Orbit (CCO), lubricated SFD)

Figure 47 illustrates the squeeze film damping coefficients (C_{SFD}) and predictions as function of the amplitude of motion for two excitation frequencies (20 Hz and 60 Hz). The viscous damping, as oppose to the combined total damping (C_D), increases steadily with the amplitude of motion. The predictions, using Eq. (32), render good agreement for 60 Hz excitations. Though, the predictions slightly underestimate (~18 %) the experimental value for excitations at 20 Hz. This probably indicates that the dry friction damping is being underestimated at low frequencies, thus the estimated C_{SFD} magnitude is larger than the actual value.

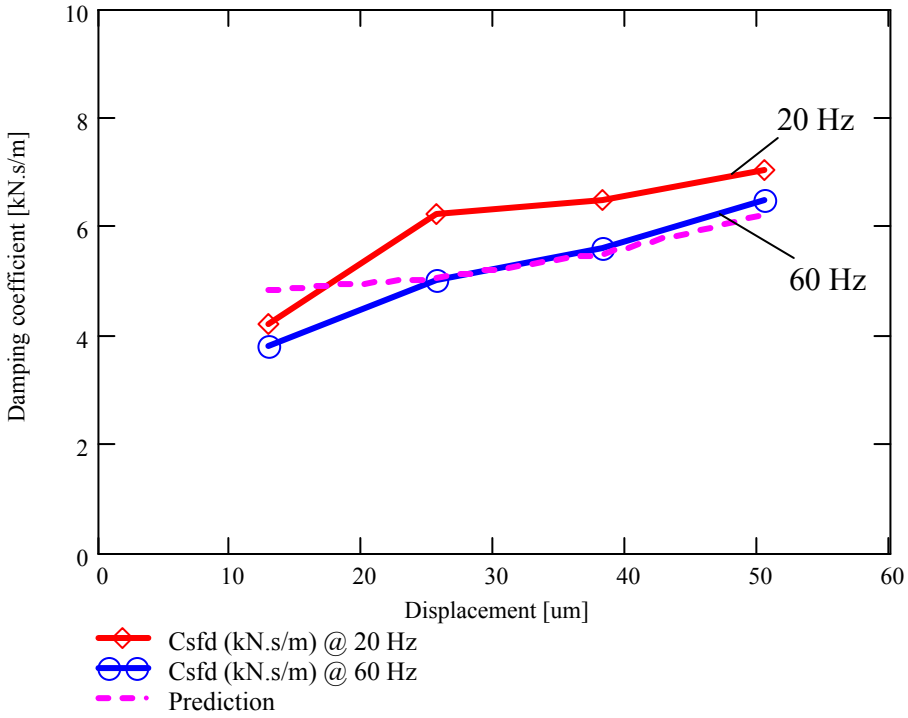

Figure 47 Squeeze film damping coefficient (C_{SFD}) versus displacement amplitude. (Excitation frequency: 20 Hz and 60 Hz. CCO, lubricated SFD)

VII CONCLUSIONS AND RECOMMENDATIONS

Exhaustive experiments were conducted to characterize the mechanical parameters of a SFD installed with an end mechanical seal. The damper can operate as an open end, partially sealed or fully sealed end configuration. The SFD is currently being used in industry, yet no experimental work has been conducted to test the effectiveness of this design.

The test SFD structure stiffnesses are derived from static load tests without the seal in place. Periodic loads, single frequency, acting on the dry test system (no lubricant) aid to identify the dry friction force (26 N-31 N) at the mechanical seal contact surface via mechanical energy balance method. The damping action of the dry friction coefficient is included in the system equations of motion as an equivalent viscous damping coefficient.

Experimental test system damping and added mass coefficients follow from unidirectional and circular dynamic load excitations in the frequency range from 20 to 60 Hz. In the experiments, the load magnitudes vary to maintain prescribed amplitudes of motion. The parameter identification is carried in the frequency domain by building system transfer functions from the measured load and displacements. The test system damping combines the effects of dry-friction in the contact zone of the mechanical seal, the squeeze film lands, and a residual action from the structural supports. The squeeze film damping coefficient is effectively extracted from the test system damping by equating the work (exerted by the external load) to the energy dissipated by each type of damping, provided that the dry friction force is previously identified.

The identification results show that the system damping coefficients are larger at the lowest frequency and lowest amplitude of motion, denoting the paramount effect of dry friction in the mechanical seal. The estimated damping coefficients for the squeeze film land alone are nearly independent of frequency, increasing slightly with the amplitude of dynamic motion. Theoretical predictions, based on the short length bearing model, agree well with the experimental results.

The experimental results demonstrate the end seal effectively prevents air entrapment into the squeeze film land for the frequencies and amplitudes of motion tested. Further experimentation is planned to identify damping coefficients for elliptical motions, centered and off-centered. Future tests aim to vary the seal contact force and to replace the orifice discharge ports in order to simulate continued operation, wear and aging under extend periods of work, for example.

Future work will also include test with higher frequency ranges and a scrutiny of the dynamic pressures at the recirculation annulus and squeeze film land. These experimental results will also provide benchmarks to validate analytical developments focused on improving predictions of inertia force coefficients (added mass terms) in squeeze film dampers.

REFERENCES

[1] Rodriguez, L., Diaz, S., and San Andrés, L., 2000, "Sine Sweep Load Versus Impact Excitations and Their Influence on the Identification of Damping in a Bubbly Oil Squeeze Film Damper," TRC Report, TRC-SFD-3-00.

[2] Zeidan, F.Y., San Andrés, L., and Vance, J. M., 1996, "Design and Application of Squeeze Film Dampers in Rotating Machinery," *Proceedings of the 25th Turbomachinery Symposium*, Houston, TX, pp.169-188.

[3] Diaz, S., and San Andrés, L., 2000,"Orbit-Based Identification of Damping Coefficients of Off-centered Squeeze Film Damper Including Support Flexibility," ASME Paper 2000-GT-0394.

[4] San Andrés, L., and Diaz, S., 2002, "Flow Visualization and Forces from a Squeeze Film Damper with Natural Air Entrapment," ASME Journal of Tribology, **125**(2), pp. 325-333

[5] Diaz, S., and San Andrés, L., 1999, "Reduction of the Dynamic Load Capacity in a Squeeze Film Damper Operating with a Bubbly Lubricant," ASME Journal of Gas Turbines and Power, **121,** pp. 703-709.

[6] Pietra, D., and Adiletta, G., 2002,"The Squeeze Film Damper over Four Decades of Investigations. Part I: Characteristics and Operating Features," The Shock and Vibration Digest, **34**(1), pp. 3-26.

[7] Pietra, D., and Adiletta, G., 2002,"The Squeeze Film Damper over Four Decades of Investigations. Part II: Rotordynamic Analyses with Rigid and Flexible Rotors," The Shock and Vibration Digest, **34**(2), pp. 97-126.

[8] San Andrés, L., and Vance, J., 1986, "Experimental Measurements of the Dynamic Pressure Distribution in a Squeeze-Film Bearing Damper Executing Circular-Centered Orbit," ASLE Transactions, **30**(3), pp. 373-383

[9] Roberts, J. B., Holmes, H., and Mason, T. J., 1986, "Estimation of Squeeze-Film Damping and Inertial Coefficients from Experimental Free-Decay Data," Proc. Instn Mech. Engrs, **200**(C2), pp 123-133

[10] Ellis, J., Roberts, J. B., and Hosseini, S. A., 1990, "The Complete Determination of Squeeze-Film Linear Dynamic Coefficients from Experimental Data," ASME Journal of Tribology, **112**, pp. 712-724

[11] Miller, R., Arauz, G., San Andres, L., 1995, "A Test Rig for the Identification of Rotordynamic Coefficients of Fluid Film Bearings Elements," *Proceedings of the International Gas Turbine and Aeroengine Congress and Exposition*, June, Houston, TX, pp.1-9.

[12] Levesley, M., and Holmes, R., 1996, "The Effect of Oil Supply and Sealing Arrangements on the Performance of Squeeze-Film Dampers: an Experimental Study," Journal of Engineering Tribology, **210**, pp. 221-232.

[13] Arauz, G., L., San Andrés, L.,1997," Experimental Force Response of a Grooved Squeeze Film Damper," Tribology International, **30**, Jan, 77-86

[14] De Santiago, O., and L. San Andrés,1999, "Imbalance Response and Damping Force Coefficients of a Rotor Supported on End Sealed Integral Squeeze Film Dampers," ASME Paper 99-GT-203

[15] Diaz, S., and San Andrés, L., 1999, "A Method for Identification of Bearing Force Coefficients and Its Application to a Squeeze Film Damper with a Bubbly Lubricant," STLE Tribology Transactions, **42** (4), pp. 739-746.

[16] San Andrés, L., and De Santiago, O., 2004, "Forced Response of a Squeeze Film Damper and Identification of Force Coefficients from Large Orbital Motions," ASME Journal of Tribology, **126**(2), pp. 292-300

[17] Kim, K., and Lee, C.,2005, "Dynamic Characteristics of Sealed Squeeze Film Damper with a Central Feeding Groove," Journal of Tribology, **127**(1), pp. 103-111

[18] Delgado, A., and San Andrés, L., 2004, "Sealed End Squeeze Film Damper: Test Rig Description and Identification of Structural Parameters," TRC Report, TRC-SFD-1-04, May.

[19] Diaz, S., 2000, " CCO Data adquisition," LabView® virtual instrument. Tribology Group, Texas A&M Turbomachinery Laboratory.

[20] Ginsberg, J. H., 2001, *Mechanical and Structural Vibrations*, John Wiley & Sons*, Inc*., New York, pp. 135-139

[21] Pinkus, O., and Sternlight, B., 1961, *Theory of Hydrodynamic Lubrication,* McGraw-Hill Book Company Inc. , New York. pp. 34-35

[22] Delgado, A., San Andrés, 2005, "Identification of Structural Stiffness and Damping Coefficients of a Shoed Brush Seal," ASME Paper DETC 2005-84159, ASME IDETC/CIE Conference, Long Beach, CA.

[23] San Andrés, L., 2005, " Fluid Inertia Effects," Internal communication, Tribology Group, Texas A&M Turbomachinery Laboratory.

[24] Coleman, H. W., and Steele, G. W., 1988, *Experimentation and Uncertainty Analysis for Engineers,* John Wiley & Sons, New York.

APPENDIX A

CALIBRATION OF EDDY CURRENT SENSORS

This section describes the results and procedure followed for calibrating the eddy current sensors employed in the identification of the test rig structural parameters.

The calibration of the eddy current sensors was performed in situ (i.e. eddy current sensors attached to the rig). Two dial gauge (± 0.0001) with magnetic bases, located in the *X* and *Y* direction, made it possible to measure the actual displacement of the bearing housing. An ad-hoc device attached to the lower base of the test rig (as shown in Figure A 1) served to induce a steady displacement of the SFD housing. The calibration includes deflections in both directions of *X* and *Y*. Table A1 presents the gain of the eddy current sensors estimated from a linear regression of the calibration results shown in Figure A 2.

Table A1 Eddy current sensors gain estimated from calibration tests.

	X_1	X_2	Y_1	Y_2
Gain[mV/mils]	202	195	204	N/A
R^2	0.99	0.99	0.99	N/A
Serial #	H-108912	H-108877	H-108913	H-108914

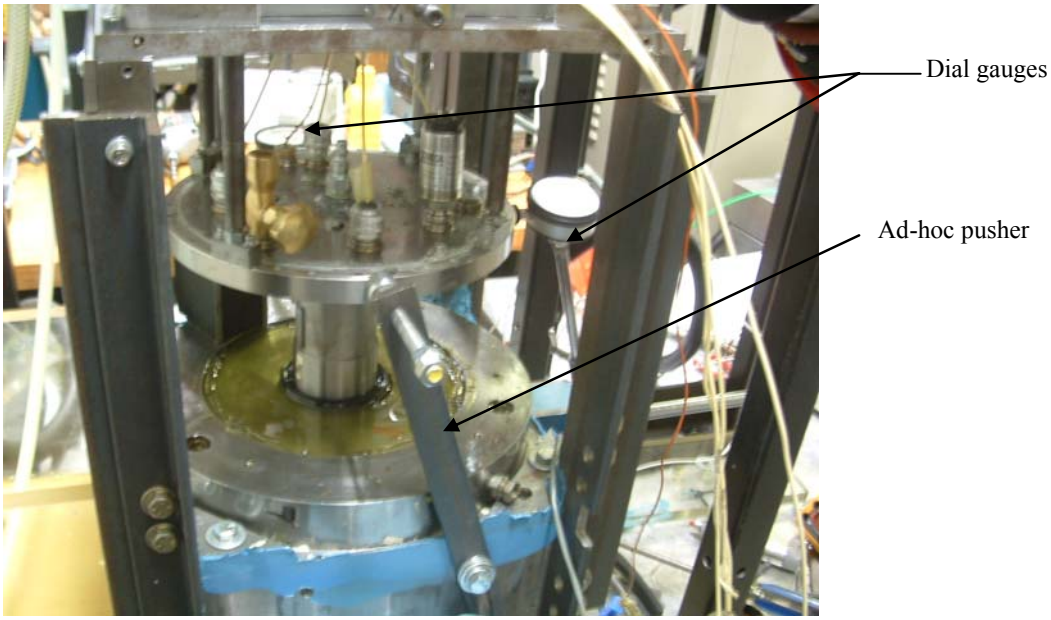

Figure A 1 Picture of VTR set up for calibrating eddy current sensors

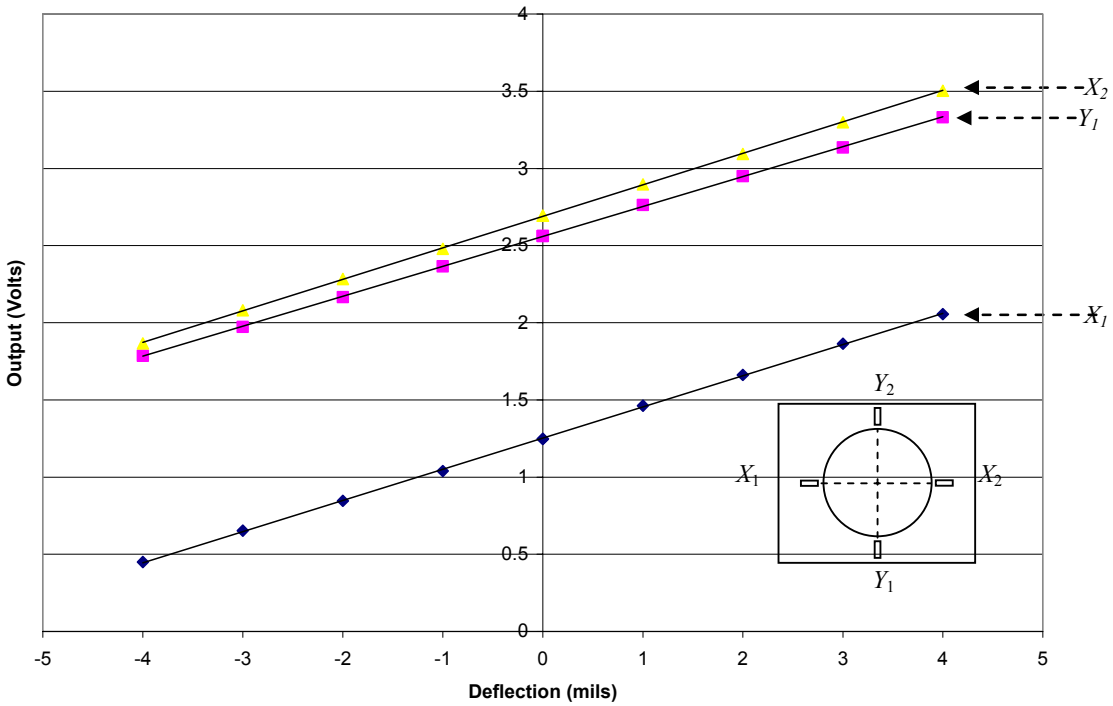

Figure A 2 Voltage output of eddy current sensors vs. displacement of SFD bearing. (Calibration test)

APPENDIX B

UNCERTAINTY ANALYSIS OF TEST DATA

This section is dedicated to asses the uncertainty associated with the results reported in previous sections. The analysis contemplates the estimation of the error of each individual measurement, as well as the error propagation associated with parameters that are function of other variables.

B.1 Eddy current sensor calibration

The calibration of the proximity sensor (Appendix A) included readings from a displacement gauge ($U_d = \pm 0.0001$") and a voltmeter ($U_v = \pm\ 0.001\ V$). The uncertainty at each point is normally given by the precision and bias error of each instrument. However, for this calibration process, the uncertainty of each point (U_d, U_v) does not include the bias error of each instrument. Recall that the bias error is the fixed, systematic, or constant component of total error [24]. Thus, the calculation of the proximity sensor gains is not affected by the bias error, considering that the calculation of such gain is based on the relative value between each measurement (i.e. slope). On the other hand, the standard error of an estimate (*SEE*) can be used to obtain the goodness of the (least-squares) line that best fits the collection of pairs (voltage, displacement). That is, the *SEE*, given in equation (B.1) below, represents the deviation of the curve fit ($y=ax+b$) from the data set. The term "*N-2*" in the denominator arises from the two degrees of freedom lost from the set of N data pairs (X_i, Y_i) when determining the curve constants, a and b (slope and axis intersection) [24].

$$SEE = \left(\frac{\sum_{i=1}^{N} [Y_i - (aXi + b)]^2}{N - 2} \right)^{1/2} \qquad \text{(B.1)}$$

The proximity sensor gain, given by the slope (a) of the curve fit, also follows the relationship

$$G = \frac{\Delta D}{\Delta V_{fit}} \tag{B.2}$$

with ΔD as the displacement variation and ΔV_{fit} as the voltage variation given by the linear fit.

The general equation used for calculating the uncertainty of parameters that are calculated from direct relations (i.e. $r=f(x_1,x_2,..x_n)$) is defined as [24]

$$U_r = \sqrt{\left(\frac{\partial r}{\partial x_1}U_{x_1}\right)^2 + \left(\frac{\partial r}{\partial x_2}U_{x_2}\right)^2 + ... + \left(\frac{\partial r}{\partial x_n}U_{x_n}\right)^2} \tag{B.3}$$

Then, from Equation B.3 the uncertainty of expression B.2 is

$$\left(\frac{U_G}{G}\right)^2 = \left(\frac{\partial G}{\partial D}\frac{U_D}{G}\right)^2 + \left(\frac{\partial G}{\partial V_{fit}}\frac{U_{V_{fit}}}{G}\right)^2 = \left(\frac{1}{\Delta D}U_D\right)^2 + \left(\frac{1}{\Delta V_{fit}}U_{V_{fit}}\right)^2 \tag{B.4}$$

where ΔD and ΔV_{fit} are given by the range of experimental values and $U_{V_{fit}}$ is calculated combining the voltmeter uncertainty (U_v) and the uncertainty of the curve fit given by the B.1 as

$$U_{V_{fit}} = \sqrt{\left(U_{fit}\right)^2 + \left(U_V\right)^2} \tag{B.5}$$

B.2 Parameter identification

B.2.1 Static tests

The procedure to estimate uncertainty of the stiffness resulting from static test is similar to the one followed in the calibration of the proximity sensor. In this case, since each data pair (displacement, force) is the average from three different tests, the uncertainty of each point (in the displacement axis) of the force vs. displacement data collection is given by the combination of the instrument uncertainty (i.e. voltmeter) and the error incurred from averaging the three test, which is given by

$$U_{avg} = tS_{\bar{x}} \quad t=4.303, \qquad S_{\bar{x}} = S_x/\sqrt{N} \qquad ; \; S_x = \left[\frac{1}{N-1}\sum_{i=0}^{N}\left(X_i - \bar{X}\right)^2\right]^{1/2} \tag{B.6}$$

where $S_{\bar{x}}$ is the precision index of the mean value, S_x is the precision index; and, $\bar{X}$ and X_i represent the mean of the sample array and the individual samples, respectively. And t is the coefficient for 2 degrees of freedom (N-1) and a 95% confidence interval for a t-distribution of data points [24].

Subsequently, the uncertainty of the linear fit is given by B.1 and the uncertainty associated with the slope (stiffness coefficient) is defined as

$$\left(\frac{U_K}{K}\right)^2 = \left(\frac{1}{\Delta F}U_F\right)^2 + \left(\frac{1}{\Delta D_{fit}}U_{D_{fit}}\right)^2 + \left(\frac{1}{G}U_G\right)^2 \tag{B.7}$$

where

$$K = \frac{G}{V}F \tag{B.8}$$

B.2.2 Impact tests

For this case the uncertainty in the stiffness and mass coefficients is given by the uncertainty associated with the measurements of displacement and force (i.e. instrumentation uncertainty) and the error from the transfer function fit.

$$H(\omega) = \frac{1}{\left[\left(K^2 - M\omega^2\right)^2 + (C\omega)^2\right]^{1/2}} \tag{B.9}$$

This assumption is valid for stiffness and mass coefficient only, regarding that the curve fit matches the measured flexibility (i.e. displacement/ force) at $\omega \rightarrow 0$ (±4%), and that the stiffness and the mass given by the numerical fit follow from the expressions

$$H_{fit}(0) = \frac{1}{K}, \quad M = \frac{K}{\omega_n{}^2} \tag{B.10}$$

where the uncertainty of the natural frequency ω_n is given by the window resolution used in the dynamic frequency analyzer (400 Hz/400 lines= ± 1Hz resolution).

Therefore, the uncertainties of the stiffness and mass are

$$\frac{U_K}{K} = \frac{U_{H_{fit}}}{H(0)}, \quad \left(\frac{U_M}{M}\right)^2 = \left(\frac{U_K}{K}\right)^2 + \left(\frac{2U_K}{\omega_n}\right)^2 \tag{B.11}$$

where

$$\left(\frac{U_{H_{fit}}}{H_{fit}}\right)^2 = \left(\frac{U_F}{F}\right)^2 + \left(\frac{U_D}{D}\right)^2 + \left(1 - \frac{H}{H_{fit}}\right)^2$$

and

$\left(\frac{U_F}{F}\right) = 0.01$ (1% linearity), $\left(\frac{U_D}{D}\right)^2 = \left(\frac{0.0008}{.03019}\right) = 7.84x10^{-4}$

B.3 Flow measurements

The flow meter is rated for flows of .3 to 3 GPM, and is field calibrated to ensure greater accuracy. The calibration procedure requires a container calibrated in one gallon increments from one to five. The container is calibrated by weighing water to estimate its volume as

$$gal._{h_2o} = Mass * \left(\frac{1}{\rho h_2 0}\right) * \left(\frac{1}{Cp}\right) \tag{B.12}$$

where mass as the liquid mass, ρ the density of water at 21 ^{0}C and *Cp* a conversion factor conversion factor (0.13368 ft^3/gal. h20)

The uncertainty of Eq. B.1 is related to the dynamometer used to weight the water and is given by the expression [24]

$$Ucalib. = \left[\left(\frac{\partial gal.}{\partial Mass} * Umass\right)^2\right]^{1/2} \tag{B.13}$$

The uncertainty of the calibration of the container is 0.03 gallons.

Field calibration of the flow meter involves reading the amount of liquid in the container and inputting the data into the flow meter. The level of liquid in the calibration container can be read at an accuracy of 1/16" from the actual gallon mark. The combined error of the calibration is 0.04 Gal. The bias error of the flow meter is given by the manufacturer as %1.5 of the measured value.

Pressure is measured using Omega® PX-215 pressure sensors. The sensors operate on a process current from 4 to 20mA. This current is read by a digital ammeter before entering the Omega® display. The current output of the pressure sensors was calibrated to pressures using an Ashcroft portable gauge tester. The current measured is converted to pressure using equation

$$P = k * ip + C_2 \tag{B.14}$$

where k is the pressure sensor calibration constant, ip the measured current (mA) and C_2 intercept of pressure calibration curve

The equation for the pressure sensor calibration constant is given by

The uncertainties used in this analysis were the uncertainty of the Ashcroft portable tester and the digital ammeters. The uncertainty values for the pressure sensors at the inlet and recirculation annals are calculated at 5 psig. The uncertainty of the calibration (Eq. B.3) is given by [24]

$$Uk = \left[\left(\frac{\partial k}{\partial P} * UP_{calib.} \right)^2 + \left(\frac{\partial k}{\partial ip} * Uip \right)^2 \right]^{1/2} \tag{B.15}$$

Combining the uncertainty of the calibration and the uncertainty of the ammeter reading yields the uncertainty of the pressure measurement

$$Up = \left[\left(\frac{\partial P}{\partial k} * Uk \right)^2 + \left(\frac{\partial P}{\partial ip} * Uip \right)^2 \right]^{1/2} \tag{B.16}$$

The uncertainty of the inlet pressure reading is 0.182 psig. The uncertainty of the pressure readings at the recirculation annulus is 0.177 psig.

For the flow measurements the precision index for each sample is calculated as [24]

$$S_X = \left[\frac{1}{N-1} \sum_{i=1}^{N} \left(X_i - \overline{X} \right)^2 \right]^{1/2} \tag{B.17}$$

and the precision index of the mean is

$$S_{\overline{X}} = S_X / \sqrt{N} \tag{B.18}$$

where N is the number of samples , X is the sample values and $\overline{X}$ is the mean value of the sample population. The t value for %95 confidence with three samples is 4.3. The precision error is [24]

$$P_{\overline{X}} = tS_{\overline{X}} \tag{B.19}$$

The bias error is a combination of the calibration errors and the manufacturer given %1.5 bias error.

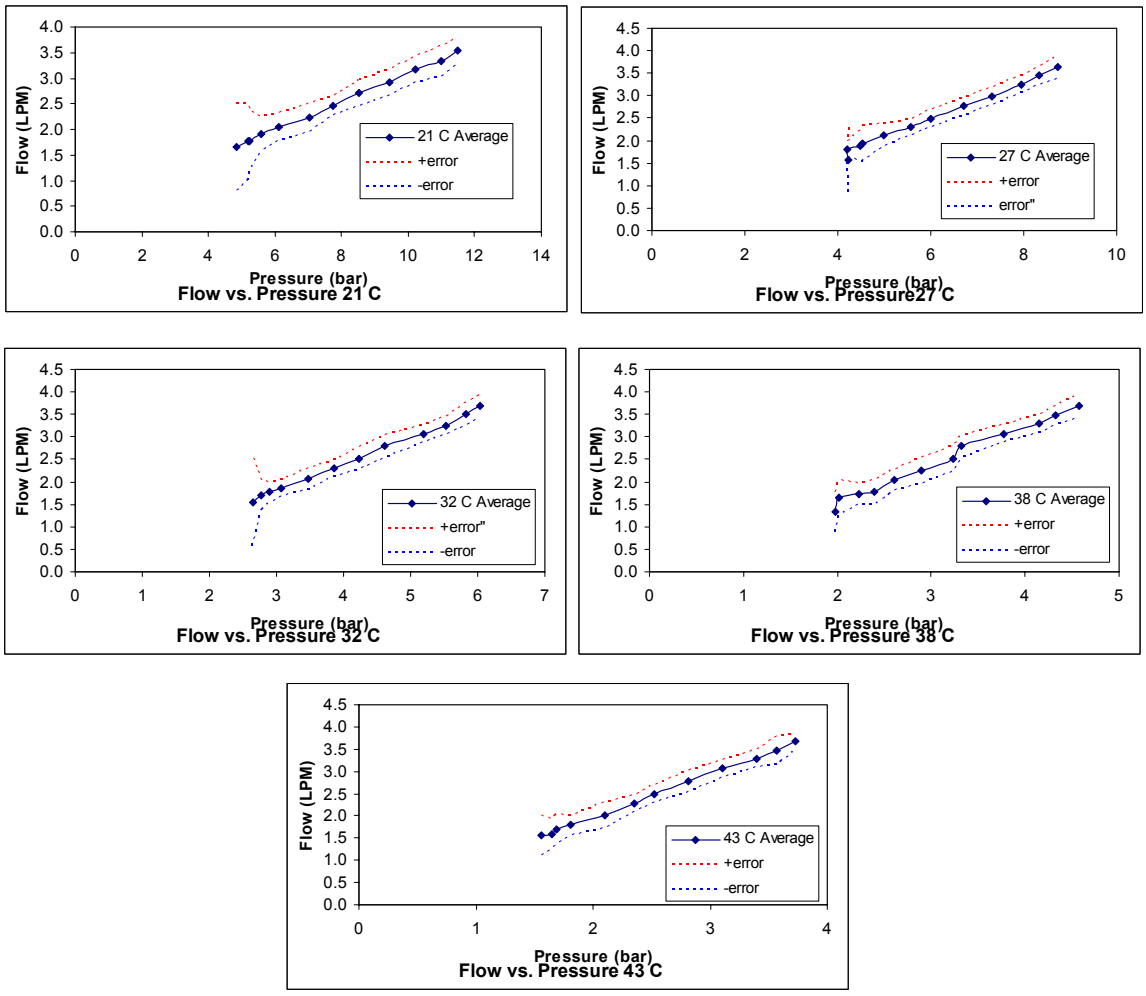

Figure B 1 Lubricant flow through SFD vs. inlet pressure. (Average from three sets of tests)

APPENDIX C

ORBITS AT 30 HZ, 40 HZ, 50 HZ, 90 HZ FROM DYNAMIC TESTS (DRY SYSTEM)

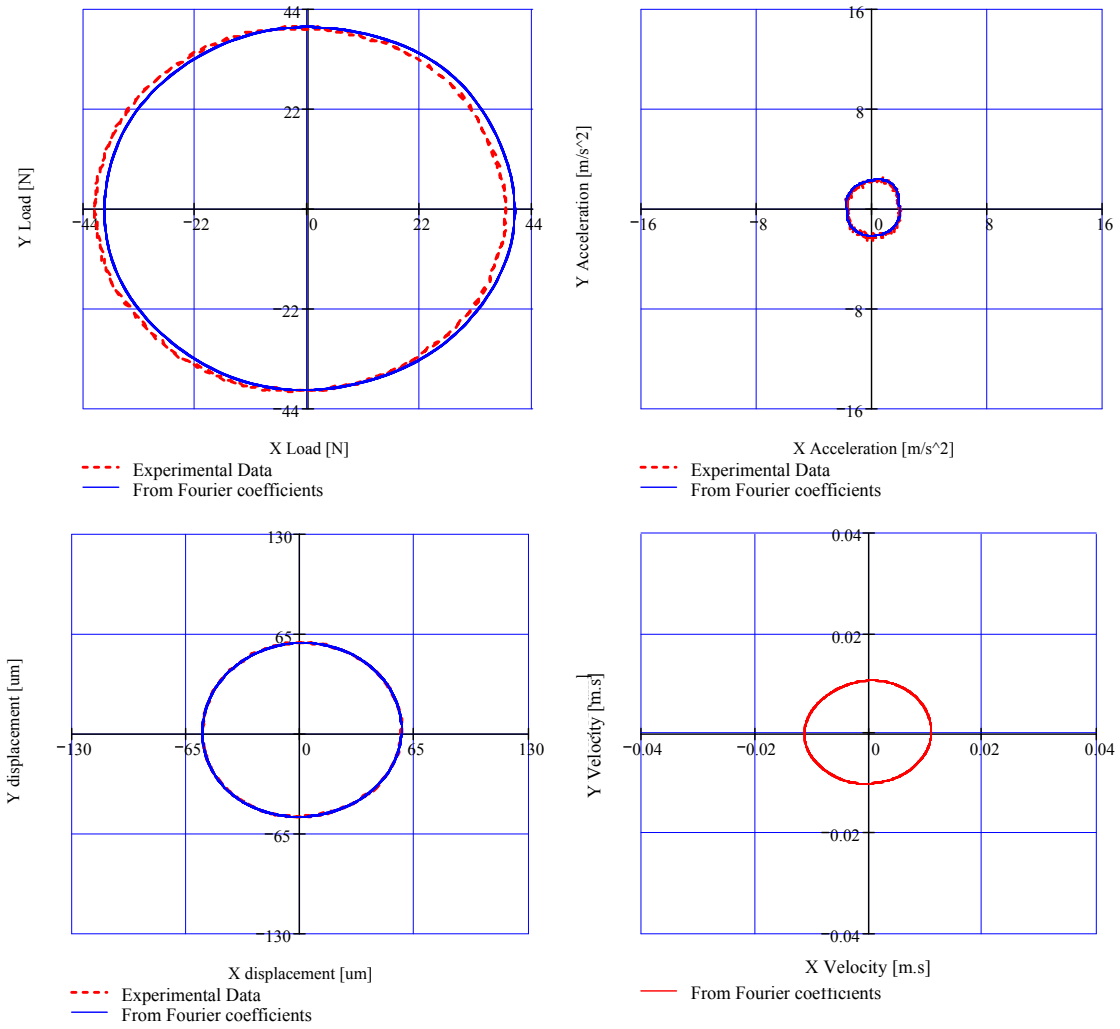

Figure C 1 Excitation and response orbits from experimental data and Fourier coefficients. Velocity orbit built from Fourier coefficients of the displacement response. (40 N, 30 Hz. Dry system)

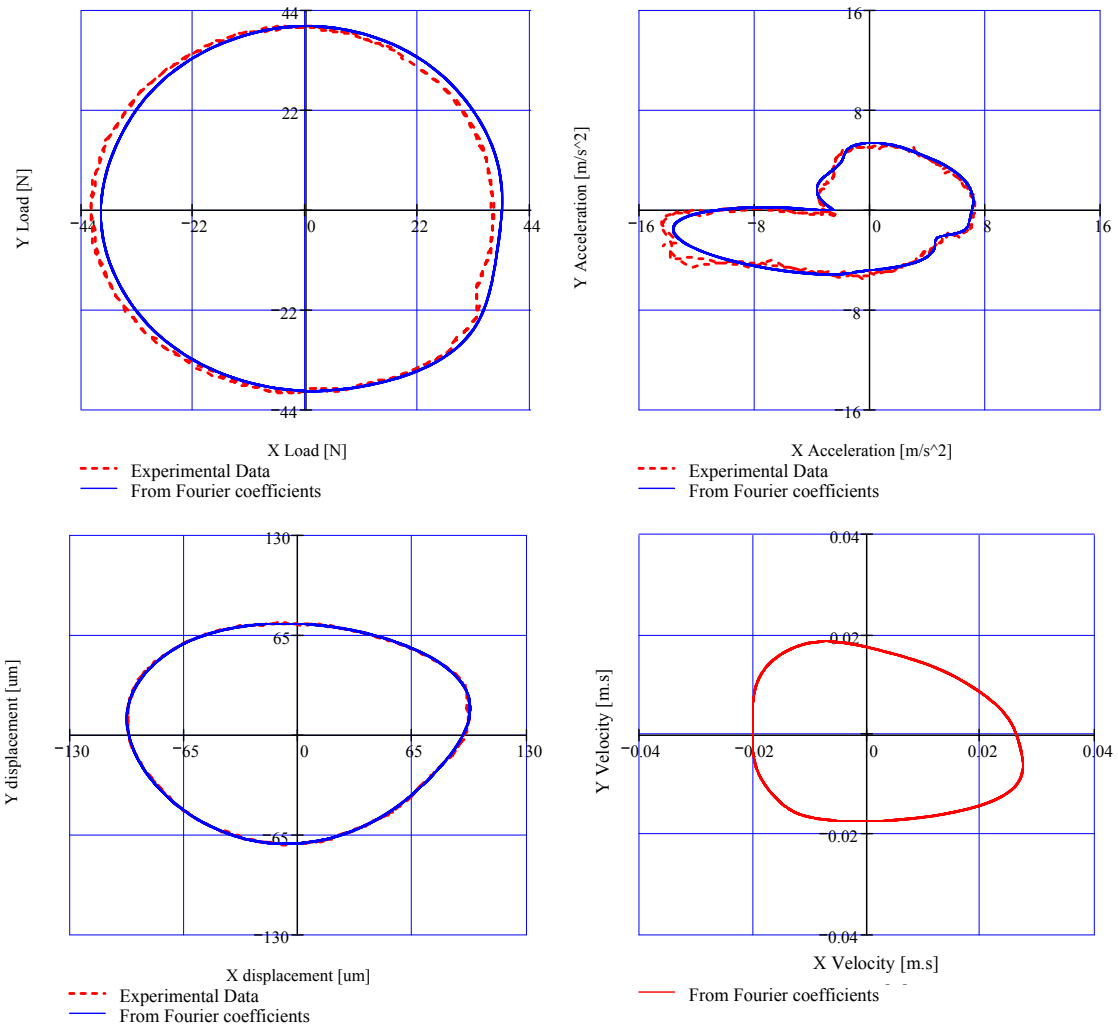

Figure C 2 Excitation and response orbits from experimental data and Fourier coefficients. Velocity orbit built from Fourier coefficients of the displacement response. (40 N, 40 Hz. Dry system)

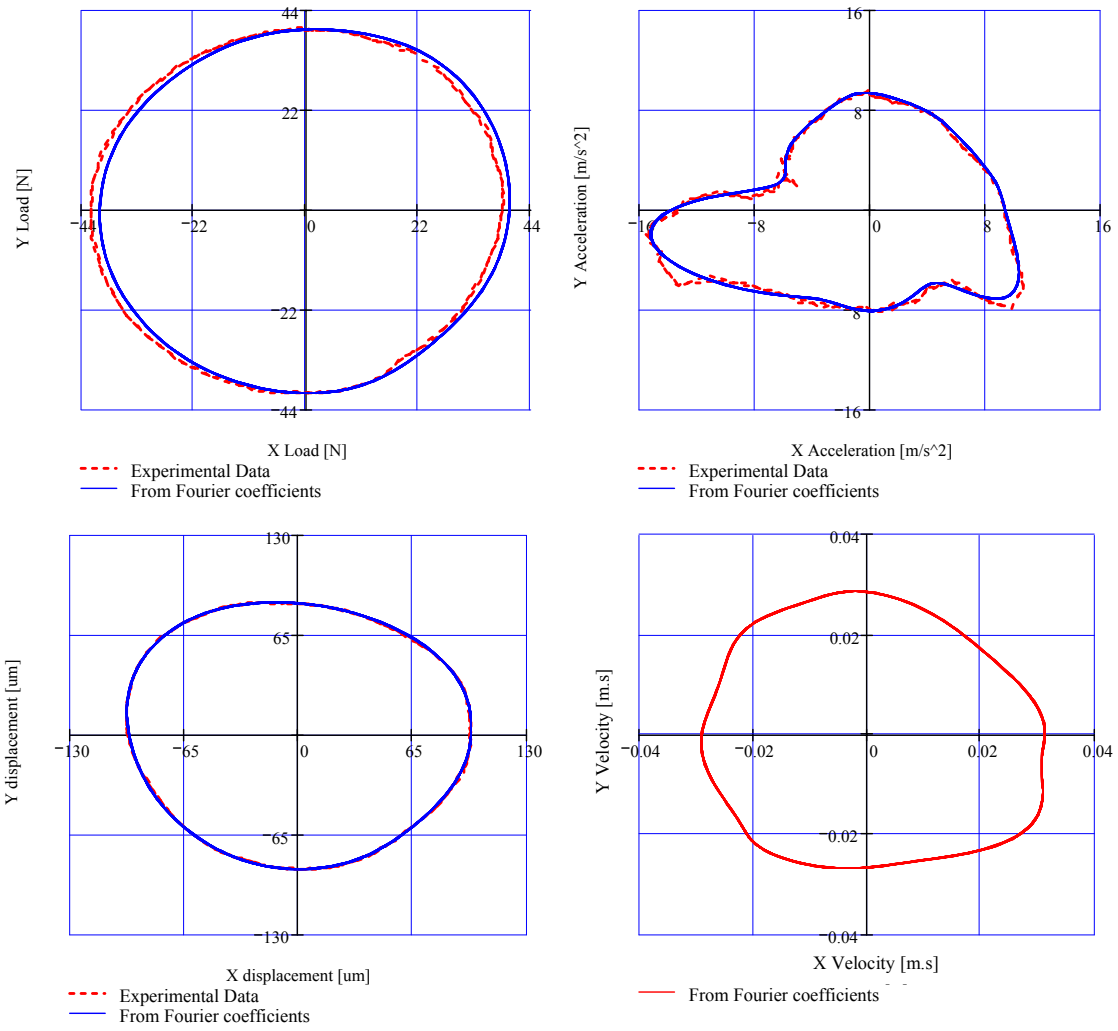

Figure C 3 Excitation and response orbits from experimental data and Fourier coefficients. Velocity orbit built from Fourier coefficients of the displacement response. (40 N, 50 Hz. Dry system)

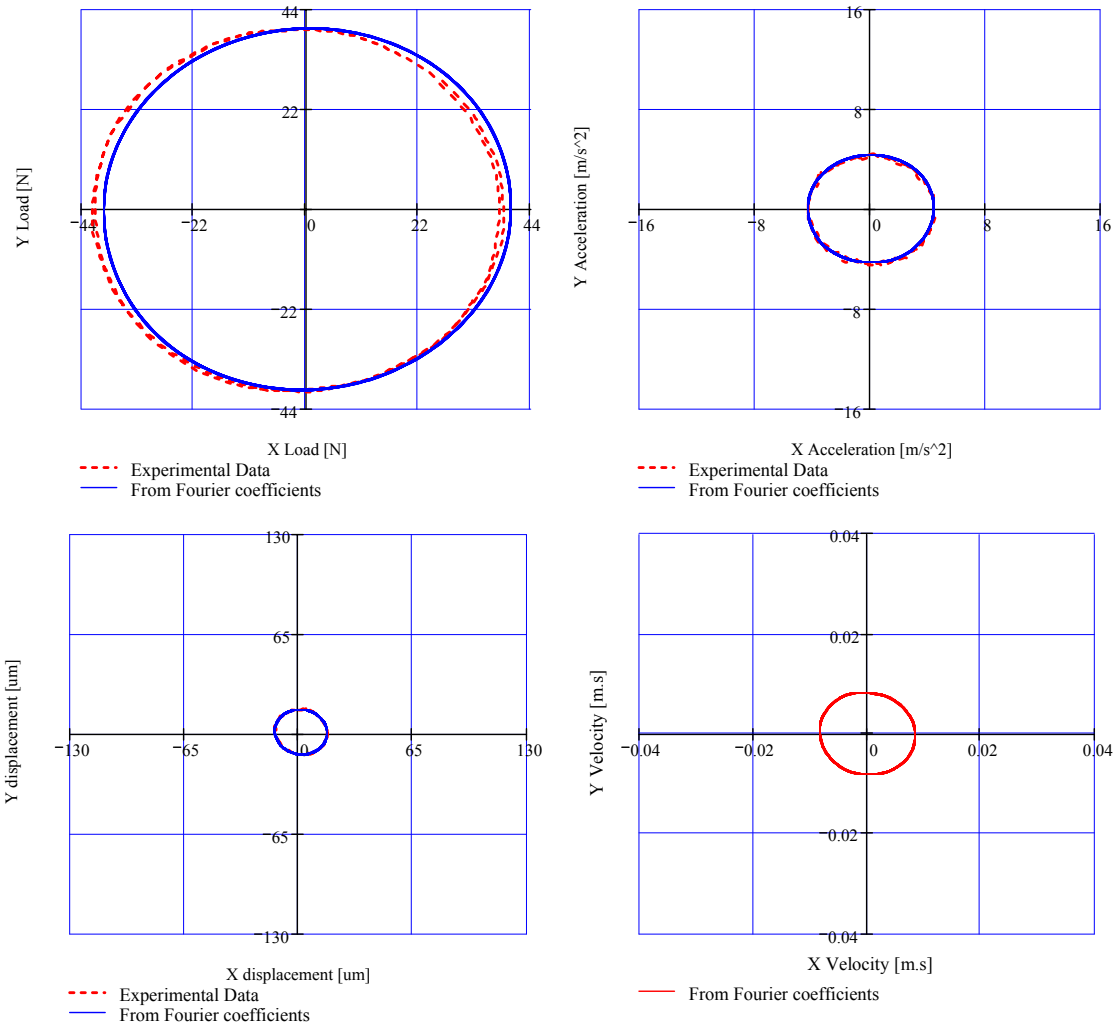

Figure C 4 Excitation and response orbits from experimental data and Fourier coefficients. Velocity orbit built from Fourier coefficients of the displacement response. (40 N, 90 Hz. Dry system)

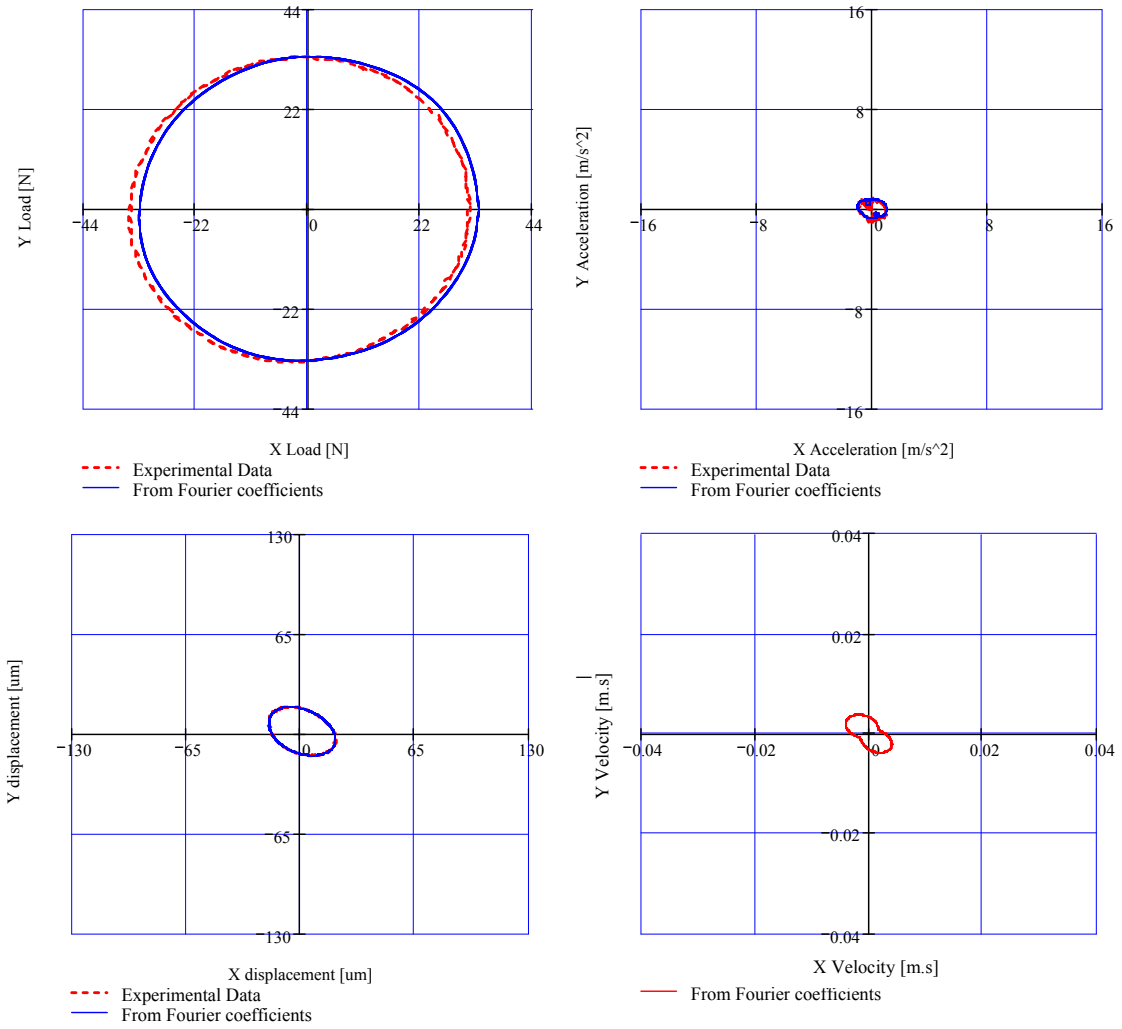

Figure C 5 Excitation and response orbits from experimental data and Fourier coefficients. Velocity orbit built from Fourier coefficients of the displacement response. (33 N, 30 Hz. Dry system)

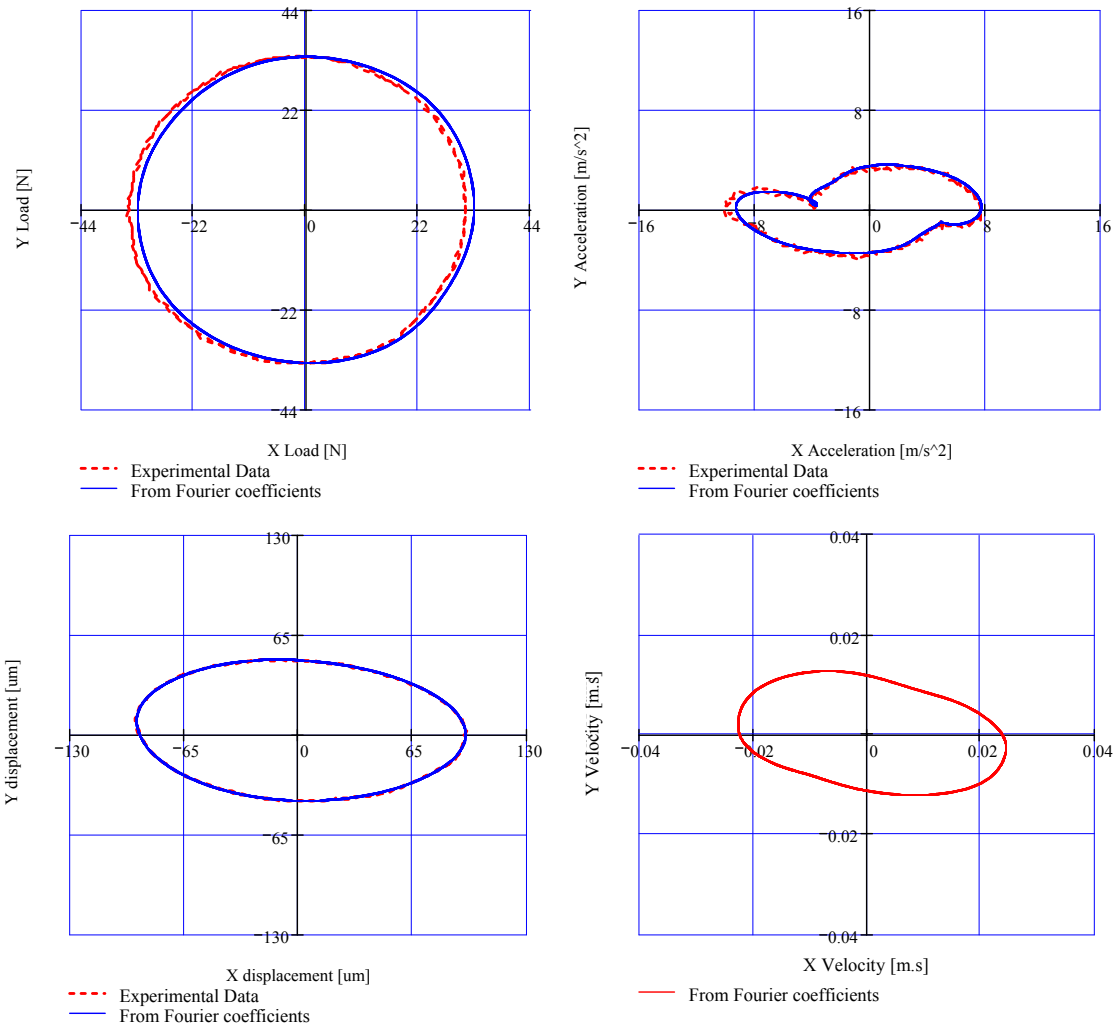

Figure C 6 Excitation and response orbits from experimental data and Fourier coefficients. Velocity orbit built from Fourier coefficients of the displacement response. (33 N, 40 Hz. Dry system)

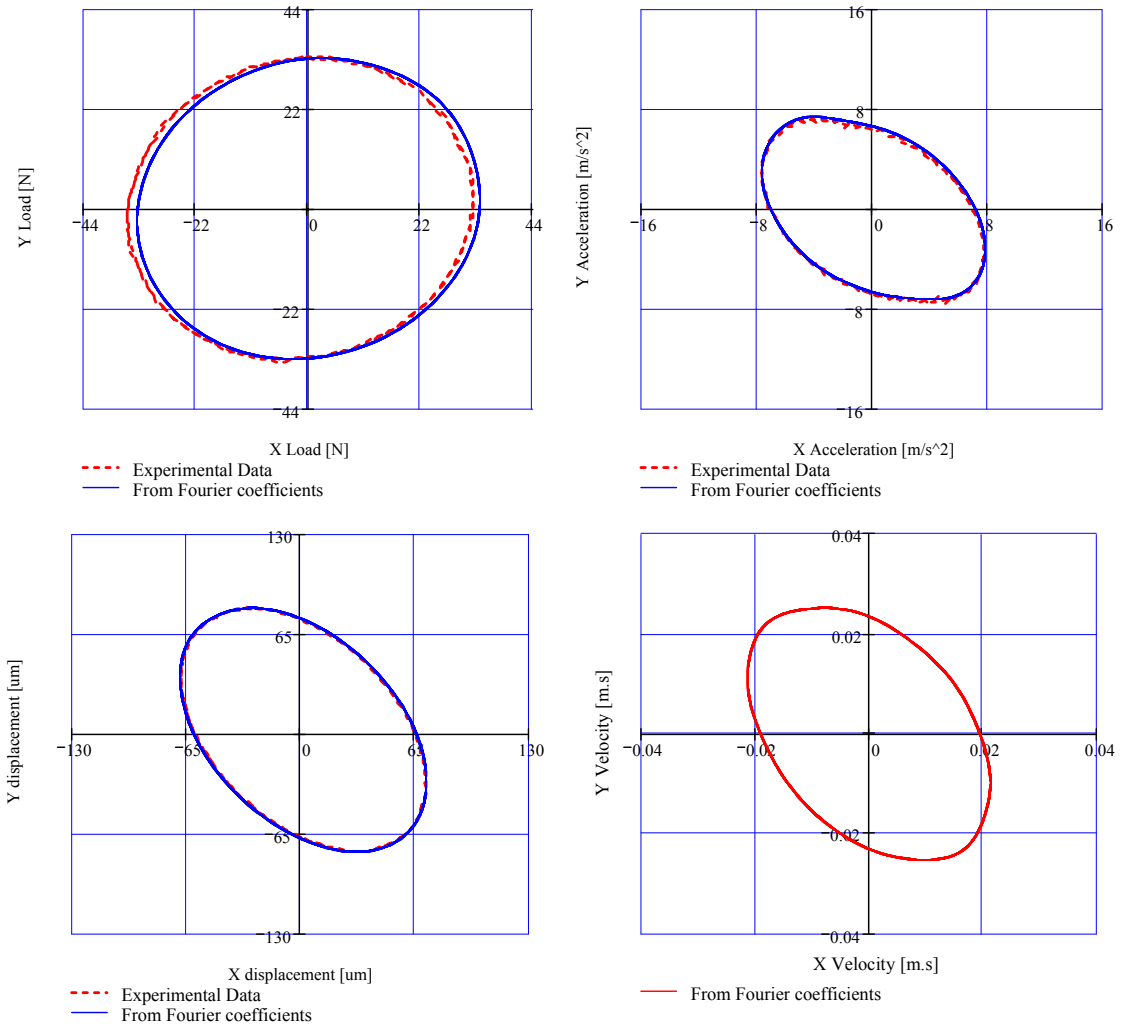

Figure C 7 Excitation and response orbits from experimental data and Fourier coefficients. Velocity orbit built from Fourier coefficients of the displacement response. (33 N, 50 Hz. Dry system)

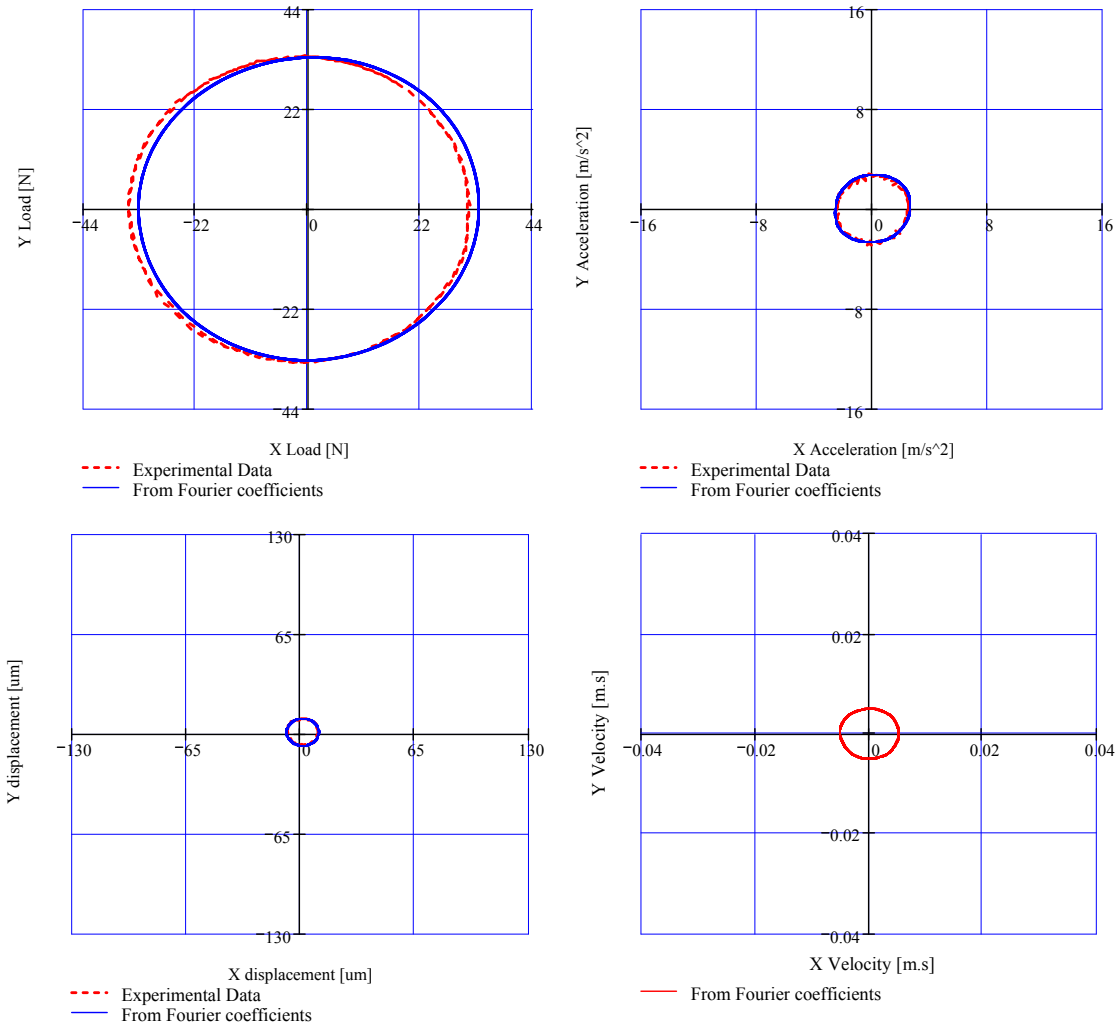

Figure C 8 Excitation and response orbits from experimental data and Fourier coefficients. Velocity orbit built from Fourier coefficients of the displacement response. (33 N, 90 Hz. Dry system)

APPENDIX D

DISPLACEMENT ORBIT FROM UNIDIRECTIONAL DYNAMIC TESTS

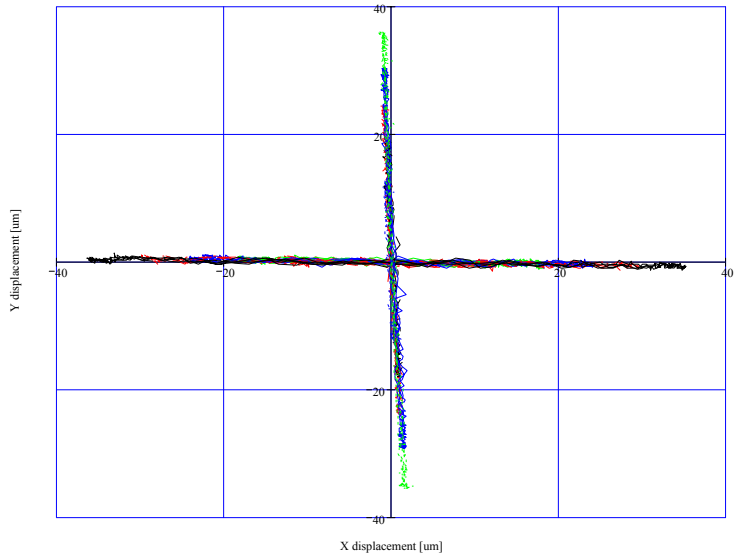

Figure D 1 Linear displacements in *X* and *Y* due to a unidirectional load in *X* and *Y* directions, respectively (20 Hz, lubricated SFD)

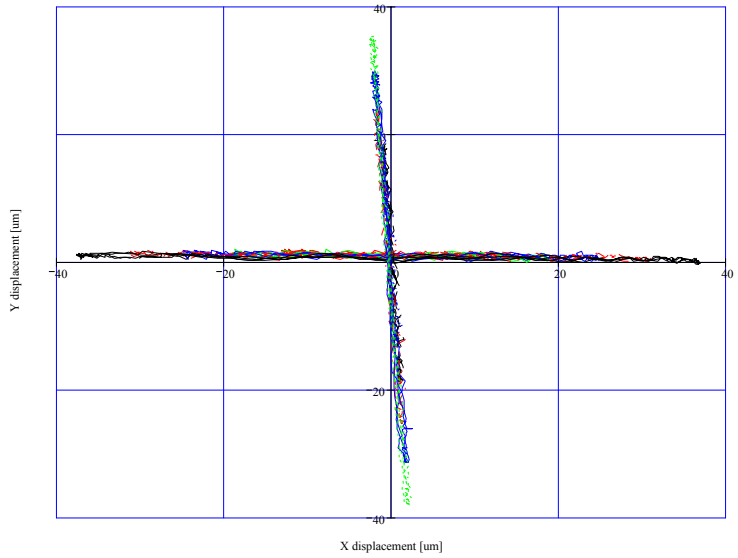

Figure D 2 Linear displacements in *X* and *Y* due to a unidirectional load in *X* and *Y* directions, respectively (30 Hz, lubricated SFD)

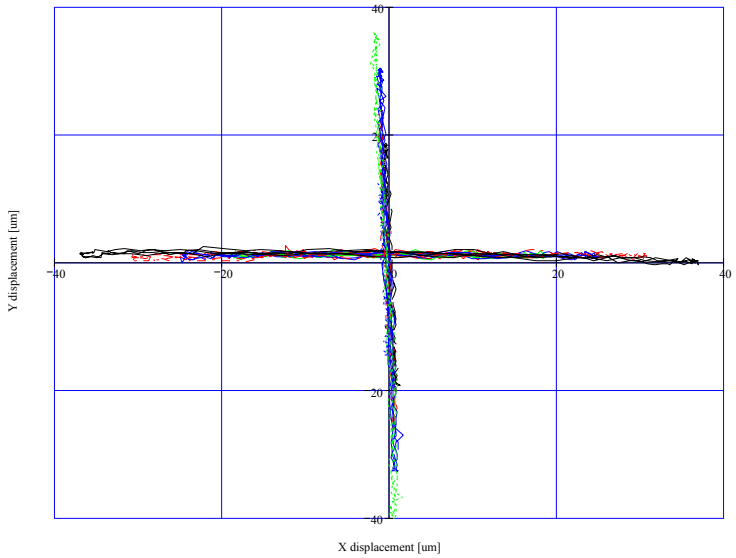

Figure D 3 Linear displacement in *X* and *Y* due to a unidirectional load in *X* and *Y* directions, respectively (40 Hz)

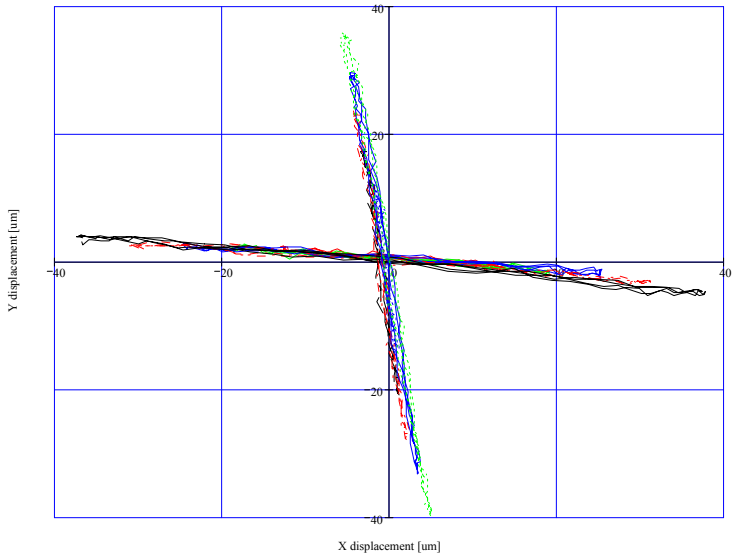

Figure D 4 Linear displacement in *X* and *Y* due to a unidirectional load in *X* and *Y* directions, respectively (50 Hz)

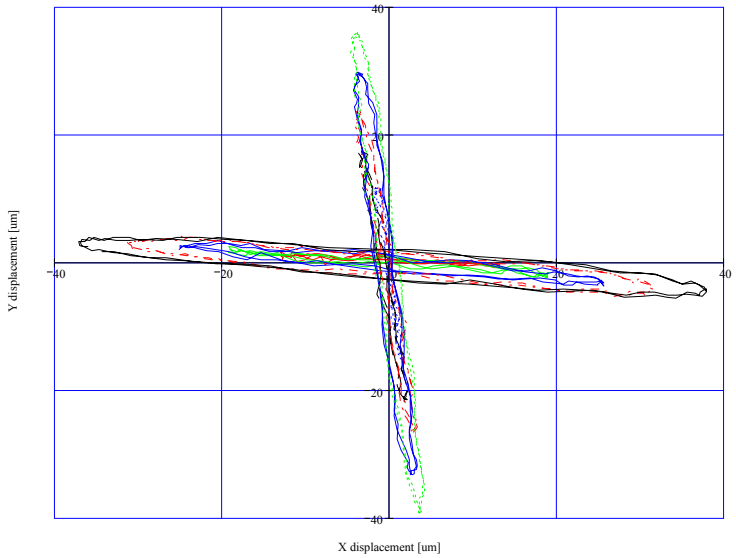

Figure D 5 Linear displacement in *X* and *Y* due to a unidirectional load in *X* and *Y* directions, respectively (60 Hz)

APPENDIX E

SQUEEZE FILM ADDED MASS COEFFICIENTS AS A FUNCTION OF DISPLACEMENT AMPLITUDE

This appendix shows the added mass coefficient identified from the unidirectional periodic excitation load tests. The coefficients are extracted from system dynamic stiffness and are presented in Table E 1.

Table E 1Added mass coefficients and correlation factors

		Coefficient [kg]	Correlation (r^2)
13 μm	D_{xx}	6.8	0.92
	D_{yy}	3.2	0.79
19 μm	D_{xx}	8.4	0.98
	D_{yy}	5.2	0.87
25 μm	D_{xx}	8.9	0.92
	D_{yy}	6.2	0.98
32 μm	D_{xx}	9.1	0.99
	D_{yy}	7.7	0.96
38 μm	D_{xx}	9.4	0.98
	D_{yy}	8.1	0.96

Figure E1 depicts the identified added mass coefficients versus displacement amplitude. For motion amplitudes less than 32 μm, the correlation factor for the analytical fit is not good ($r^2 < 0.92$), making the parameters not reliable. This poor correlation is related to variations of the system stiffness due to the presence of dry friction. Figure E 2 shows the real component of the transfer function (*F/X*). The dynamic stiffness (*Re (F/X)*) is somewhat irregular for smaller amplitude of motions, becoming smoother as the amplitude of motions increases. Further testing is needed to asses this phenomenon and improve the identification of added mass coefficients at low amplitudes of motion.

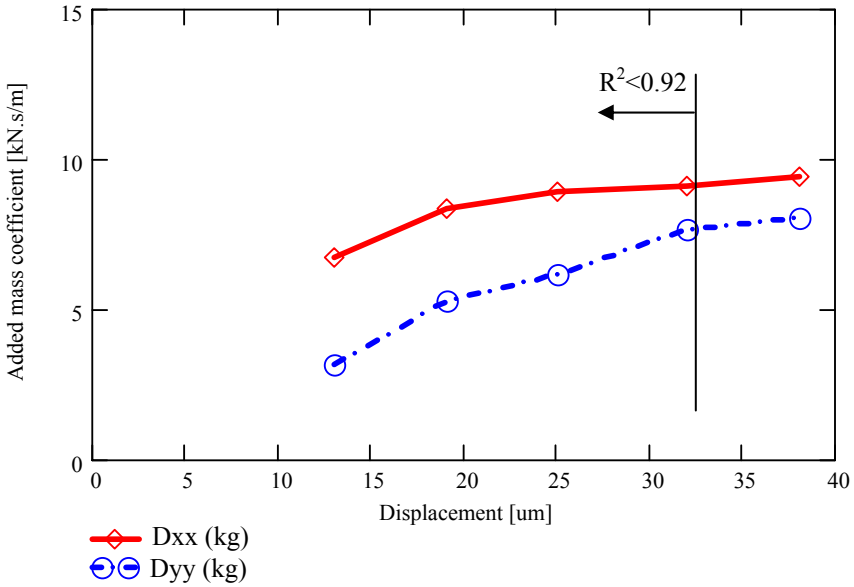

Figure E1 Squeeze film added mass coefficient versus displacement amplitude. (Identification range 20-60Hz)

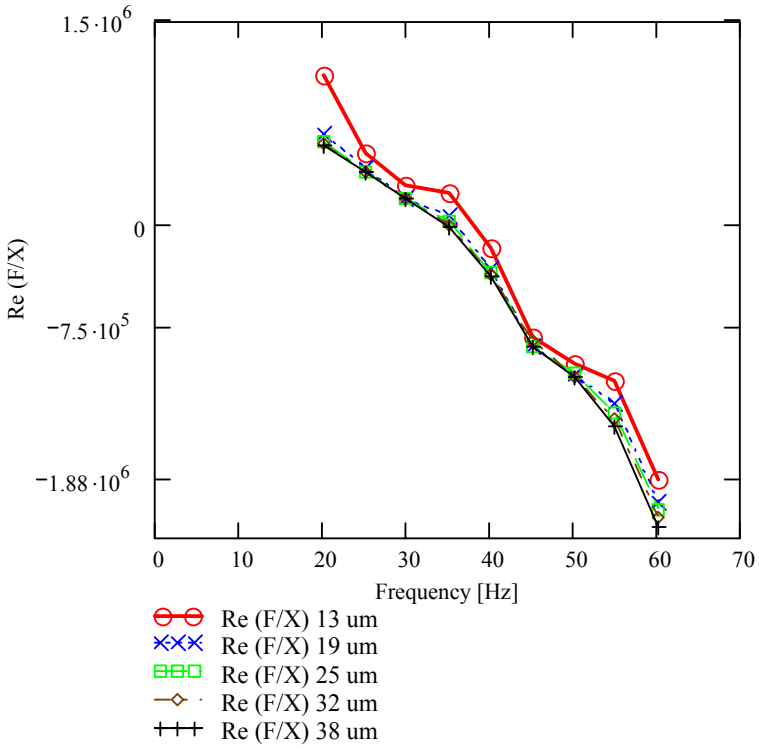

Figure E2 Real component of the transfer function (*F/X*) versus excitation frequency for increasing amplitudes of motion. (Unidirectional tests)

APPENDIX F

IDENTIFIED SQUEEZE FILM DAMPING COEFFICIENTS AS FUNCTION OF DISPLACEMENT AMPLITUDE AND FREQUENCY (UNIDIRECTIONAL TESTS)

This appendix presents the viscous damping coefficients for five excitation frequencies and displacement amplitudes. Figure F1 shows the squeeze film damper coefficients are mostly constant throughout the displacement amplitudes tested (13 μm - 38 μm).

Figure F2 presents the squeeze film damper coefficient versus excitation frequency for five different amplitudes of motion. Notice that the damper coefficient drops suddenly at around 40 Hz, which coincides with the natural frequency of the main frame of the test rig. This behavior is presumably related to a variation of the dry friction force due to a motion of the main frame holding the test element. However, the damper coefficients are fairly constant throughout the test frequency range, in particular for the largest amplitude of motion (38 μm).

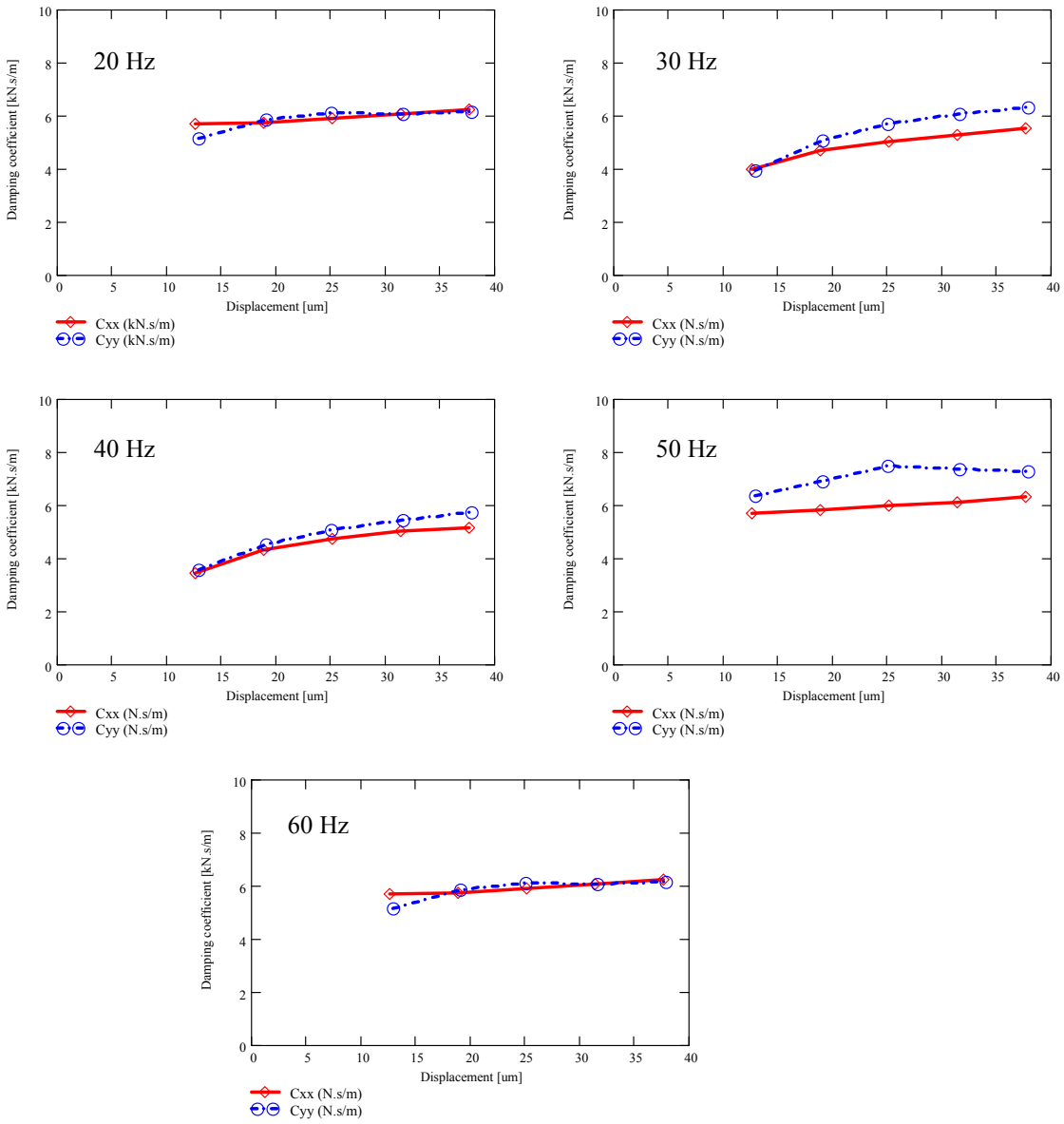

Figure F1 Squeeze film damping coefficients vs. displacement amplitude for five excitation frequencies (20 Hz, 30 Hz, 40 Hz, 50 Hz, 60 Hz).(Lubricated SFD, unidirectional load)

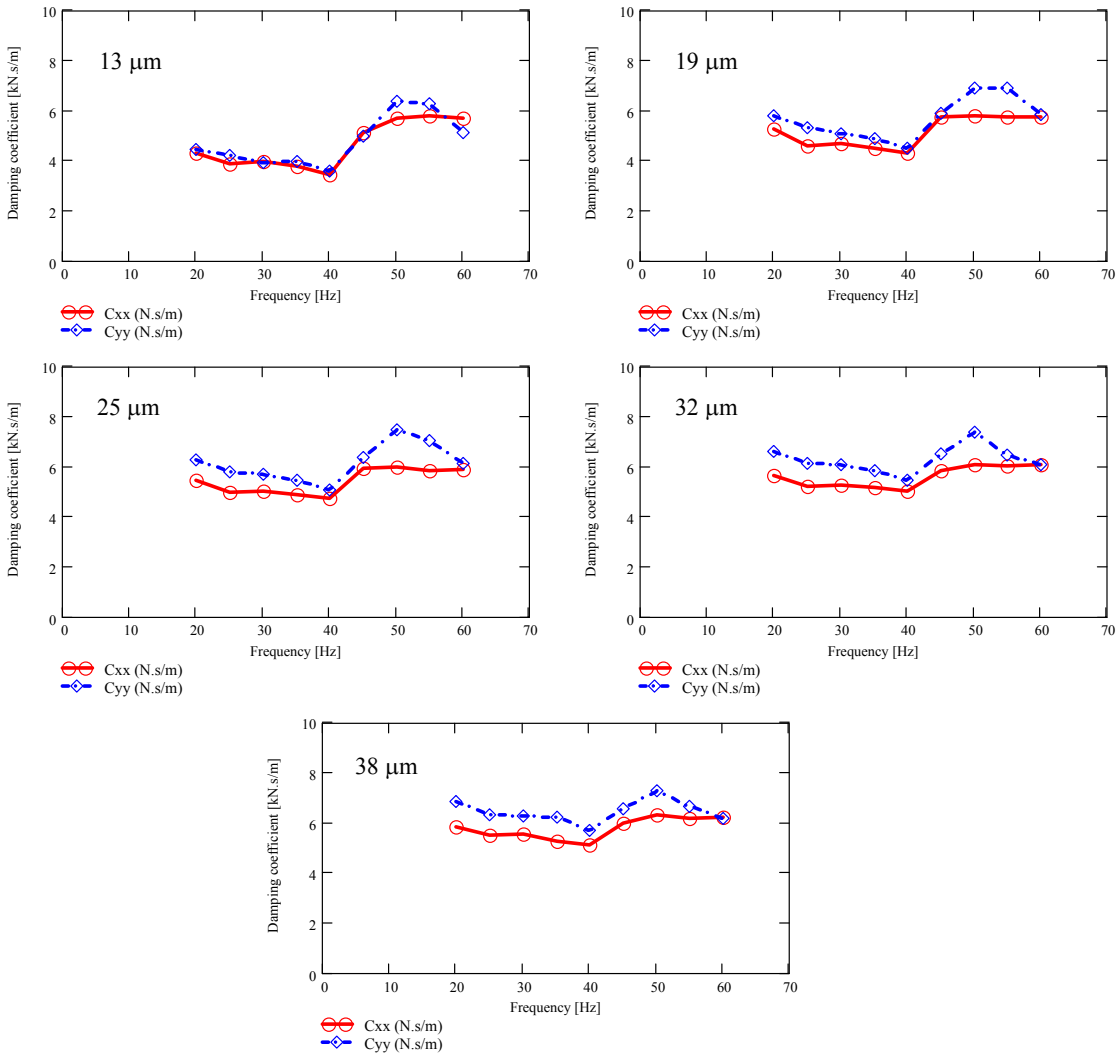

Figure F2 Squeeze film damping coefficient vs. excitation frequency for 5 constant displacement amplitudes (13 µm, 19 µm, 25 µm, 32 µm, 38 µm). (Lubricated SFD, unidirectional load)

APPENDIX G

IDENTIFICATION OF DRY FRICTION FORCE

This appendix presents the identification of the end seal friction force for the centered circular orbit (CCO) tests. A reassessment of the dry friction force for the CCO tests was mandatory due to a series of modifications applied to the tests rig in order to improve the alignment of the test damper element. Table G1 presents the dry friction force and equivalent viscous damping value from the new sets of tests. The dry friction force value equals 31 N and is slightly higher (~16%) than the previous value (26 N).

Table G1 Identified (averaged) dry friction force and equivalent viscous coefficients from single frequency excitation tests (20-120 Hz)

Test	Load(N)	Friction Force F_μ (N)	Residual Damping C_{rv}(N.s/m)	r^2
1	40	31	370	0.98
	34			0.98

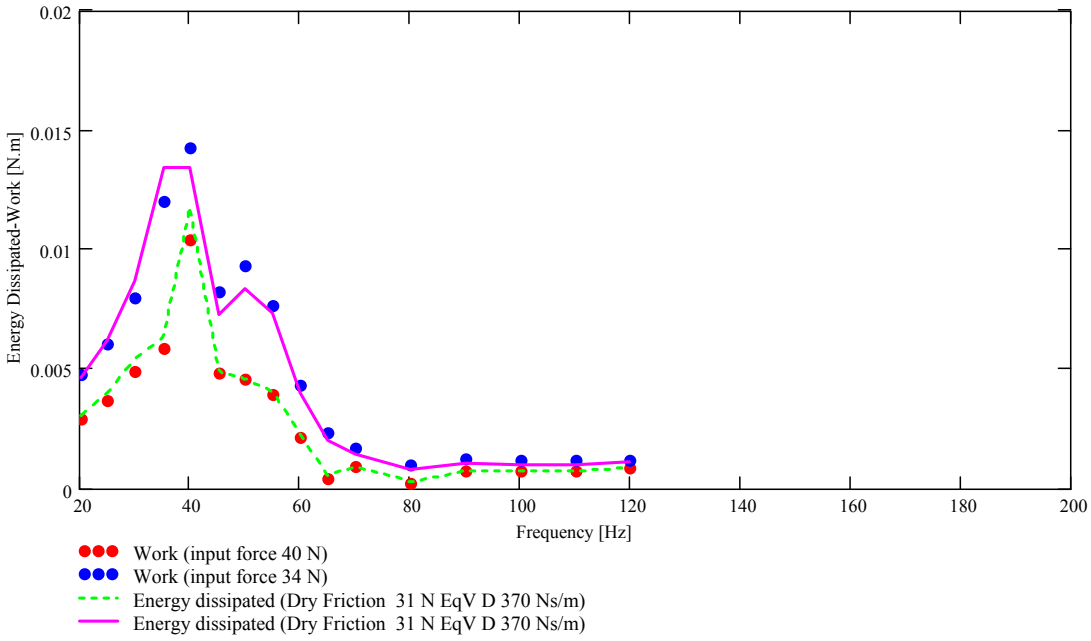

Figure G1 Work exerted by input force (= dissipated energy) estimated from combined damping model. (Dry SFD, end seal in place,CCO)

APPENDIX H

DISPLACEMENT ORBITS FOR SELECTED FREQUENCIES. (CIRCULAR CENTERED ORBITS)

This appendix presents the recorded orbits for the circular centered tests. The orbits are mostly circular from 20 Hz to 55 Hz. The orbits at 60 Hz are not circular due to an uneven distribution of the normal force at the sealing interface, mainly associated to misalignment of the test element. This same phenomenon was evidenced without oil in the SFD land.

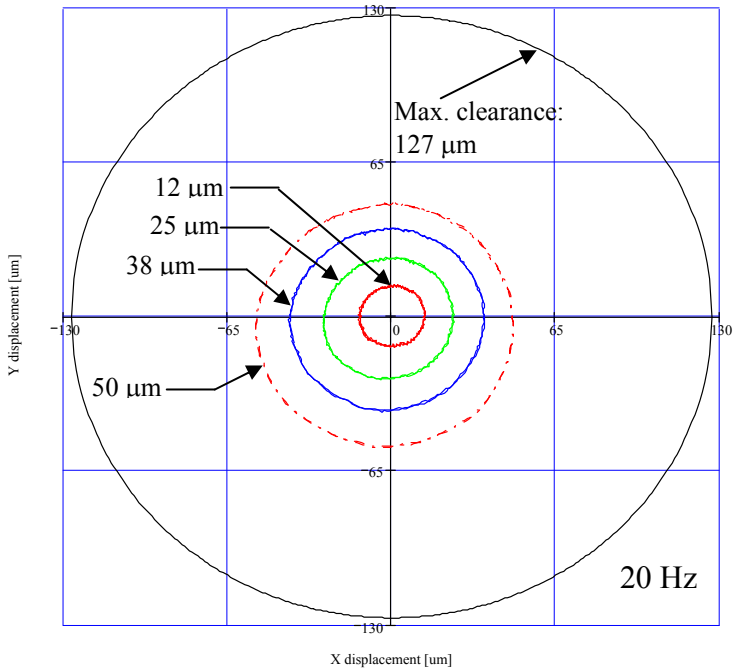

Figure H 1 Displacement orbits for four amplitude levels and maximum clearance orbit. (20 Hz, lubricated SFD, CCO)

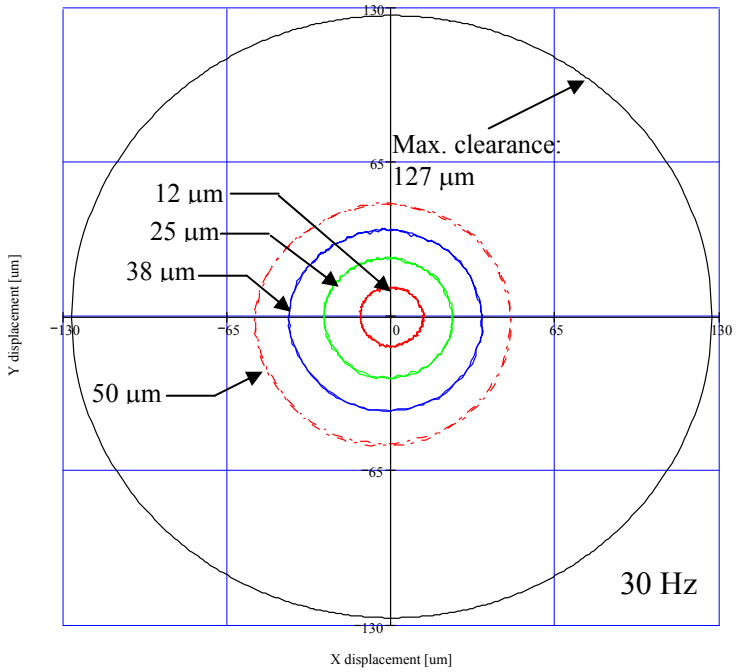

Figure H 2 Displacement orbits for four amplitude levels and maximum clearance orbit. (30 Hz, lubricated SFD, CCO)

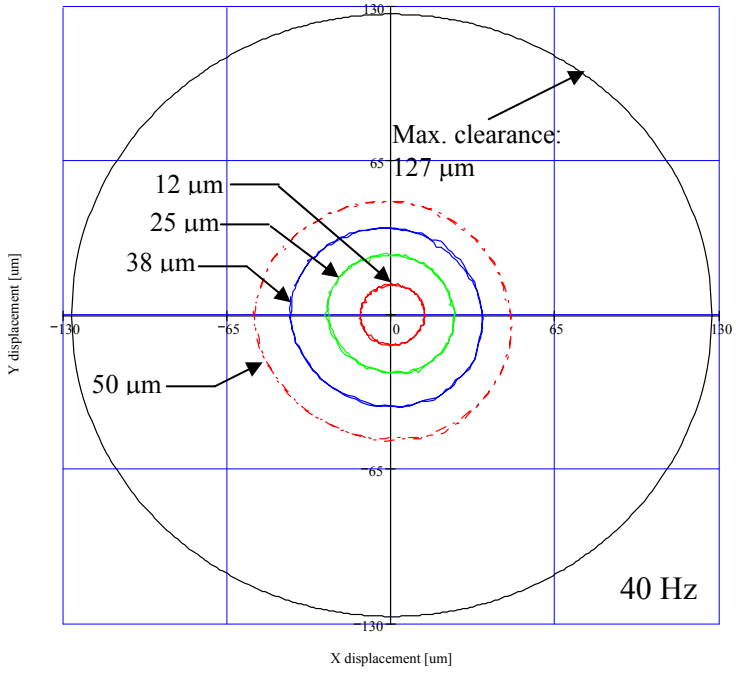

Figure H 3 Displacement orbits for four amplitude levels and maximum clearance orbit. (40 Hz, lubricated SFD, CCO)

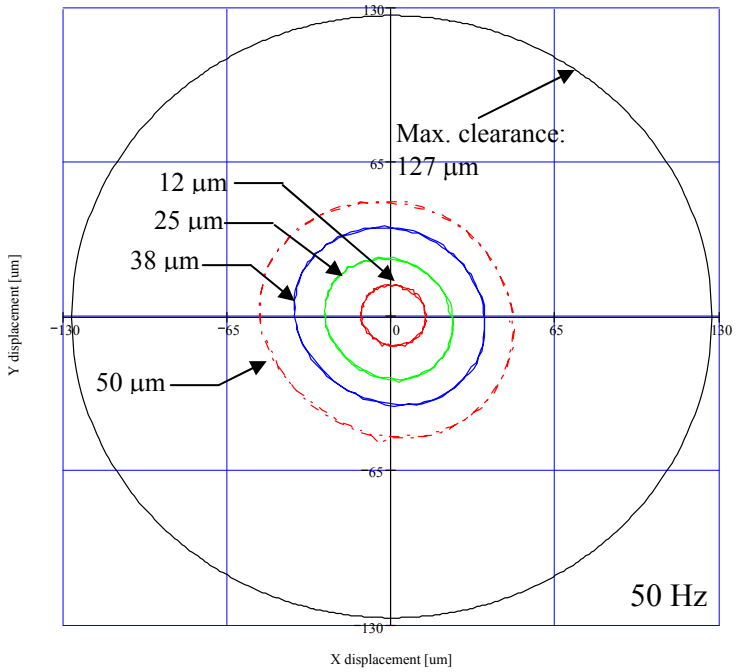

Figure H 4 Displacement orbits for four amplitude levels and maximum clearance orbit. (50 Hz, lubricated SFD, CCO)

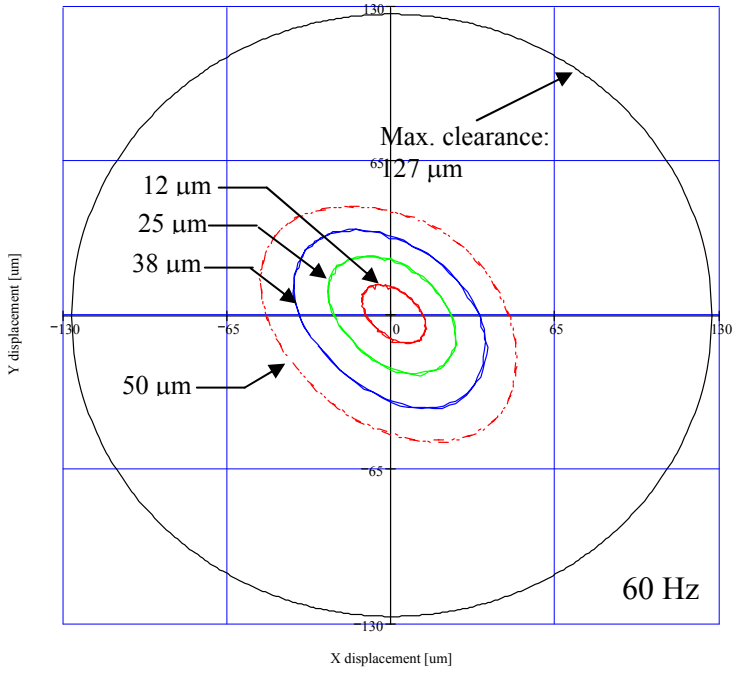

Figure H 5 Displacement orbits for four amplitude levels and maximum clearance orbit. (60 Hz, lubricated SFD, CCO)

APPENDIX I

DYNAMIC IMPEDANCES FOR CIRCULAR CENTERED ORBIT TEST

This appendix presents the direct (X/F_x, Y/F_y) and cross (X/F_y, Y/F_x) dynamic transfer functions versus excitation frequency. Figures I1 through I4 depict the magnitude and phase angle of the dynamic impedances for 12 μm, 25 μm, 38 μm, 50 μm displacement amplitudes, respectively. The direct dynamic impedances in *X* and *Y* show similar magnitude and phase. On the other hand, the cross-coupled dynamic impedances in *X* and *Y* directions are similar magnitudes but 180^0 out of phase (opposite sign).

Figures I5 through I8 present the direct and cross dynamic impedances (H_D, H_C). The amplitude of the cross-coupled impedance is considerably smaller than the direct impedance for all the test displacement amplitudes.

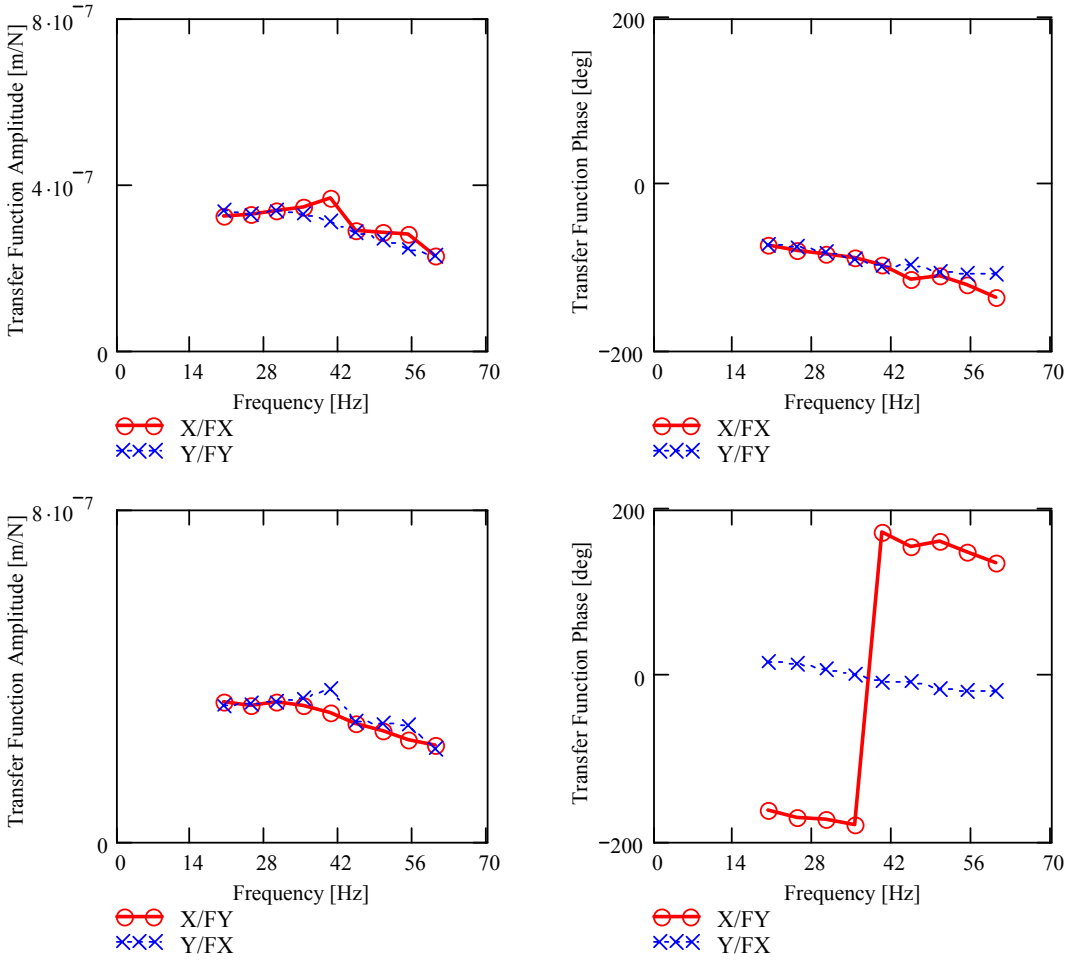

Figure I 1 Direct (*X/FX*, *Y/FY*) and cross (*Y/FX*, *X/FY*) transfer function magnitudes and phase versus excitation frequency. (12 mm, Circular Centered Orbit)

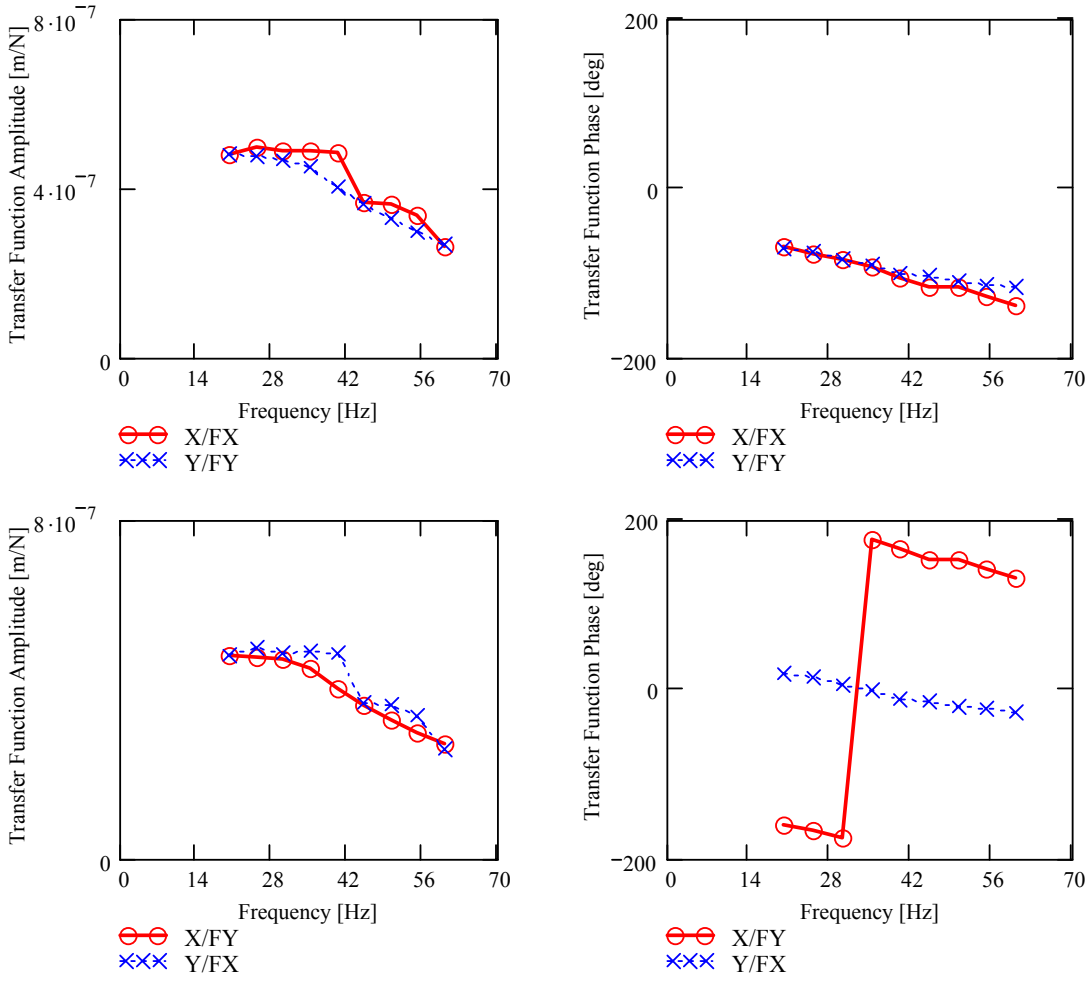

Figure I 2 Direct (*X/FX*, *Y/FY*) and cross (*Y/FX*, *X/FY*) transfer function magnitudes and phase versus excitation frequency. (25 μm, Circular Centered Orbit)

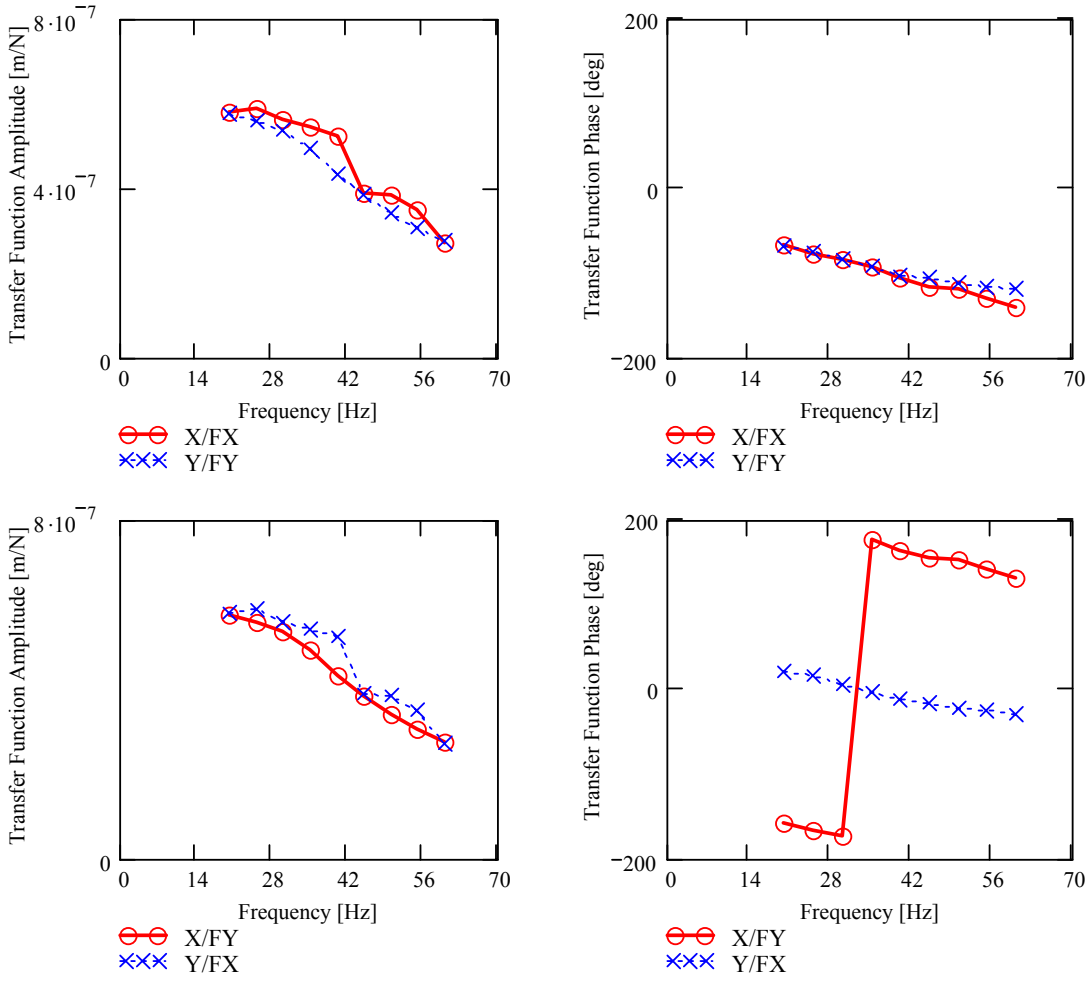

Figure I 3 Direct (*X/FX*, *Y/FY*) and cross (*Y/FX*, *X/FY*) transfer function magnitudes and phase versus excitation frequency. (38 μm, Circular Centered Orbit)

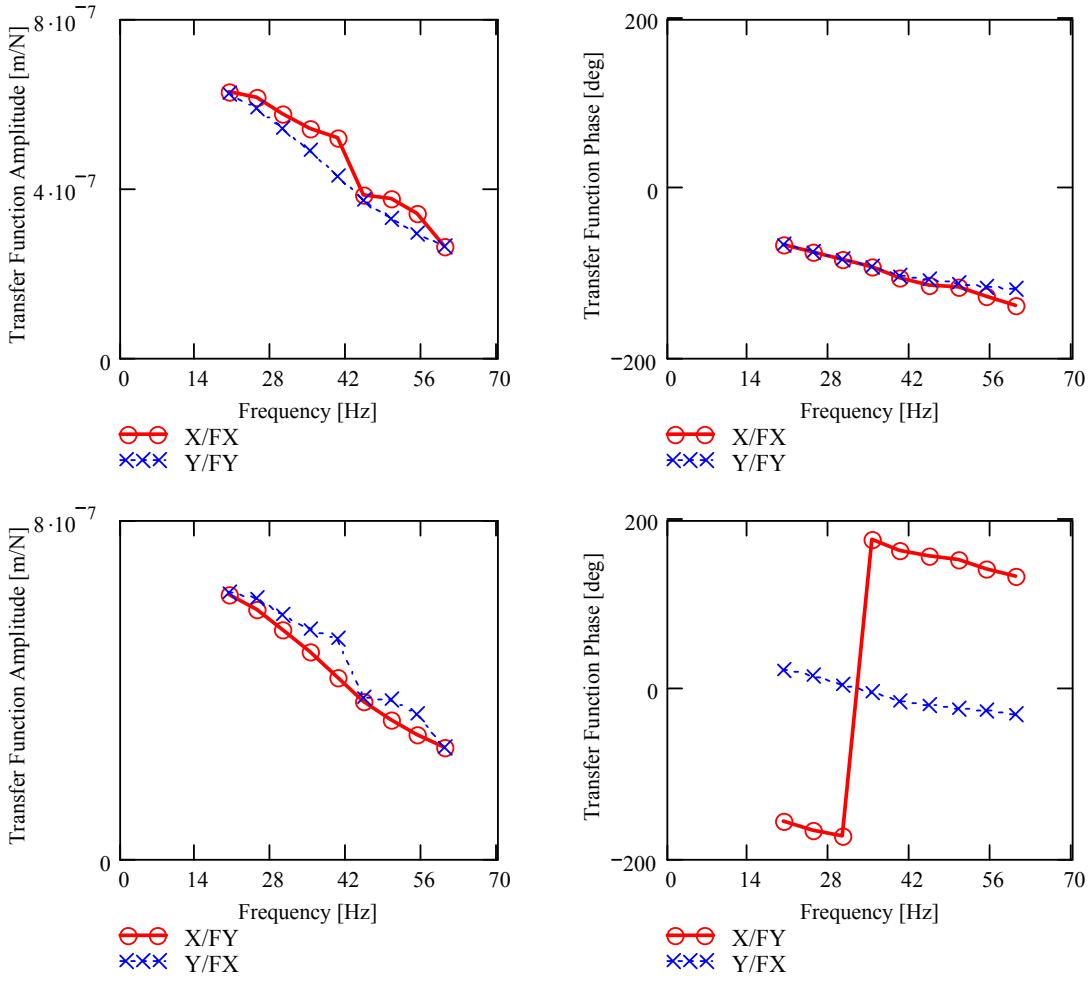

Figure I 4 Direct (*X/FX*, *Y/FY*) and cross (*Y/FX*, *X/FY*) transfer function magnitudes and phase versus excitation frequency. (50 μm, Circular Centered Orbit)

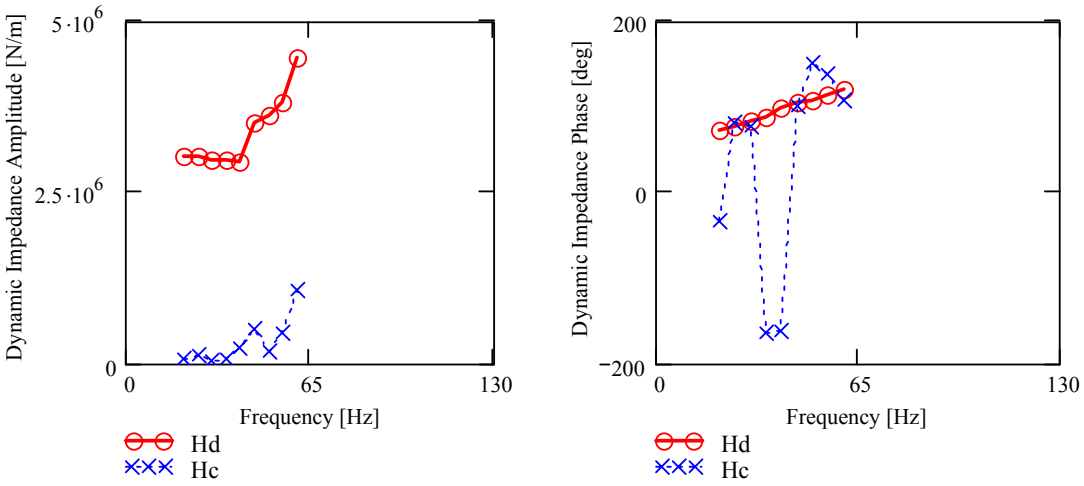

Figure I 5 Direct (*X/FX*, *Y/FY*) and cross (*Y/FX*, *X/FY*) dynamic impedance magnitudes and phase versus excitation frequency. (12 μm, Circular Centered Orbit)

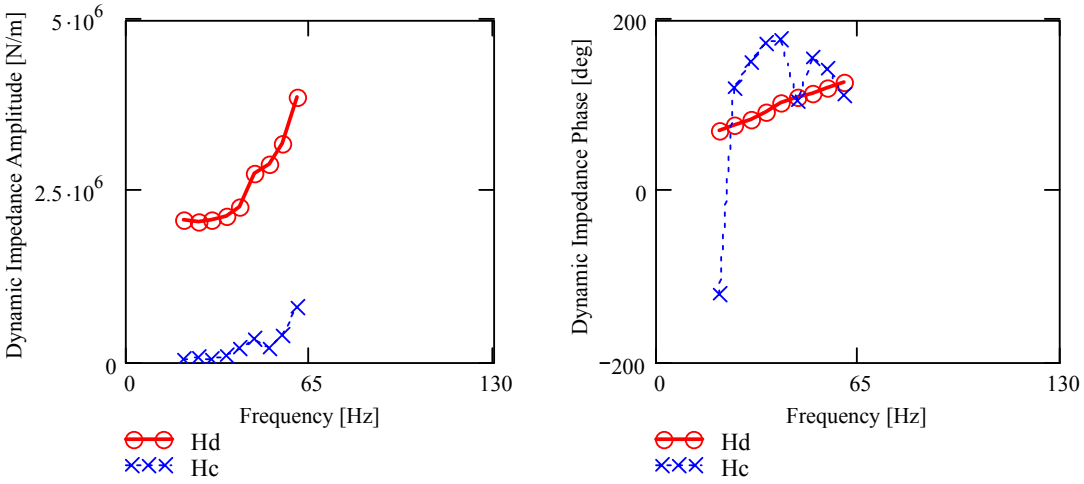

Figure I 6 Direct (*X/FX*, *Y/FY*) and cross (*Y/FX*, *X/FY*) transfer function magnitudes and phase versus excitation frequency. (25 μm, Circular Centered Orbit)

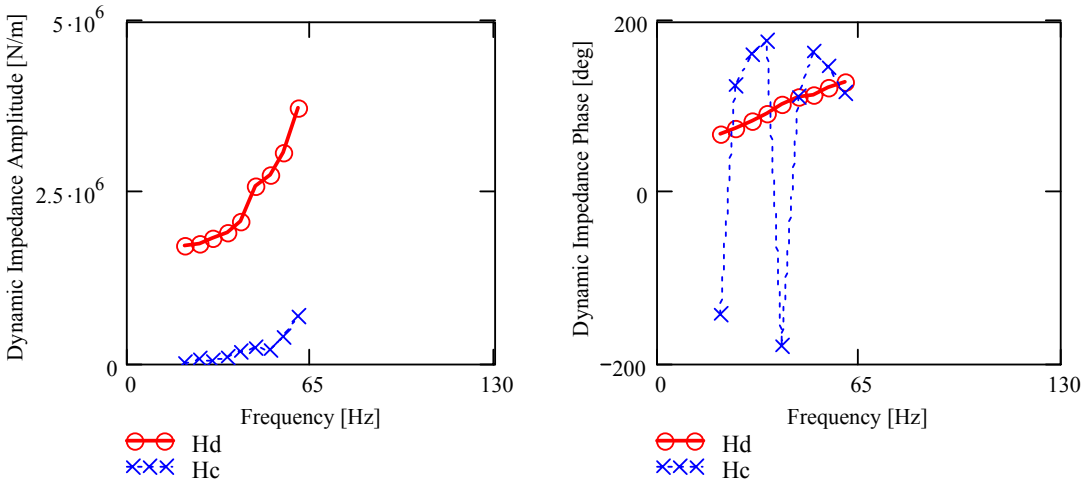

Figure I 7 Direct (*X/FX*, *Y/FY*) and cross (*Y/FX*, *X/FY*) transfer function magnitudes and phase versus excitation frequency. (38 μm, Circular Centered Orbit)

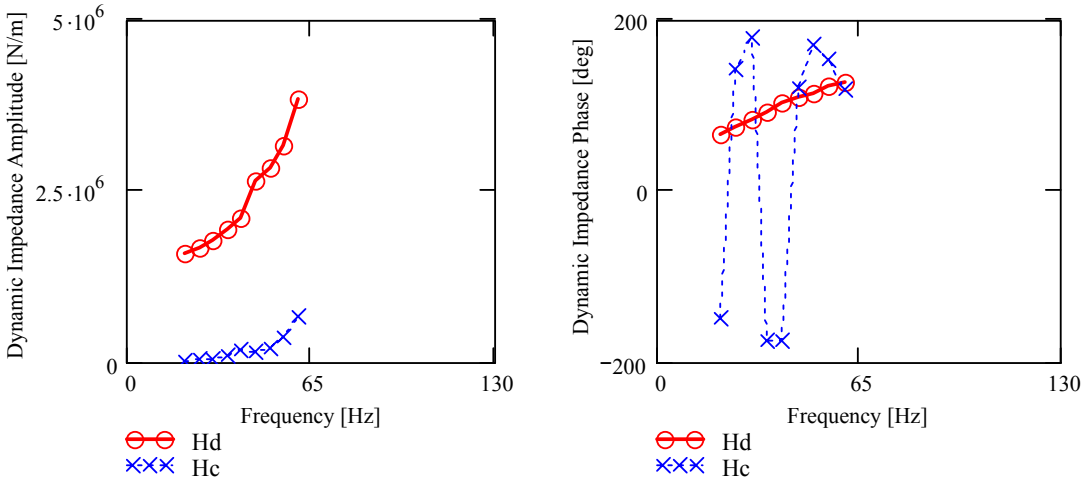

Figure I 8 Direct (*X/FX*, *Y/FY*) and cross (*Y/FX*, *X/FY*) transfer function magnitudes and phase versus excitation frequency. (50 μm, Circular Centered Orbit)

VITA

Name: Adolfo Delgado-Marquez

Address: Texas A&M Turbomachinery Laboratory, College Station, TX 77843-3123

Email Address: adelgam@tamu.edu

Education: B.S., Mechanical Engineering, Universidad Simón Bolívar at Caracas (Venezuela), 2002.

Interests: Turbomachinery- rotordynamics and lubrication. Parameter identification of mechanical systems.

Publications: Delgado, A., San Andrés, "Identification of Structural Stiffness and Damping Coefficients of a Shoed Brush Seal," ASME IDETC/CIE Conference, Long Beach, CA. September, 2005.

Delgado, A., San Andrés, L., Justak, J., "Analysis of Performance and Rotordynamic Force Coefficients of Brush Seals with Reverse Rotation Ability," VII ASME Turbo Expo, Vienna, Austria. June, 2004.

Delgado, A., San Andrés, L., Justak, J., "Identification of Stiffness and Damping Coefficient in a Shoed Brush Seal," VIII Congreso Latinoamericano de Turbomaquinas, Veracruz, Mexico. October, 2003